

AD-757 275

An Atmospheric Noise Model with Application to Low Frequency Navigation Systems

**Massachusetts Institute of
Technology**

**prepared for
Coast Guard**

JUNE 1972

Distributed By:

NTIS

**National Technical Information Service
U. S. DEPARTMENT OF COMMERCE**

AD 757275

AN ATMOSPHERIC NOISE MODEL WITH APPLICATION TO
LOW FREQUENCY NAVIGATION SYSTEMS

by

Donald Alexander Feldman

B. S., U. S. Coast Guard Academy
(1961)

M. S. E. E., E. E., Massachusetts Institute of Technology
(1966)

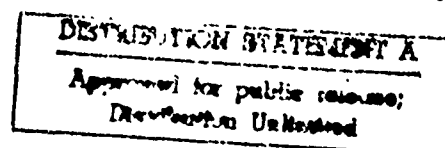
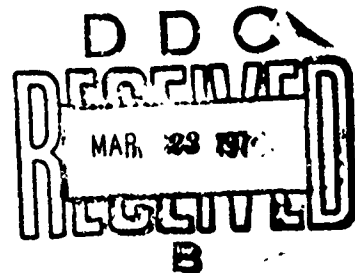
SUBMITTED IN PARTIAL FULFILLMENT OF THE
REQUIREMENTS FOR THE DEGREE OF
DOCTOR OF SCIENCE

at the

MASSACHUSETTS INSTITUTE OF TECHNOLOGY

June, 1972

Reproduced by
NATIONAL TECHNICAL
INFORMATION SERVICE
U S Department of Commerce
Springfield VA 22151



1. Report No. DOT-CG-13446-A	2. Government Accession No.	3. Recipient's Catalog No.	
4. Title and Subtitle AN ATMOSPHERIC NOISE MODEL WITH APPLICATION TO LOW FREQUENCY NAVIGATION SYSTEMS		5. Report Date 30 JUNE 1972	
		6. Performing Organization Code	
		8. Performing Organization Report No.	
7. Author(s) DONALD ALEXANDER FELDMAN		10. Work Unit No. (TRAIS)	
9. Performing Organization Name and Address DEPARTMENT OF TRANSPORTATION U. S. COAST GUARD 400 7th STREET, S W. WASHINGTON, D.C. 20590		11. Contract or Grant No. LOT-CG-13446-A	
		13. Type of Report and Period Covered DOCTORAL DISSERTATION	
		14. Sponsoring Agency Code	
12. Sponsoring Agency Name and Address Same as No. 9.			
15. Supplementary Notes Authors note "Submitted in partial fulfillment of the requirements for the Degree of Doctor of Science at the Massachusetts Institute of Technology."			
16. Abstract A prerequisite of the design of low frequency radio receivers is a model for low frequency atmospheric radio noise that encompasses the non-Gaussian nature of the actual noise process and is sufficiently tractable to enable performance analysis and optimization of receiver designs. This work describes a new model for atmospheric noise waveforms observed at the output of the antenna band-limiting filter. This model, which is based on statistical analysis of sample records of these waveforms, is used to analyze the performance of typical radio navigation receivers and to determine near optimum receiver performance. The analysis is verified by simulating the receiver structure and testing the receiver with the actual noise sample records.			
17. Key Words Atmospheric noise models, Low frequency noise models, low frequency navigation radio receivers		18. Distribution Statement Document is available to the public through the National Technical Information Service, Springfield, Virginia, 22151	
19. Security Classif. (of this report) Unclassified	20. Security Classif. (of this page) Unclassified	21. No. of Pages 205	22. Price

AN ATMOSPHERIC NOISE MODEL WITH APPLICATION TO
LOW FREQUENCY NAVIGATION SYSTEMS

BY

Donald Alexander Feldman

Submitted to the Department of Electrical Engineering
on 30 June 1972 in partial fulfillment of the require-
ments for the Degree of Doctor of Science

ABSTRACT

A prerequisite for the design of low frequency radio receivers is a model for low frequency atmospheric radio noise that encompasses the non-Gaussian nature of the actual noise process and is sufficiently tractable to enable performance analysis and optimization of receiver designs. This work describes a new model for atmospheric noise waveforms observed at the output of the antenna bandlimiting filter. This model, which is based on statistical analysis of sample records of these waveforms, is used to analyze the performance of typical radio navigation receivers and to determine near optimum receiver performance. The analysis is verified by simulating the receiver structure and testing the receiver with the actual noise sample records.

The proposed model for bandlimited atmospheric noise utilizes a background Gaussian process, of constant power level, to which is added discrete bursts of Gaussian noise whose power level, for each burst, is a random variable. The burst occurrences and the power level are common to waveforms observed in disjoint frequency channels and provides a model for the statistical dependence between such waveforms. The model is shown to match first order characteristics of a bandlimited noise waveform and a noise envelope, recorded in disjoint channels, over a range of noise conditions from nearly Gaussian to the severest noise caused by frontal thunderstorm activity. The length of each noise burst, and occurrence rate intensity, are both stochastic in the model. A non-homogeneous Markov process provides a description of these burst characteristics and is shown to result in an envelope autocorrelation that matches observed correlations over periods of 1 millisecond to 1 second.

THESIS SUPERVISOR: Amar G. Bose

TITLE: Professor of Electrical Engineering

The atmospheric noise model is used to analyze the performance of three basic types of phase-locked-loops used in navigation receivers. The first of these is a linear time-invariant loop optimized for the noise power level. The second adds a zero memory nonlinearity in the path of the loop error signal and is optimized to the first-order noise probability density. The third is a near optimum structure that uses the joint channel noise model and the second channel noise envelope to convert the atmospheric noise process to an approximate time-varying gaussian process. This can be optimally filtered by a time-varying Kalman-Bucy estimator. It is shown, using the recorded noise sequences, that the simple nonlinear loop provides performance improvements of up to 16 dB compared to the time-invariant linear case, and that the optimum time-varying filter provides additional improvements of up to 3-5 dB when receiver processing intervals are less than several seconds.

The work concludes with suggestions for further research, including an application of the joint channel noise model to the design of an optimum digital communication receiver that appears to be both practical and offer significant performance advantages over present designs.

DEDICATION

This work is dedicated to the people who are the U. S. Coast Guard, with whom I have been privileged to serve these past fifteen years, and who have provided all of my educational opportunities.

ACKNOWLEDGMENT

It is, of course, never possible to acknowledge all of the contributors to a work of this nature that has required extensive laboratory, shop, instrumentation and computational facilities. First must come Ellen, Kenneth, and Kaywin, without whose love and understanding it would have been infinitely more difficult. I am indebted to the thesis committee of Professors Bob Kennedy and Don Nelsen and in particular the supervisor, Professor Amar Bose, who gave unstintingly of his time, guidance and faith in the eventual outcome. Mr. Ralph Sayers, Assistant Director of the Research Laboratory of Electronics and the entire support staff provided for every requirement, be it one day delivery of a part or 1 more hour of computer time. William Lee contributed to the design and construction of the instrumentation system, and David Thiele provided the machine language program base for all of the computer efforts. Finally, the U. S. Coast Guard funded the instrumentation system under contract DOT-CG-13446-A and provided the laboratory space and facilities for the noise recordings on which the entire work rests.

TABLE OF CONTENTS

	<u>Page</u>
Chapter 1 INTRODUCTION	16
1.1 Atmospheric Noise Mechanisms	18
1.2 Experimental Noise Data	21
1.3 Proposed Noise Models	22
1.3.1 Impulse Model	22
1.3.2 Communication Models	24
1.3.3 Multiplicative Noise Model	25
Chapter 2 EXPERIMENTAL DATA	27
2.1 Noise Characteristics Measured	28
2.2 Instrumentation System	29
2.3 Classification of Observations by Weather Conditions	30
2.4 First Order Probability Density of Atmospheric Noise	32
2.4.1 Single Frequency Channel Probability Density	32
2.4.2 Joint Frequency Channel Probability Density	36
2.5 Time Structure of Atmospheric Noise	44
2.5.1 Power Spectral Density	44
2.5.2 Time Structure of $A(t)$	45
2.6 Summary	54
Chapter 3 AN ATMOSPHERIC NOISE MODEL	56
3.1 Hall's Noise Model	56
3.2 An Extension of Hall's Model	58
3.3 Noise Envelope	61
3.4 Joint Channel Model	63
3.5 First Order Model Statistics	65
3.5.1 Unconditional Moments	65
3.5.2 Conditional Moments	69

	<u>Page</u>
3.6 Comparison of Joint Channel First Order Model with Data	72
3.6.1 General Parametric Dependence	72
3.6.2 Comparison Results	74
3.6.3 Comparison with Additional Joint Channel Characteristics	83
3.7 Noise Model Time Structure	87
3.7.1 General Time Structure	89
3.7.2 Functional Form of the Model Time Structure	91
3.7.3 Time Structure Simulation Results	99
3.8 A Canonic Atmospheric Noise Generator	102
3.9 Summary	105
3.9.1 Model Results	105
3.9.2 Additional Questions	107
 Chapter 4 AN OPTIMUM DESIGN FOR NAVIGATION RECEIVERS	 111
4.1 Definition of the Problem	113
4.1.1 Navigation Problem	113
4.1.2 Signal Generator Model	114
4.1.3 Signal Processing Structure	116
4.2 Optimum Linear Time Invariant Estimator	118
4.2.1 Kalman-Bucy Equations	118
4.2.2 Sampled Data-Continuous Time Relations	122
4.2.3 Relation to Classical Design Procedures	123
4.3 Time Invariant Non-Linear Estimator	124
4.3.1 Definition of Non-Linear Estimator Class	124
4.3.2 Linearized Analysis	125
4.3.3 ZNL Improvement Factor	128
4.3.4 Improvement Factor of Four Types of ZNL's in Atmospheric Noise	131
4.3.5 Optimality of ZNL Estimator Class	139

4.4	Linear Time-Varying Estimator	141
4.4.1	Use of Joint Channel Noise Model	141
4.4.2	Performance of Time-Varying Linear Estimator	143
4.5	Test of Estimators for Scalar Signal Model	145
4.5.1	Operating Equations	145
4.5.2	Simulation Technique	147
4.5.3	Simulation Results	149
4.6	Test of Estimators for Two-State Signal Model	153
4.6.1	Operating Equations	153
4.6.2	Simulation Technique	157
4.6.3	Simulation Results	157
4.7	Summary and Remarks	162
4.7.1	Summary of Navigation Receiver Design Results	162
4.7.2	Remarks on Receiver System Design	164
4.7.2.1	Linear Receivers	166
4.7.2.2	Hard Limiting Receivers	166
4.7.2.3	Optimum Receivers	168
Chapter 5	SUMMARY AND SUGGESTIONS FOR FURTHER WORK	169
5.1	Summary	169
5.2	Suggestions for Further Work	170
5.2.1	Noise Model	170
5.2.2	Applications to Communication Receiver Design	172
	BIBLIOGRAPHY	177
Appendix A	INSTRUMENTATION SYSTEM	182
A-1	Introduction	182
A-2	Analog Signal Processing	183
A-3	Digital Timing and Control	191
A-4	Data Handling	192
A-5	Data Storage and Output	193

Page

Appendix B DATA ANALYSIS ALGORITHMS	195
B-1 Probability Density Analysis	195
B-2 Probability Density Estimation Error	197
B-3 Probability Density Surface Analysis	199
B-4 Correlation Analysis	199
Appendix C INSTRUMENTATION TESTS	201
C-1 Probability Density Tests	201
C-2 Correlation Tests	201
Biography of Donald A. Feldman	205

LIST OF FIGURES

-10-

<u>Figure Number</u>		<u>Page</u>
1-1.	Examples of Lightning Discharge Radiation	19
2-1.	Noise Probability Density at VLF and LF	33
2-2.	LF Noise pdf's Observed in 1 and 10 kHz Bandwidths	35
2-3.	Correlation of RF Noise Magnitude with Various $A(t)$ Estimates	37
2-4.	Sample Waveforms from RF Channel and Envelope Channel	37
2-5.	Joint Probability Surface for Quiet and Frontal Conditions	40
2-6.	Joint Probability Surface for Tropical Conditions	41
2-7.	Standard Deviation of RF Channel Noise Conditioned by Pilot Channel Envelope	43
2-8.	Autocorrelation Envelope of Bandlimited Atmospheric Noise	46
2-9.	Sample Record of $A(t_i)$ Estimates	48
2-10.	Short-Time and Long-Time Autocorrelation of $A(t_i)$	50
2-11.	Long-Time Correlation Decay Detail	52
2-12.	Long-Time Correlation for Quiet and Transition Conditions	53
3-1.	Comparison of Model to Quiet Noise Observations	75
3-2.	Comparison of Model to Quiet-Night Noise Observa- tions	76
3-3.	Comparison of Model to Tropical Noise Observations	77
3-4.	Comparison of Model to Frontal Noise Observations	78
3-5.	Comparison of Model to VLF Noise Observations	82

Figure
Number

-ii-
Page

3-6.	Comparison of Model Conditional Density to Tropical Observations	85
3-7.	Comparisons of Mean-RMS Ratio for Conditional RF Noise Density	87
3-8.	Equivalent $A(t_i)$ Generator	91
3-9.	Simulated $A(t_i)$ Sample Record	100
3-10.	Autocorrelation of Simulated $A(t_i)$ Sample Record	101
3-11.	Atmospheric Noise Generator for Computer Simulation	103
4-1.	Block Diagram of Phase-Locked Loop Simulation	119
4-2.	Various ZNL Transfer Functions	134
4-3.	ZNL Improvement Factor for Frontal and Tropical Noise Conditions	136
4-4.	ZNL Improvement Factor for Quiet and Quiet-Night Noise Conditions	137
4-5.	ZNL Improvement Factor for Gaussian Noise and Equivalent Linear Gain	138
4-6.	Standard Deviation of Estimation Error for Scalar Signal Model	150
4-7.	Time Evolution of Estimation Error for Scalar Signal Model	152
4-8.	Standard Deviation of Estimation Error for Two-State Signal Model	158
4-9.	Time Evolution of Estimation Error for Two-State Signal Model	161
5-1.	Optimum Digital Receiver for Atmospheric Noise	173

Figure
Number

-12-

Page

A-1.	Block Diagram of Instrumentation System	184
A-2.	Received Noise and Interference Spectrum	186
A-3.	Frequency Response of Observation Filters	188
B-1.	Probability Density Estimation Error	198
C-1.	Estimate of Gaussian Cumulative Distribution	203
C-2.	Correlation Test Result	204

LIST OF TABLES

Table 3-1.	Canonic Noise Generator Parameters	104
------------	------------------------------------	-----

LIST OF SYMBOLS

$A(t)$	Conceptual lowpass random process modulating Gaussian process to form atmospheric noise waveform.
$A(t_i)$	Estimates of conceptual $A(t)$ formed by integrating rf noise magnitude for 1 or 10 msec.
$a(t)$	Model random process representing $A(t)$.
$b_i(t)$	Lowpass random processes used to form $a(t)$.
E_{f2}	Symbolic representation of recorded (data) noise envelope sequence in frequency channel f_2 .
$E(\cdot)$	Expectation operator, equivalent to $\overline{(\cdot)}$.
$E(\cdot)_x$	Conditional expectation operator. average taken with respect to x .
\underline{H}	Observation matrix, linear mapping from signal process to observed process.
I. F.	Improvement Factor, output signal-to-noise ratio divided by input signal-to-noise ratio.
k	Sequential index variable of sampled data systems.
K-B	Kalman-Bucy
LF	Low Frequency, 30 to 300 kHz
MMSE	Minimum Mean Square Error performance criterion.
msec	millisecond
$N(A, B)$	Gaussian or normal distribution of mean A and variance B .
$n(k)$	Noise sequence at output of non-linearity used in signal estimation problem.
$n_1(t)$	Background Gaussian noise component of atmospheric noise model with variance σ_{nG}^2 .

$n_2(t)$	Gaussian component modulated by $a(t)$ in noise model, variance σ_{nH}^2 .
$P(A)$	Probability of discrete event A .
$P(Y_0)$	Cumulative probability of the random variable y .
PLL	Phase-Locked-Loop.
pd	Probability density.
pdf	Probability density function.
$p_x(t)$	Time varying probability the two-state process $x(t)$ is in state one.
p_x^f, p_x^s	Two probabilities, $p(x_t = 1)$, corresponding to $w(t) = 1, 0$.
$p_y(\eta)$	Probability density of the random variable y .
\underline{Q}	Covariance of random process driving signal generator model.
$\underline{R}(k+1)$	Time varying covariance matrix of observation noise (atmospheric noise).
RF_{f1}	Representation of recorded (data) bandlimited noise sequence from frequency channel f_1 .
rf	Radio frequency.
RNG	Computer generated random number generator.
$r(\cdot)$	Received waveform or sample sequence, additive combination of signal and atmospheric noise process.
rv	Random variable.
$\underline{s}(\cdot)$	Signal or message process
$\hat{\underline{s}}(\cdot)$	Instantaneous estimate of signal process.
$\tilde{\underline{s}}(\cdot)$	Instantaneous error, $\underline{s}(\cdot) - \hat{\underline{s}}(\cdot)$.
SNR	Signal-to-noise power ratio.

ΔT	sampling interval.
$U(A, B)$	Uniformly distributed random variable on the interval (A, B) .
$v_1(t)$	Background Rayleigh envelope process of atmospheric noise model, parameter σ_{vG}^2 .
$v_2(t)$	Rayleigh component modulated by $a(t)$ in noise model, parameter σ_{vH}^2 .
VLF	Very Low Frequency, 3 to 30 kHz.
$w(t)$	Two-state process modulating occurrence-rate of $x(t)$.
$x(t)$	Two-state process that adds non-Gaussian $a(t) n_2(t)$ to $n_1(t)$ in noise model when $x(t)$ equals one.
$y(t)$	Model random process representing bandlimited atmospheric noise waveform.
$z(\cdot)$	Error process at PLL comparison node, $z(\cdot) = \tilde{z}(\cdot) + y(\cdot)$.
ZNL	Zero-memory non-linear device, output is a function of instantaneous value of the input only.
$\Sigma(\cdot)$	Covariance matrix of estimate error, $E[\tilde{z}(\cdot) \tilde{z}(\cdot)^T]$.
$\Phi(t, t_0)$	State transition matrix.
λ	Transition rate of two-state Markov process $x(t)$.
μ	Transition rate of two-state Markov process $w(t)$.
μsec	Microsecond
σ_{nG}^2	Variance of background process $n_1(t)$.
σ_{vG}^2	Parameter of Rayleigh background envelope process $v_1(t)$.
σ_{nH}^2	Variance of Hall component process $n_2(t)$.
σ_{vH}^2	Parameter of Hall component envelope process $v_2(t)$.

INTRODUCTION

The Very-Low Frequency (VLF, 3-30 kHz) and Low-Frequency (LF, 30-300 kHz) electromagnetic spectrum is extensively used for digital radio communications and radio navigation. When the performance of these radio systems is limited by noise, such noise is generally atmospheric radio noise, additively combined with the signal at the receiving antenna. Thermal noise in the antenna-receiver system is generally of a lower level than this radio noise. The principal source of the dominant atmospheric noise is radiation from lightning discharges, which propagates considerable distances at these frequencies. When atmospheric noise waveforms are observed at the output of the receiver band-limiting filters used at these frequencies, it is described with words such as "impulsive," "peaky," "crashy," etc., recognizing the fact that individual lightning discharge events are discernible and tend to dominate the waveform at any given time instant. A result of this individual dominance is that statistical descriptions of the noise waveform are, in general, distinctly non-gaussian since the individual dominance condition clearly violates the basic assumption of the central limit theorem. The design of receiver structures for processing signals, corrupted by non-gaussian atmospheric noise, is a difficult procedure and the results depend critically upon the statistical characteristics ascribed to the noise. Improved characterization/design procedures are useful goals for VLF/LF systems because of the large costs associated with obtaining equivalent receiver performance improvements by increasing radiated signal power. For example, the costs of erecting antenna

structures vary as the fourth power of the height above 800'-1000'.

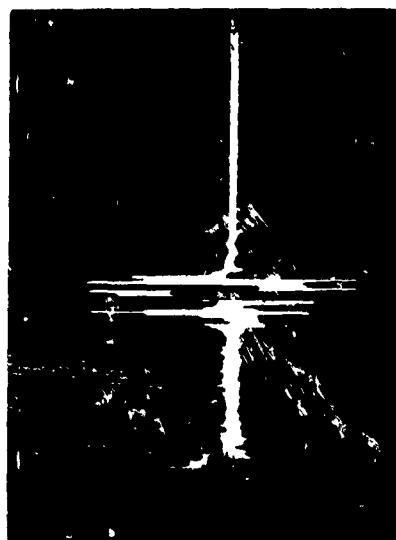
The research reported here has addressed the problem of improving the statistical characterization of low-frequency atmospheric noise for the purpose of improving the design of VLF/LF radio systems. The succeeding work is divided into four parts. Chapter 1, Introduction, provides a qualitative description of the physical noise process to motivate our conceptual approach to the problem. This approach is placed in perspective to the results reported by other workers during the past twenty years. Chapter 2, Experimental Data, is a tabulation of the various measurements we made of atmospheric noise waveforms using a digital data collection system. Most of this data represents new contributions to the literature of this field. Chapter 3, An Atmospheric Noise Model, presents a mathematical model for bandlimited atmospheric noise waveforms which describes first-order statistics, time structure, and the statistical dependence of waveforms observed in different frequency channels. Chapter 4, An Optimum Design for Navigation Receivers, applies classical servo-mechanism theory to the design of a nonlinear Phase-Locked Loop (PLL), and exploits the co-frequency-channel dependence of the noise to design a near-optimum Kalman-Bucy, time-varying PLL. Performance predictions of the designs, based on the noise model, are verified with the use of atmospheric noise sample records. Chapter 5 concludes with suggestions for further work, in particular, with other applications of the noise model to digital communication receiver design.

1.1 Atmospheric Noise Mechanism

Electromagnetic radiation from lightning discharges, the principal source of atmospheric noise, have been extensively studied.¹⁻³ While there is a wide diversity of specific details in these measurements, there is agreement as to the general structure of these discharges. A basic cloud-to-ground discharge consists of a series of short current pulses associated with the advance of the ionization of the air dielectric along the incipient discharge path, followed by cloud-to-ground movement of the electric charge which created the initial potential difference. Figure 1-1(A) shows the radiation from such a basic discharge with the ionization noise and large cloud-to-ground pulse clearly observable. This oscilloscope photograph was made at the amplified output of a broadband loop antenna with -3 dB bandwidth of 15 to 85 kHz. Maxwell³ reports that the spectral energy of the initial ionization burst, termed the leader stroke, is centered at 30 kHz, whereas the main stroke, termed the return stroke, has a peak of spectral energy in the region of 3-8 kHz. The leader stroke has been observed to have an average length of 1 msec, whereas the return stroke falls in a 100-200 μ sec category.

A large number of discharge events, perhaps a majority under conditions of large, high energy storm cells, are composed of complicated repetitions of the basic discharge just described. Repeated return strokes are termed multiple discharges and have been observed to consist of 20-30 such strokes lasting for periods of 200-500 msec.^{1,4} Figure 1-1(B) shows several return strokes occurring in a short time frame, while 1-1(C) shows a longer segment of a multiple discharge.

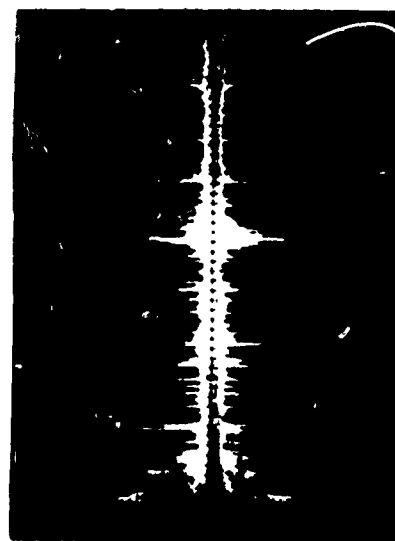
Figure 1-1. Examples of Lightning Discharge Radiation



(A) 100 usec/cm



(B) 50 usec/cm



(C) 10 msec/cm



(D) 5 msec/cm
Upper: $f_c = 65$ kHz; Lower: $f_c = 14$ kHz

Noise bursts caused by lightning discharges, recorded on Tektronix 249 Storage Oscilloscope. (vertical uncal)

Of particular interest to our work is the fact that these more complicated discharge patterns have a "leader" type pattern that becomes a continuum noise burst rather than a series of identifiable strokes or events. Since this leader structure has a principal spectral energy above 30 kHz, whereas the return strokes are centered below this frequency, we would expect significant differences in the time structure of noise waveforms observed at different frequencies with respect to 30 kHz. This is indeed often the case, as is seen in Figure 1-1(D). This tendency of complex discharge events to appear as continuous noise bursts has been noted by many experimental workers.^{4, 5} Gupta⁴ provides comparative tracings of single and multiple discharge noise patterns observed at the output of a narrow-band filter followed by an envelope detector. These tracings, made at frequencies in the MF and HF region, clearly show the complicated burst structure of both the single and multiple discharge phenomena.

We have been, up to this point, implicitly considering the structure of lightning discharges observed near the source where we may assume single mode (ground-wave) propagation from source to observer. In determining the total observed atmospheric noise spectrum one must also consider propagation effects which are very significant and change radically from VLF to LF, and above. The sum total of these effects is given by Maxwell³ in determining the broad spectral characteristics of atmospheric noise. All of the work in this area has been summarized by Oh⁶ who provides a plot from kHz to GHz of relative noise intensity and the references for measurements at various frequencies. We shall not be concerned with these relative levels of atmospheric noise; rather,

we have sought to provide a qualitative background on the nature of the discharge process to motivate our conceptual approach to the problem and to point out the fundamental changes in structure that occur with frequency. These changes and the effect of propagation will be seen in many of the measurements to be reported in Chapter 2.

1.2 Experimental Noise Data

The statistical measurement of atmospheric radio noise that has been most often reported in the literature is the exceedance probability (one minus the cumulative probability) of the noise envelope at the output of a bandlimiting filter. A representative but not exhaustive list of such work is given by references 1, 2, 5, 7-13, 30. The major reason for the use of this characterization is its ease of measurement with relatively simple analog circuits, threshold detectors, and counters. Evans⁸ and Coon⁹ recorded noise waveforms on analog tape recorders and later derived these measurements from digital computer processing of the sample records. The exceedance probability is usually plotted on Log-Log versus Log paper where a Rayleigh distribution appears as a straight line of slope 2. From these measurements workers have concluded that the atmospheric noise waveform consists of a low amplitude Rayleigh component (implying a low-amplitude, gaussian-distributed component in the narrow-band waveform) with a large amplitude component due to distinct or dominating lightning bursts. Most workers have used a log-normal or $1/y^a$ probability density function to fit the observed large amplitude excursions.

The only statistical characterization of the time structure of

atmospheric noise waveforms that has been reported⁷⁻⁹ has been some type of level crossing measurement. Generally this takes the form of a probability density for the time until a given level is crossed in the upward direction by the noise envelope, given that an upward crossing occurred at time zero. The principal conclusion from these measurements has been that the discrete discharge events, assumed to be detected by such a measurement, are not independently distributed in time (a Poisson process) but rather tend to cluster, i. e., there is a higher than expected probability that another event will occur after an initial event has been detected. This effect is a manifestation of multiple discharge phenomena.

In considering what type of statistical parameters to measure to characterize the time structure of atmospheric noise, one must bear in mind that a theoretically infinite set of probability distributions is required to completely describe this structure. The usefulness of any particular parameter selected can only be judged in relation to its end use. While level crossing measurements are quite illuminating of the temporal behavior of discharge events, it is not clear that they are equally useful to the receiver engineer, especially at higher band-center frequencies where the complex leader structure becomes dominant. As will be seen in Chapter 2, we have selected a much different characterization of atmospheric noise time structure.

1.3 Proposed Noise Models

1.3.1 Impulse Model

A number of different models for atmospheric noise waveforms have appeared in the literature over the past 15 years. The majority of these

might be termed "impulse models" for they derive their motivation from an approximation of the actual generating mechanism by an impulse train exciting the narrow-band observation filter. One might also term them physical models because the model parameters can usually be closely linked to physical quantities or filter parameters. The classic model of this type is that given by Furutsu and Ishida.¹⁰ Their model includes not only a Poisson distributed wave of impulse functions of random energy, but further Poisson distributed pulse bursts following a basic impulse. They were concerned with MF and HF atmospheric noise and this type of model accounts for the complex leader or continuum structure dominant at these frequencies. The general approach^{10, 14, 15} to the determination of noise statistics at the output of the observation filter, for this type of model, has been to use Price's technique with characteristic functions to determine the first order and higher probability densities in the characteristic function domain. The resulting expression cannot in general be transformed to yield a probability density function (pdf) except at the large and small amplitude limits. The noise model given by Beach² is of this impulse type and is the most complex model that we are aware of, including a number of different rate parameters for weather patterns, time-of-year, etc. Beckman¹¹ utilizes a different approach with much the same result in terms of the envelope pdf. These models are well suited for the inference of physical parameters (such as storm cell distribution or propagation parameters) from observed noise waveforms but are difficult to use for receiver engineering, nor do they provide insight into the actual noise structure on which the receiver processor must operate. An exception to this

-24-

seems to occur for ELF noise waveforms as considered by Evans⁸ and Modestino¹⁴ where, due to the frequency (3-300 Hz) and bandwidth, the noise is completely dominated by the return stroke phenomena which at this bandwidth is well modeled by an impulse function. Snyder¹⁶ also uses an impulse model as a vehicle for the derivation of the optimum estimator equations for a binary detection receiver. Snyder's approach is only dependent upon structure, avoiding any explicit reference to probability distributions. However, the resulting equations form an infinite set of coupled partial-differential-integral equations which are as difficult to exploit¹⁵ as the determination of the complete model statistics at the filter output.

1.3.2 Communication Models

A number of atmospheric noise models have appeared in the communications literature¹⁷⁻²⁰ and have been directed towards receiver design. A principal feature of these models is that they attempt to describe the noise waveform at the output of the bandlimiting filter with only peripheral concern for the underlying generating mechanism. Kapp¹⁷ utilized a "switched process" model, originally due to Kurz, in which the observed waveform was given as either a bandlimited gaussian process or an impulsive process with first order Cauchy pdf. The probability of "finding" one or the other of these distributions is then a measure of the impulsiveness of the noise waveform.

A much different model was given by Shaft¹⁷ in which the envelope of the narrow-band process is given as $\text{EXP}(n(t))$, where $n(t)$ is a gaussian process. This expression only provides correct large amplitude

behavior of the model; however, Shaft reports satisfactory application of the model to the prediction of VLF modem performance.

1.3.3 Multiplicative Noise Model

Hall¹⁸ proposed a model in which the narrow-band noise waveform at the filter output is given as $y(t) = A(t) \cdot n(t)$, where $n(t)$ is a conventional gaussian process and $A(t)$ is a lowpass random process. The time structure of $n(t)$ is that obtained by illuminating the bandlimiting filter with white noise. The modulating process, $A(t)$, is used to increase the dynamic range of the basic gaussian process to match that exhibited by atmospheric noise waveforms. At the same time, the time structure of $A(t)$ is available to imitate the complex time behavior of the discharge process. Hall demonstrated that with an assumed generating mechanism (which will be covered in detail in Chapter 3) the first order statistics of either the envelope or the narrow-band rf process could be expressed in closed form for his model and that this form matched quite well the various reported exceedance probability distributions of the noise envelope.

Recalling the discussion of the complex nature of the discharge event, in particular, the tendency at LF and above for the noise mechanism to be dominated by the leader or fine structure, we see that there is considerable motivation for the multiplicative noise model. The modulating process, $A(t)$, we can associate physically with the fluctuating power level of the atmospheric noise at a receiving site, caused both by different sources and the long noise burst characteristics of multiple discharges at individual sources. The use of $A(t)$ to

to model these effects at the filter output offers the possibility of approximating the very complex behavior of the lightning discharge process by a simpler description of a random generating mechanism for $A(t)$.

Another concept that we have evolved in considering this type of model is that $A(t)$, modeling the envelope of the broadband discharge process, should be common to noise waveforms observed in nearby but disjoint frequency channels. Noting that our final goal is the use of the model in receiver design, this concept has considerable importance for if one knew $A(t)$ exactly, then the corrupting noise waveform would become a time-varying or non-stationary gaussian process. Existing signal processing designs generally include time-varying gaussian noise as the most general case, and hence the difficult, non-gaussian, atmospheric noise problem would have the potential for being converted to a much more tractable time-varying gaussian problem. While there have been a few references in the literature^{21, 22} to using information from adjacent frequency channels, these are based on an assumed deterministic relationship between noise waveforms, that both are generated by an ideal impulse exciting the respective filters. Our postulated model appears to be the first attempt at modeling a statistical relation between such waveforms.

We began the experimental phase of this research by approaching the design of a data collection system to answer certain questions about the suitability of such a conceptual multiplicative model. The specific measurements, the system designed to obtain these, and the analyzed results are given in the next chapter.

EXPERIMENTAL DATA

In Chapter 1 we discussed the nature of electromagnetic radiation from lightning discharges as it affects low-frequency radio noise. From this discussion and a review of past efforts at modeling the noise process, we postulated a multiplicative noise model as suggested by Hall.¹⁸ This model is given as $y(t) = A(t) \cdot n(t)$, where $y(t)$ is the output of a bandlimiting filter excited by received atmospheric noise fields and represents the waveforms that must be processed by the receiver. The term $n(t)$ is a conventional narrow-band gaussian process and $A(t)$ is a lowpass random process. This conceptual form of model had two appealing features for our requirement of a noise model that was particularly useful for receiver design: 1) The modulating process $A(t)$ could be used to absorb the very complex, long-time nature of the actual discharge process which is broadband and excites all nearby frequency channels; 2) a knowledge of or good approximation of $A(t)$ would convert an untractable non-gaussian noise problem into a much simpler time-varying gaussian problem for which optimum solutions are known. In this chapter we describe an experimental program formulated to answer the two basic questions raised by point 1) above: Are the actual noise waveforms amenable to these interpretations? Our purpose in this chapter is to provide a broad overview of the measured noise characteristics prior to detailed development of a mathematical model and comparison of model characteristics with the observations.

2.1 Noise Characteristics Measured

The instrumentation system that was constructed for this work is described in section 2.2 below. This system was designed to measure the following statistical characteristics of bandlimited atmospheric noise waveforms at frequencies of 14, 65, and 83 kHz and bandwidths of 1, 10, and 20 kHz.

1) Probability Density. Noise waveforms were sampled at periods of 1 to 20 milliseconds with sample records of 10^5 samples. These were analyzed to estimate the noise probability density (pd) using a rectangular approximation over small intervals.

2) Joint Probability Density. Simultaneous samples of a noise waveform in frequency channel one and the noise envelope in a non-overlapping frequency channel two were recorded. These were analyzed to estimate the joint pd surface and various conditional statistics of these two, dependent, variables.

3) Conditional Sampling. Samples of noise waveforms were taken, conditioned by hardware upon a given event in another channel, to reinforce the measurements of (2).

4) Autocorrelation. The autocorrelation of the noise waveform was measured by sampling the waveform at an integral multiple of the band-center frequency period and autocorrelating the resulting record.

5) A(t) Estimates. To generate an estimate of the short-term power level of the atmospheric noise, represented by A(t) in the model, we integrated the absolute value of the noise waveform

$$A(t_i) = \frac{1}{\Delta T} \int_{t_i}^{t_i + \Delta T} |y(t)| dt$$

for fixed time periods of 1 and 10 msec. It is well known²⁶ that a statistically optimum estimate of an unknown, gaussian noise, power level is given by an average of the observations squared. However, for atmospheric noise waveforms with a dynamic range in excess of 80 dB this requires squaring circuitry with a dynamic range of 160 dB, which is presently unattainable. The use of the magnitude was selected as a realizable alternative. These estimates of $A(t_i)$ were made in two frequency channels simultaneously and used to determine the auto and cross-channel correlation of $A(t)$.

The exact computational algorithms used to realize these estimates and approximate error analyses are given in Appendix B.

2.2 Instrumentation System

A functional description and performance measurement of the instrumentation system is given in Appendix A. The basic functions of the system are described below.

1) Analog Processing. Atmospheric noise fields were received on a one-meter loop antenna, amplified, and filtered with a bank of LC notch filters to remove possibly saturating communication signals. The notch filtered signal was bandlimited to four channels by fixed tuned LC filters. The dynamic range of the system to this point was greater than 100 dB, with system noise better than 6 dB below the quiescent or background atmospheric noise level. These four channels were processed through two wide-band amplifier samplers or two rectify-integrate-hold circuits. The sampler dynamic range was greater than 80 dB, with a 600-nsec gate, and included appropriate offset adjustments. The active

rectifier circuits had a linear range of 76 dB. The rectifier outputs could also be fed to a 20-kHz lowpass filter and thence to the wide-band samplers for envelope data collection.

2) Digital Processing. Digital processing began with a 1 MHz ultra-stable crystal oscillator, which was used as a system clock to control all sampling and data handling functions. A wide variety of sampling modes could be generated, from rates of 100 kHz to 0.1 Hz and in continuous or burst patterns. Special circuits allowed coarse synchronization of the sampling pattern with received pulse signals from the Loran-C navigation system²⁸ so that noise data could be taken at this operating frequency (100 kHz) without signal contamination. The four sampled analog channels could be connected to the Analog-to-Digital converter, in various periodic sequences, to provide 15 bit, ± 10 volt digitizing capability to all channels. Digitized data was stored in an 8K by 16 bit core memory prior to asynchronous recording on paper tape.

3) Data Recording. Digital data was recorded on a 1K bit-per-second paper tape punch for convenient input to the small computer system used throughout this research program. Data flow was asynchronous from the buffer memory via an optical isolator to prevent transient contamination of the analog system.

A complete description of parts (2) and (3) of the data system is given by Lee.²⁴

2.3 Classification of Observations by Weather Conditions

The instrumentation system was extensively tested on known deterministic and random signal sources as described in Appendix C. Prelim-

inary recording and analysis of atmospheric noise was conducted at Cambridge, Massachusetts during July 1971. The complete data record on which the remainder of this work is based was made during the period 10 August to 22 August 1971 at the United States Coast Guard Electronics Engineering Center, Wildwood, New Jersey, which is located 90 miles from the nearest urban area. The loop antenna was mounted on top of a single story concrete block building approximately 1/4 mile from the ocean. The antenna reception null zones were oriented to minimize received signals from the Loran-C transmitting stations at Nantucket, Massachusetts, and Cape Fear, North Carolina.

During the data collection period the Eastern Seaboard experienced three distinct types of weather patterns that were highly correlated with the observed atmospheric noise characteristics. For convenience in referring to the different noise conditions, we have termed the three basic weather/noise conditions "quiet," "tropical," and "frontal." The frontal condition occurred on 11 August 1971 and was caused by an advancing cold front with extensive thunderstorms along the squall line. Heavy rain and visual lightning passed over the observation site 3 hours after the frontal data was recorded. The weather during the next week was dominated by a high pressure air mass that had caused the frontal conditions. This air was cool and stable with very little thunderstorm activity and produced the quiet conditions. As this weather pattern moved to the east, a flow of warm, moist, unstable air from the Gulf of Mexico overspread the East Coast. This tropical weather period had a high geographic density of thunderstorm activity, especially in the afternoon at the time of maximum accumulated energy in the vertical

air thermals. As will be seen, the quiet noise conditions were quite close to being gaussian and hence these, or gaussian conditions, represent probably a majority of year 'round noise conditions in temperate latitudes. The tropical conditions we would describe as typical "dog days of August" weather that one experiences during the East Coast summer. The frontal conditions, producing severest noise conditions, were only observed at five distinct times during the July-August period that we made observations and were all associated with frontal weather patterns. Frontal noise, then, represents atypical temperate latitude behavior, but is possibly representative of more common conditions in equatorial regions.¹² In addition to these three basic noise conditions, a transitional condition was observed during the night when the tropical air flow was moving over the middle Atlantic region. This is labeled "quiet-night" in what follows.

Our sample of atmospheric noise conditions, while taken in a relatively small time frame, is probably representative of a wide variation of noise conditions that one would find throughout the world. This statement will be given more meaning in Chapter 3 where we shall observe that the various noise conditions can be related to extreme ranges in important model parameters.

2.4 First Order Probability Density of Atmospheric Noise

2.4.1 Single Frequency Channel Probability Density

The range of the first order pd of a bandlimited atmospheric noise waveform, at VLF and LF, is shown in Figure 2-1. These observations were made at each frequency with different gains which attempted to

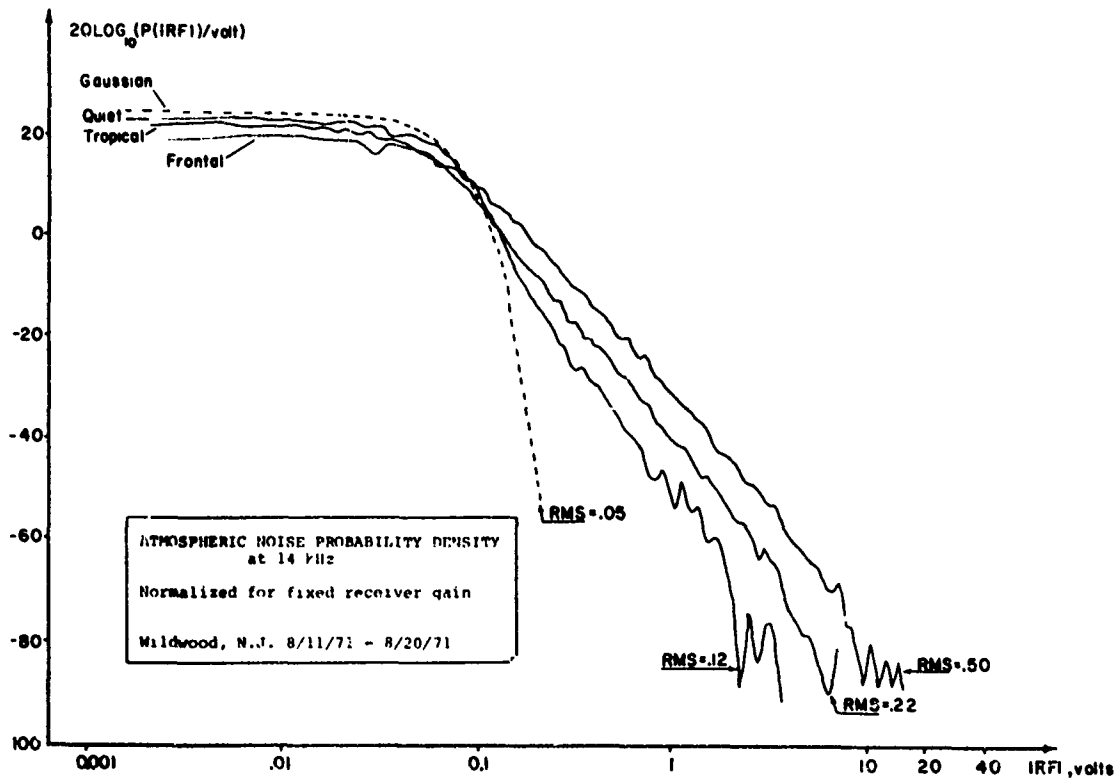
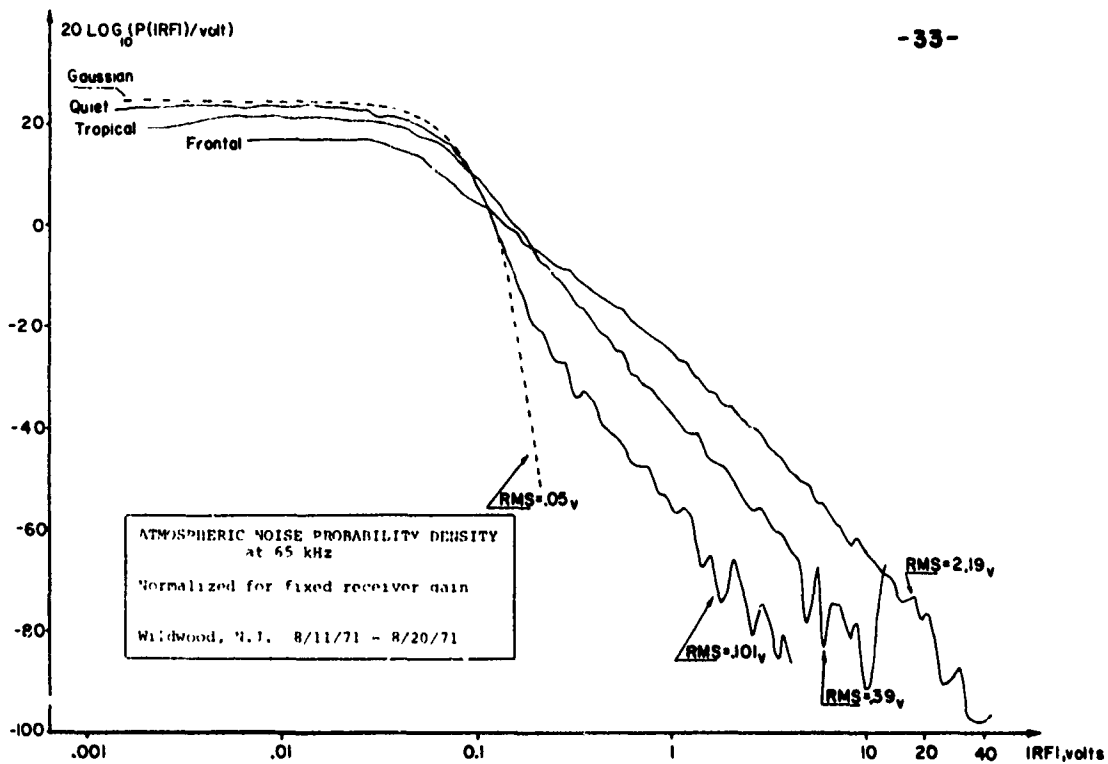


Figure 2-1. Noise Probability Density at VLF and LF

optimize use of the 80 dB dynamic range of the A-D converter. The combined plots were made by removing the differential scale factor, resulting in a pd that would have been measured by a fixed gain system of greater dynamic range. The scale factor between frequency channels is arbitrary, no attempt was made in this work to determine relative noise levels between frequency bands (see Maxwell,³ Oh⁶).

The most striking factor in these plots is the wider variation in pd's at LF (65 kHz) than at VLF (14 kHz). This is a consequence of two physical factors,³ propagation and the frequency dependence of the discharge characteristics. Propagation attenuation is a factor of 10 greater (@ 8000 KM) at 65 kHz compared to 14 kHz, increasing to a factor of 100 at 100 kHz.³ Thus the received atmospheric noise field at VLF is sensitive to a much wider geographic area than at LF. At the New Jersey observation site this meant that the 14 kHz observations, during quiet conditions, included discharge effects from much farther south, regions of greater thunderstorm activity than affected the 65 and 100 kHz observations. During the frontal observations, the received noise field was dominated by the intense lightning activity along the cold front squall line. At this time, the long multiple discharge phenomena produced a near continuum of noise at LF and above, while the VLF noise consisted principally of distinct pulses from the return stroke (see Figure 1-1(D)). These observations support our qualitative analysis of expected differences in VLF and LF noise waveforms.

Several workers have suggested^{6, 18, 25} that a bandwidth of 10 kHz plays an important role in the behavior of atmospheric waveforms. The arguments given involve the dependency of peak value of a noise burst

on bandwidth, with 10 kHz being the point at which this dependence changes from a linear relation to a square root relationship. This prediction is based on a comparison of the average length of a return stroke (100 μ sec) to the effective filter impulse response time, and a consideration as to whether the discharge appears as a noise burst or an impulse. It is not clear what effect this consideration has on the noise pdf, however, our observations at LF show no important difference in noise pd's measured at 1, 10, and 20 kHz bandwidths. Figure 2-2 shows the noise pd at 65 kHz, in 1 and 10 kHz bandwidths, plotted on a normalized amplitude scale illustrating this fact.

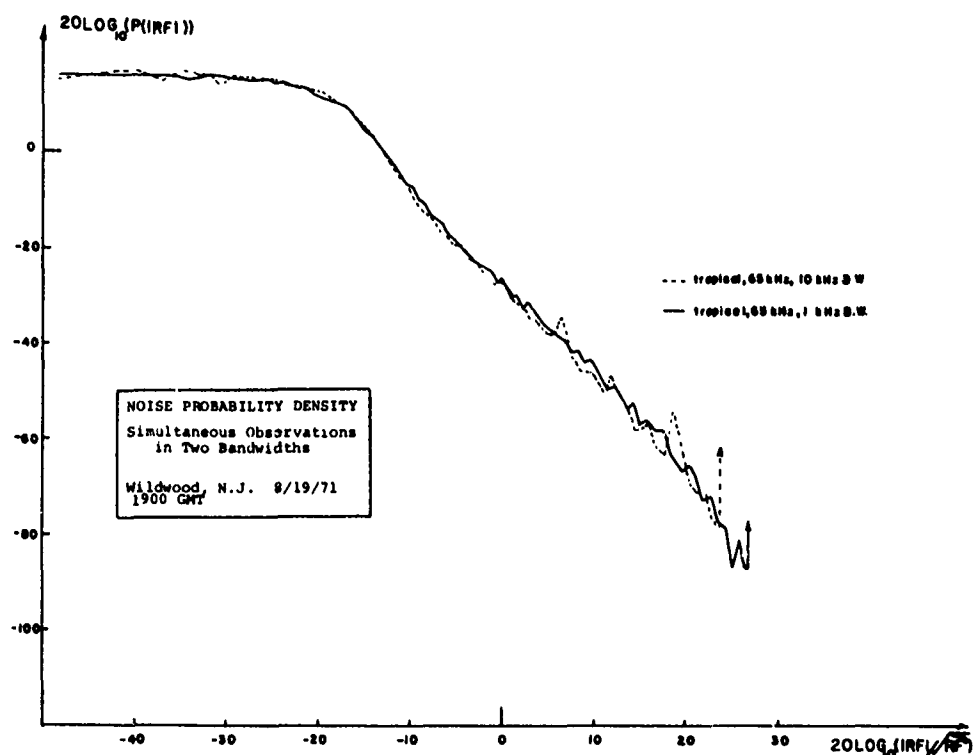


Figure 2-2. LF Noise pd's Observed in 1 and 10 kHz Bandwidths

We believe this behavior is attributable to the importance of the leader stroke component of the noise burst, which for a single discharge has an average length of 1 msec. One would suspect, if this is the case, that observations made in bandwidths much less than 1 kHz would show significant differences, however, we have not made any observations at these bandwidths. We shall discuss the role of filter bandwidths less than 1 kHz in Chapter 3 as they significantly affect signal processing structures. However, in the remainder of this chapter, we shall treat all of the LF data as equivalent at the three observations bandwidths of 1, 10, and 20 kHz with only notations on the figures to indicate the bandwidth used. All of the data recorded at 14 kHz was taken in a 1 kHz bandwidth.

2.4.2 Joint Frequency Channel Probability Density

As we have noted, a principal feature of the multiplicative noise model that we have postulated is that the modulating random process, $A(t)$, is common to nearby but disjoint frequency channels. To explore this concept we recorded samples of the bandpass noise in one frequency channel, termed the rf channel, and the bandpass envelope in an adjacent frequency channel, termed the envelope or pilot channel. The decision to use the envelope as a short term measure of the fluctuating power level rather than the $A(t_i)$, used to estimate the dynamic properties of $A(t)$, was based on tests to determine which of these parameters had the highest correlation coefficient with the magnitude of the bandpass noise. The results of these tests are shown in Figure 2-3 where the use of the envelope is seen to result in a slightly larger cross-correlation coefficient.

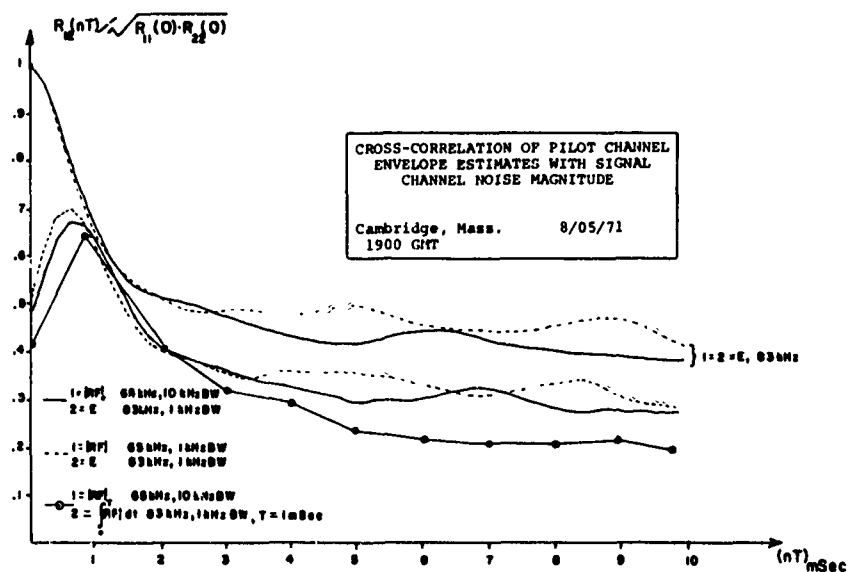


Figure 2-3. Correlation of RF Noise Magnitude with Various A(t) Estimates

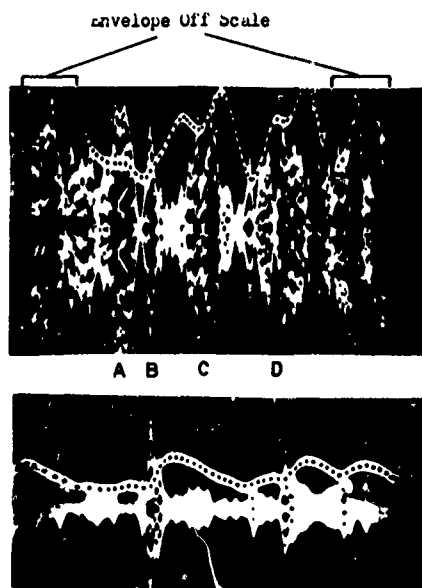


Figure 2-4.
Sample Waveforms from
RF Channel and Envelope
Channel

Simultaneous recording of 65 kHz RF
channel noise and 65 kHz Pilot Channel
envelope (dots added) on storage Oscil-
loscope, 1 msec/cm, 200 mV/cm both traces

Figure 2-4 shows two oscilloscope photographs of the pilot channel envelope and rf channel noise for a multiple discharge and scattered low level single discharges. Inspection of the relationship of the pilot channel envelope (dots were added to distinguish this trace) shows that this envelope does not "follow" the rf noise level in a simple deterministic manner. For example, the four large rf bursts labeled A, B, C, and D do not have the same response in the pilot channel. In principle, if we knew the state of the respective rf, and the pilot channel bandlimiting filters at some time and the exact form of the broadband atmospheric noise excitation for future time, we could calculate these responses deterministically. The implicit assumption of our multiplicative noise model is that we do not have this information; we seek rather a noise model that describes these relationships in an average or statistical sense. It would appear from these photographs that our concept of a multiplicative noise model, with $A(t)$ independent of frequency, would provide a plausible basis for modeling these relations.

RF channel and pilot channel waveforms, such as those seen in Figure 2-4, were sampled at 1 kHz rates in bursts of approximately 10 seconds. The burst length was determined by input/output rate and memory capacity of the instrumentation system. The pilot channel sample was taken 0.7 msec after the rf sample to compensate for the differing group delays in the respective bandlimiting filters. This delay difference produced the lag in the cross-correlation peak seen in Figure 2-3 and the obvious delay seen in the photographs of Figure 2-4. The pilot channel center frequency was 83 kHz with a 0.9 kHz bandwidth for all recordings, whereas rf channels were located at 65 kHz with 1 and

and 10 kHz bandwidths and 100 kHz with a 20 kHz bandwidth. Appendix A provides a description of these filters. For the 100 kHz record, sampling bursts were restricted to 30 msec in length and were time-interlaced with the on-air, pulsed, Loran-C navigation²⁸ signals. Joint channel sample records were not made at VLF frequencies.

These joint channel sample records were used to estimate the joint probability density surface for rf samples from channel 1 and envelope samples from channel 2. The analysis algorithm is given in Appendix B. The probability density surface is shown in Figure 2-5 for quiet and frontal conditions. For the quiet data, we see that the surface for most rf and envelope levels shows no correlation; it appears as a product of an envelope type density and an rf density. At large envelope values, however, the conditional rf density (a line of constant envelope value) begins to shift to the right, indicating larger rf values are more probable at increasing values of the pilot channel envelope. The frontal surface shows much the same behavior, except that the dependency of the rf density on the conditioning envelope value extends over nearly all of the observed range of these variables. In Figure 2-6, the joint probability surface for tropical conditions is shown, and exhibits a dependency behavior intermediate between the quiet and frontal surfaces. Figure 2-6 also shows the one data recording made of joint envelope dependency between two frequency channels. The movement of the peak of the envelope density, parallel to the conditioning envelope axis and then to the right for larger values, provides a clearer indication of the nature of the statistical interrelation between noise waveforms in disjoint channels.

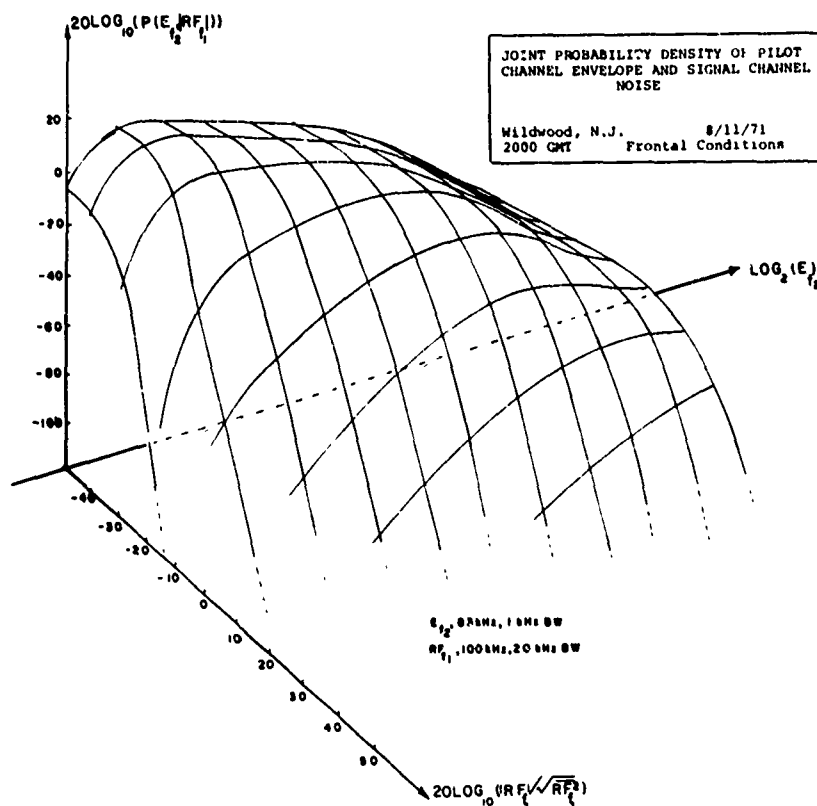
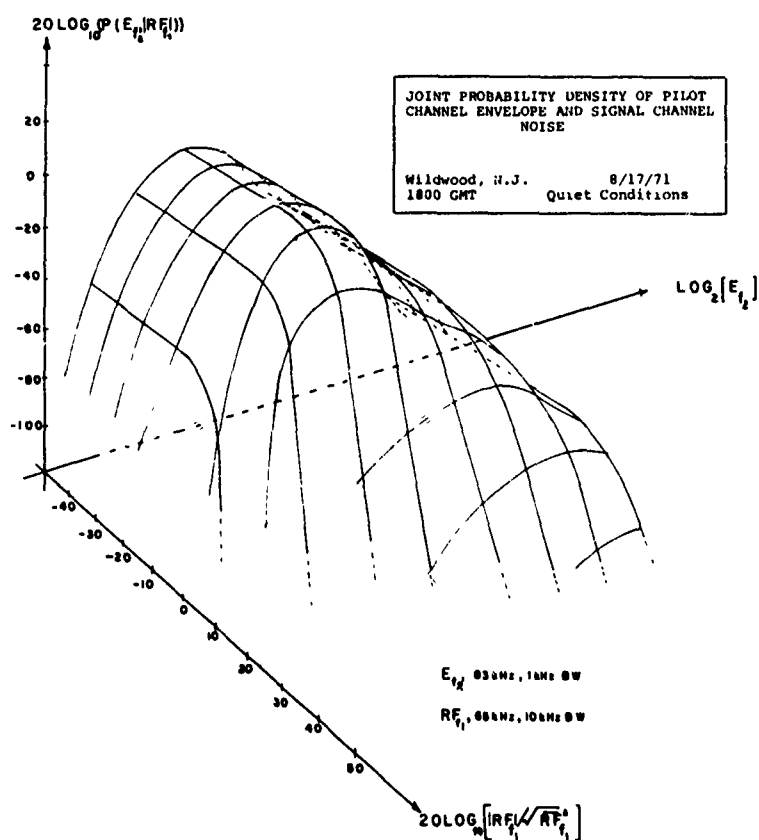


Figure 2-5. Joint Probability Surface

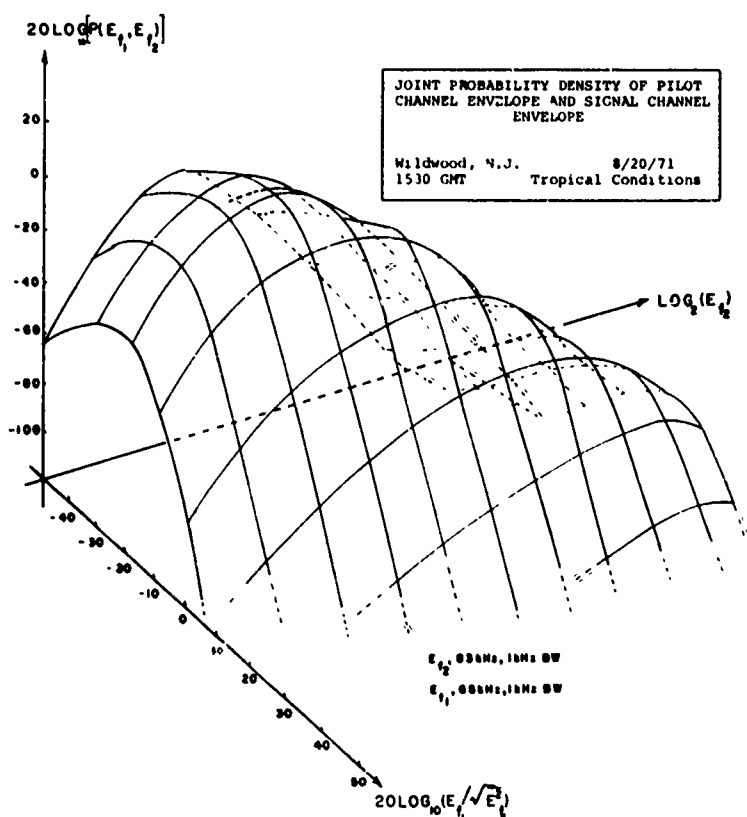
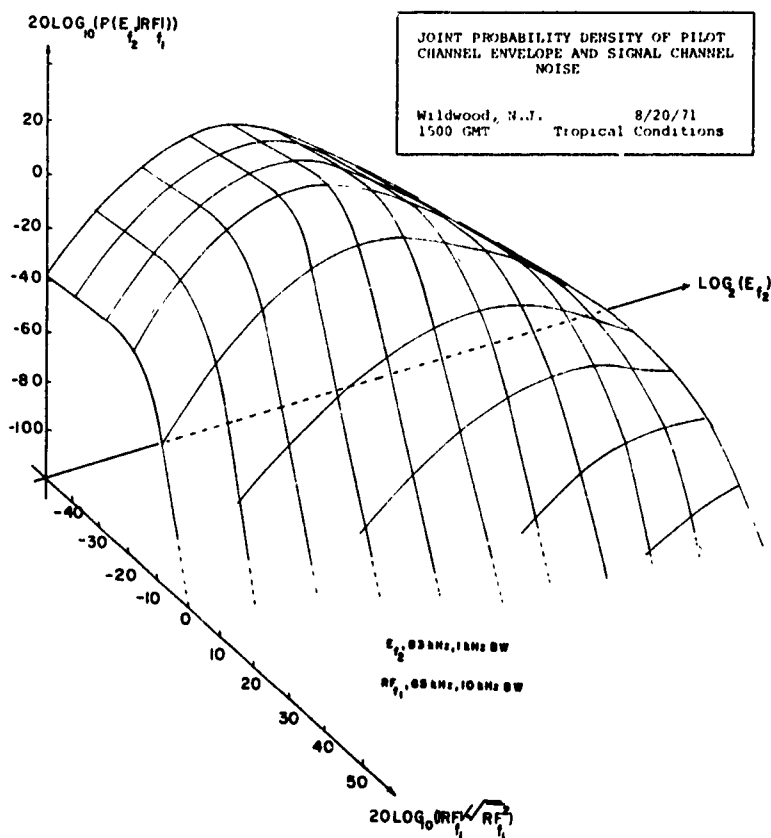


Figure 2-6. Joint Probability Surface for Tropical Conditions

A more intuitive measure of this interrelationship, that can be displayed in two dimensions, is the standard deviation of the rf noise waveform, conditioned on the value of the envelope in the pilot channel. For our discrete sample record this is given as

$$\sigma_{RF_{f1} | E_{f2}(h)} = \left[\frac{1}{N(h)} \sum_{i=1}^{N(h)} RF_{f1}^2(i | E_{f2}(h) < E_{f2}(h) \leq E_{f2}(h) + \Delta E) \right]^{1/2} \quad (2.1)$$

Plots of this joint channel statistic for various noise conditions and bandwidth are shown in Figure 2-7. These plots were computed directly from the raw data, not smoothed estimates used in the joint density surfaces. Note that the relative scale factors used for different data records, removed in Figure 2-1, are present here. The horizontal portion of each of the plots in Figure 2-7 corresponds to the region of the joint density surface where there is no statistical dependence between channels. Physically, this portion is due to the background atmospheric noise component where one cannot identify the effect of any single discharge. The rising portion of the plot corresponds to those components of the noise waveform that are clearly influenced by a dominant lightning discharge, and a linear dependence is seen in this joint channel statistic. It is also important to note that this linear dependence holds for all noise conditions, from quiet, where only 10% of the samples fall in the correlated region, to frontal, where 90% fall in this region.* The nature of the joint channel noise dependence will be considered in greater detail in Chapter 3 in connection with the mathematical noise model.

*The method used to determine these percentages is given in Chapter 3.

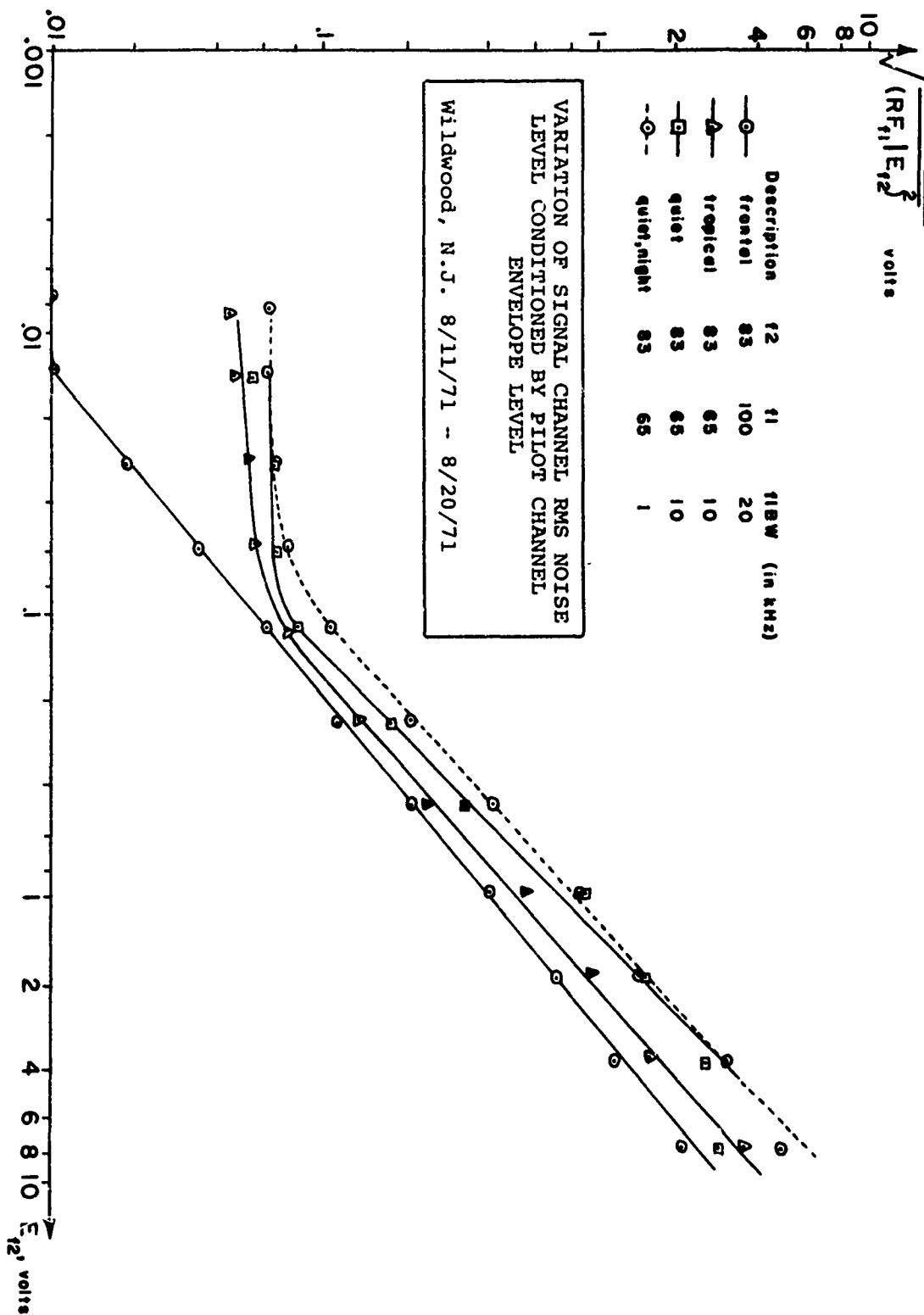


Figure 2-7. Standard Deviation of RF Channel Noise Conditioned by Pilot Channel Envelope

2.5 Time Structure of Atmospheric Noise

2.5.1 Power Spectral Density

A large number of experimental observations⁶ show that broadband atmospheric noise has an approximate $1/f$ dependence from 10 kHz to 200 MHz. When such noise is observed through a narrow-band filter, we would expect that the noise at the filter input may be considered to have a flat power density spectrum (white noise) across the effective filter bandwidth. Thus the power density spectrum of the bandlimited noise should be proportional to the filter response magnitude squared, or equivalently, the autocorrelation of the bandlimited noise should be proportional to the autocorrelation of the filter impulse response.

To test this hypothesis, the envelope of the autocorrelation coefficient of bandlimited atmospheric noise was measured by sampling the waveform at an integral multiple of the period of the nominal center frequency of the narrow-band filter and autocorrelating this sample record. If one uses Rice's representation for a bandlimited waveform, it is well known²⁷ that the autocorrelation function is given as

$$R(\tau) = R_{aa}(\tau) \cos(\omega_o \tau) + R_{ab}(\tau) \sin(\omega_o \tau),$$

where $R_{aa}(\tau)$ is produced by the power spectral density component symmetric with respect to the frequency, ω_o , and $R_{ab}(\tau)$ by the anti-symmetric component. By choosing the arbitrary center frequency, ω_o , as the fundamental of our sampling frequency (nominally band center) we see that the autocorrelation of our sample record will be

$$R(nT) = R_{aa}(nT),$$

which is the symmetric component of the autocorrelation envelope.

This component of the autocorrelation envelope was estimated, using an 8000-point sample record, for three different filter shapes. The filter was alternately excited by atmospheric noise and a known white gaussian signal source (General Radio Type 1390-B Random Noise Generator). The experimental autocorrelation envelope is shown in Figure 2-8. Two sources of error affected these measurements, slight differences in the sampling frequency, which produce a slightly different symmetric spectral component, and the greater instability of the estimate with atmospheric noise. The first factor produces slightly different shapes of the main lobe at the origin, while the latter produces greater fluctuations in the "long-time" correlation estimates. The results shown in Figure 2-6 appear to confirm the general hypothesis that received atmospheric noise fields may be considered white with respect to typical filter bandwidths. The import of this fact to signal processing problems is that no unique information is conveyed by knowledge of the bandlimited atmospheric noise correlation function, beyond that provided by a white noise assumption.

2.5.2 Time Structure of $A(t)$

The second most important aspect of our experimental investigation, after the measurements of joint channel characteristics, was an estimate of the time structure (dynamics) required of the lowpass modulating random process, $A(t)$, in the multiplicative noise model $y(t) = A(t) \cdot n(t)$. The integrated estimates, $A(t_i)$, were used to explore this behavior. Preliminary tests of these estimators (see Appendix C) indicated that

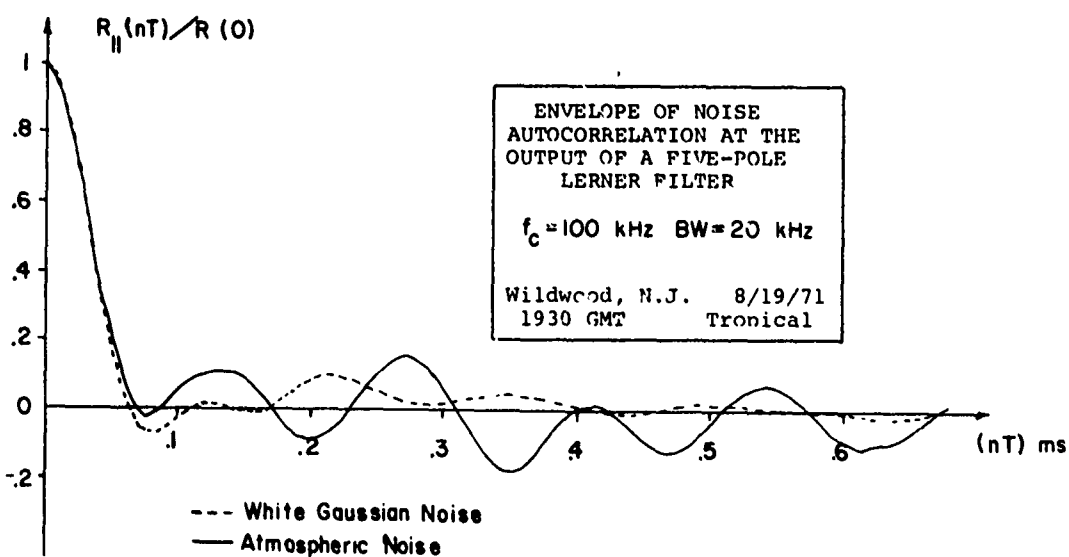
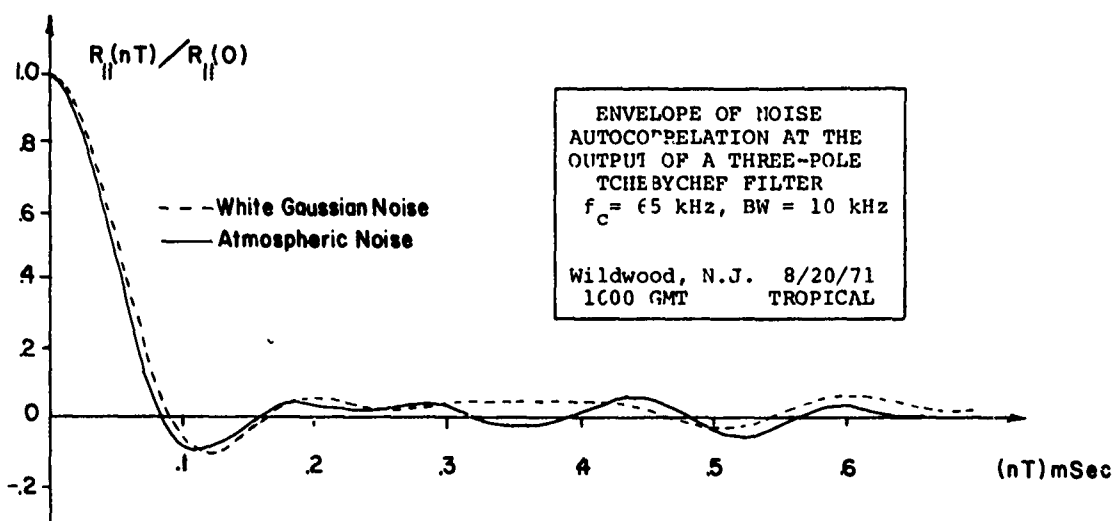
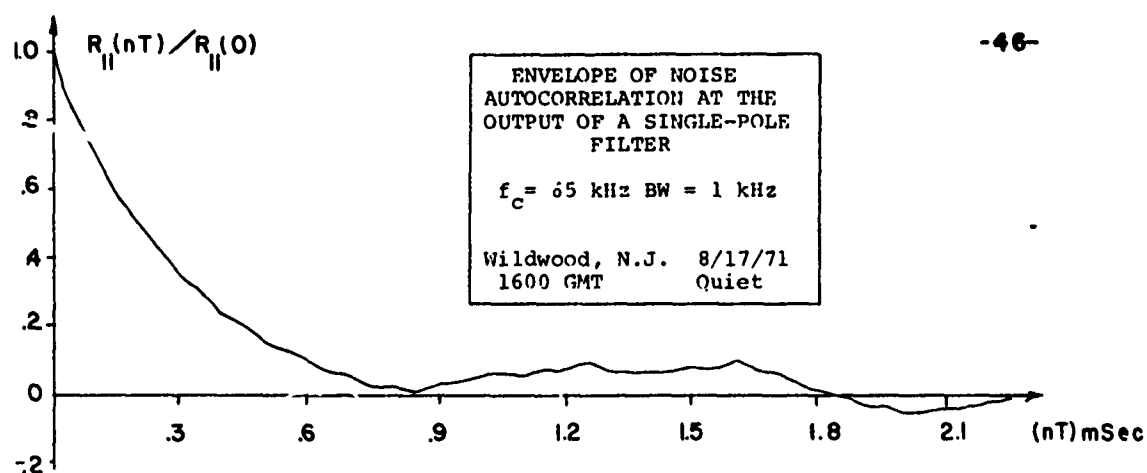


Figure 2-8. Autocorrelation Envelope of Bandlimited Atmospheric Noise

the 1 and 10 msec integration periods provided a low variance estimate of $A(t_i)$ when used with a gaussian signal source and rf bandwidths of 1 and 10 kHz, and clearly exposed a periodic two-state power level used to modulate the gaussian source.

Recordings of the $A(t_i)$ estimates were made for all noise conditions at frequencies of 14, 65, and 83 kHz. The 100 kHz channel could not be used since these $A(t_i)$ records, used mainly for correlation analysis, were made in continuous bursts of 0.5 sec and longer and such lengths would have been contaminated by the pulsed signal groups of the operating Loran-C navigation system. The $A(t_i)$ samples were taken simultaneously in two frequency channels, with the 1 msec integration periods used to study the short-time structure of $A(t)$, and the 10 msec estimates the long-time structure. Physically, this corresponded to emphasizing the structure of single bursts (average time of 1 msec) and multiple discharges (average time 300-400 msec).

Prior to a discussion of the correlation analysis of these $A(t_i)$ records, it is of interest to inspect an actual sample record as shown in Figure 2-9. This is a plot of each sample point (the digitized integrator output at 1 and 10 msec) connected by a straight line, with the appropriate time scale indicated. We see from the upper 1 msec integration time the tendency of the noise fluctuations to cluster in bursts, and also the greater fluctuation of the 65 kHz estimates in comparison with the 14 kHz estimates. This is due to the intense leader structure found at these frequencies and above. The 10 msec sample record makes this behavior more apparent, where there is a somewhat lower range of excursions in the $A(t_i)$ estimates in the 65 kHz trace, but a

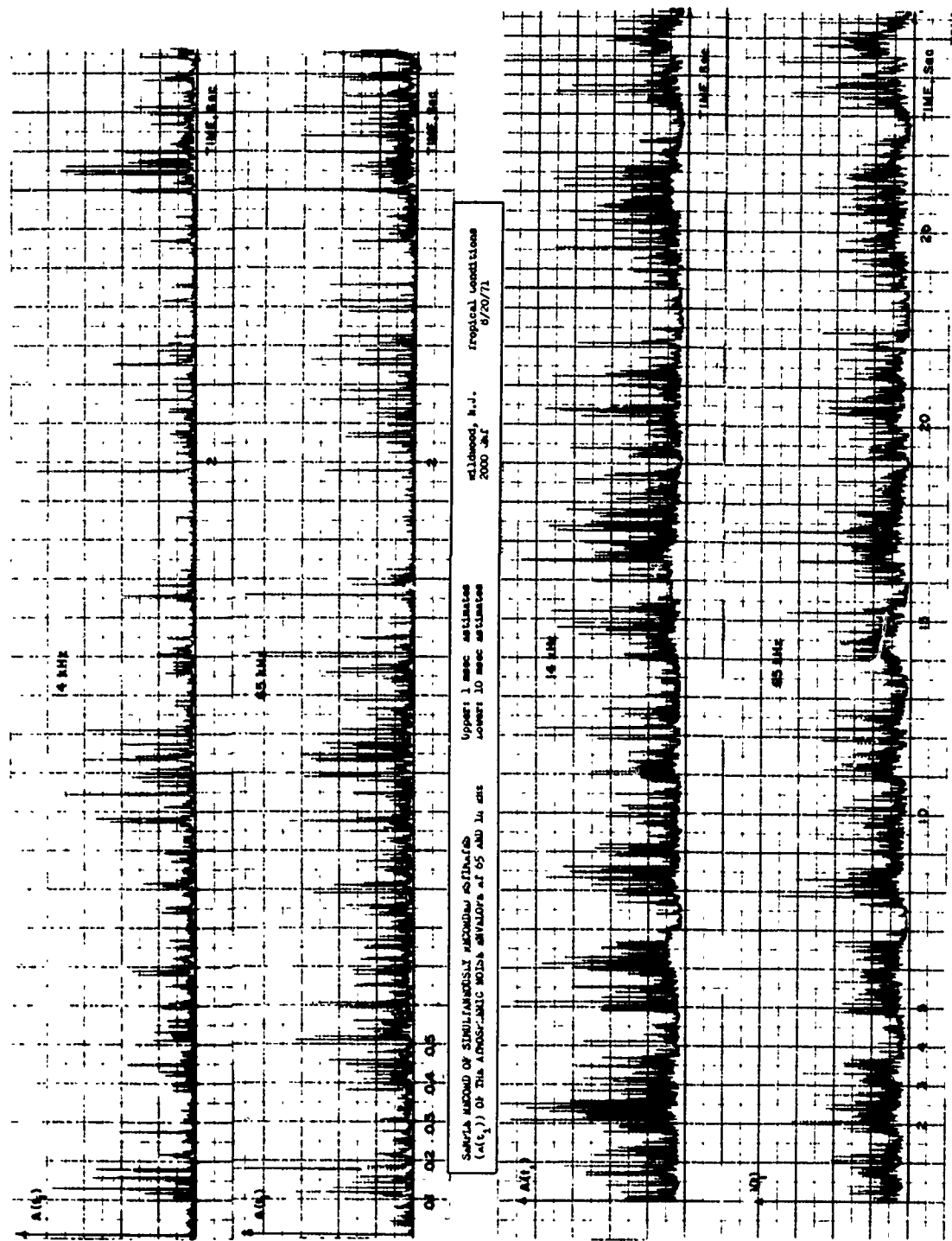


Figure 2-9. Sample Record of $A(t_i)$ Estimates

larger fluctuation in the continuum component. This undulating behavior is suggestive of a lowpass modulating process, with the addition of a larger white or uncorrelated component.

The autocorrelation of the estimates $A(t_i)$ with 1 msec integration times showed the same basic structure under all noise conditions as shown in Figure 2-10. The $A(t_i)$ time series is dominated by an uncorrelated component producing the large discrete impulse at the origin, followed by a small exponential type short time decay component. These records were all made with a 1 kHz bandwidth; however, previous records using a 10 kHz bandwidth showed the same behavior. We attribute this short-time decay to the stochastic length of single discharges, including the leader stroke. The difference between the value of the autocorrelation coefficient at 3-4 msec and that at infinity (computed as the square of the average value of $A(t_i)$) is caused by the presence of long multiple discharges, especially during the tropical and frontal conditions.

The autocorrelation coefficient of the 10 msec estimates, $A(t_i)$, show the exponential type decay due to this long-time feature as seen in Figure 2-10. This figure shows the discrete impulse at the origin, caused by the same impulse measured with the 1 msec estimates plus the short-time correlation component observed there, followed by the long-time decay which has a time constant in the 300-500 msec category. To study this decay component several recordings were made with the start of a sample burst triggered by the 10 msec estimate, $A(t_i)$, exceeding a preset threshold. The 10 msec estimate would only exceed this threshold when a strong multiple discharge had occurred, sufficient to

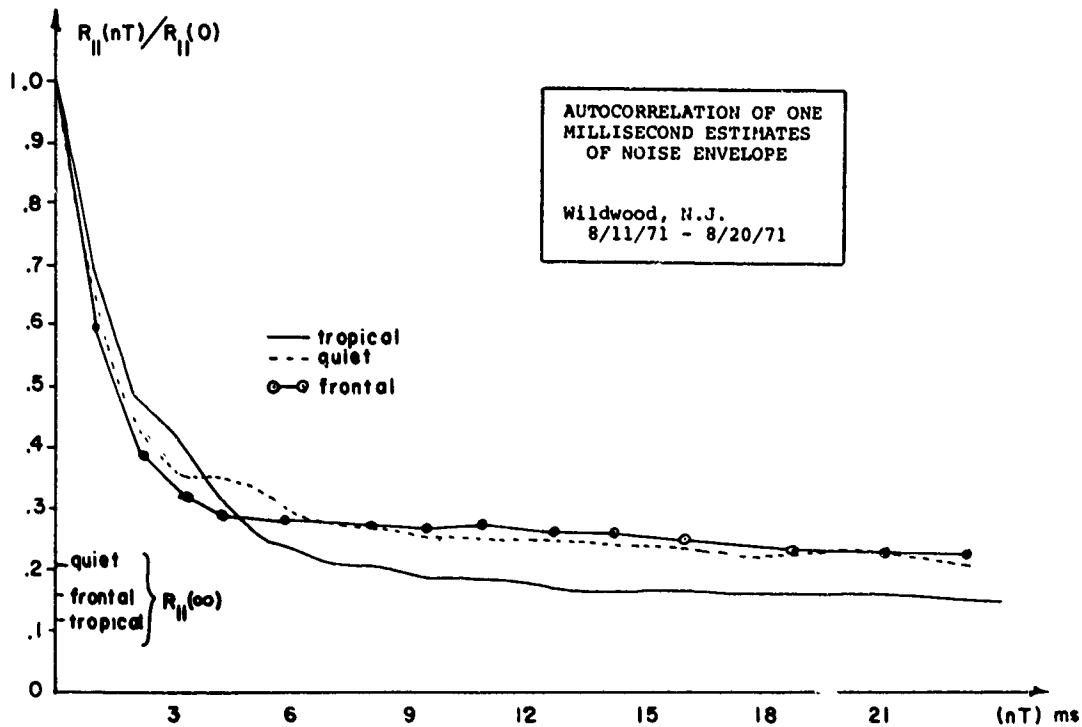
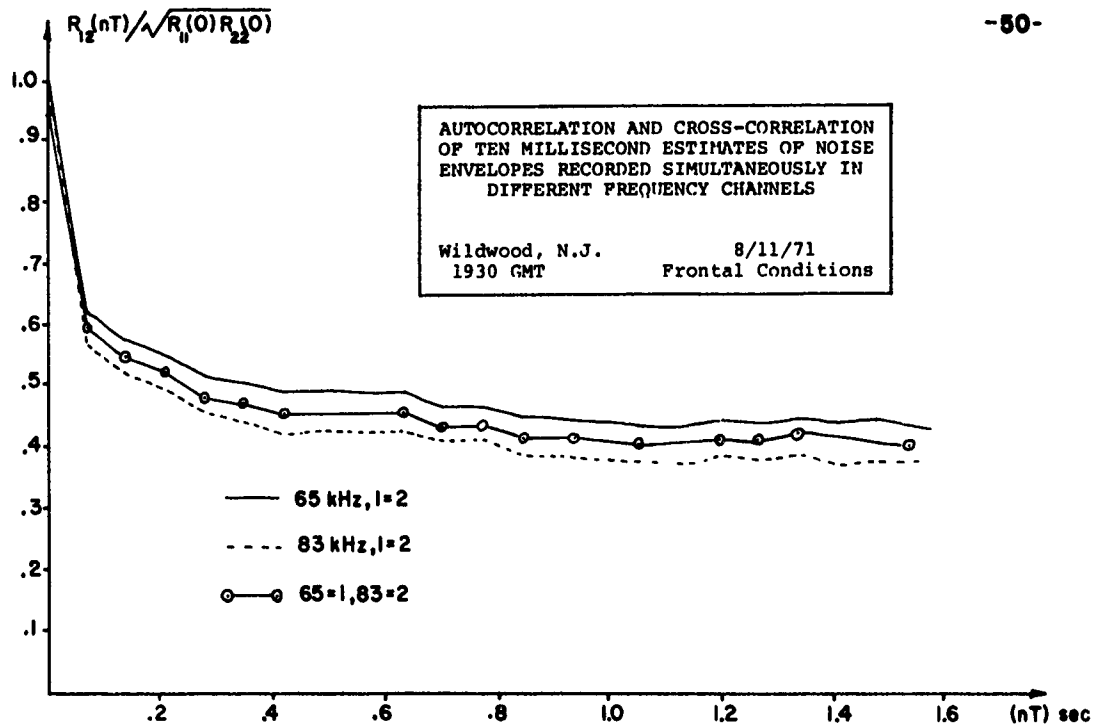


Figure 2-10. Short-Time and Long-Time Autocorrelation of $A(t_i)$

cause $A(t_1)$ to rise well above the level normally caused by the background noise plus the average single discharge rate. The autocorrelation of this 10 msec conditional sample record for tropical conditions is shown in Figure 2-11 where the exponential decay is strongly in evidence. We also note the dramatic difference in magnitude of the decay component between 14 kHz and 65 kHz due to the difference in the lightning burst structure at these frequencies. Due to the effect of the conditioning circuit in these observations we should not draw general conclusions that this large a difference is always present, as can be seen from the sample record in Figure 2-9.

During the quiet noise period when there was only scattered, relatively low energy, discharge activity, there was little significant multiple discharge phenomena. This is shown in the autocorrelation of the 10 msec sample record from this period (Figure 2-12) in which there is little discernible long-time decay. The autocorrelation of the 10 msec sample record for quiet-night conditions (Figure 2-12) does show the long-time decay factor. This was caused by the north-moving warm air soon to cause locally tropical noise conditions, and the fact that propagation distances are greatly extended at night by ionospheric reflections, thus extending the region of geographic noise sensitivity towards the southern warm air mass.

The various cross-frequency-channel correlations shown in Figures 2-10 through 2-12, which reach values of 0.95 in some cases, reinforce the modeling concept of $A(t)$ being frequency independent. We note that cross-correlation is generally better for the 65 kHz-83 kHz pair than for the 65 kHz-14 kHz pair. This is to be expected, due both to the increased frequency separation and to the changing nature of the dominant discharge mechanism at the 14 kHz frequency.

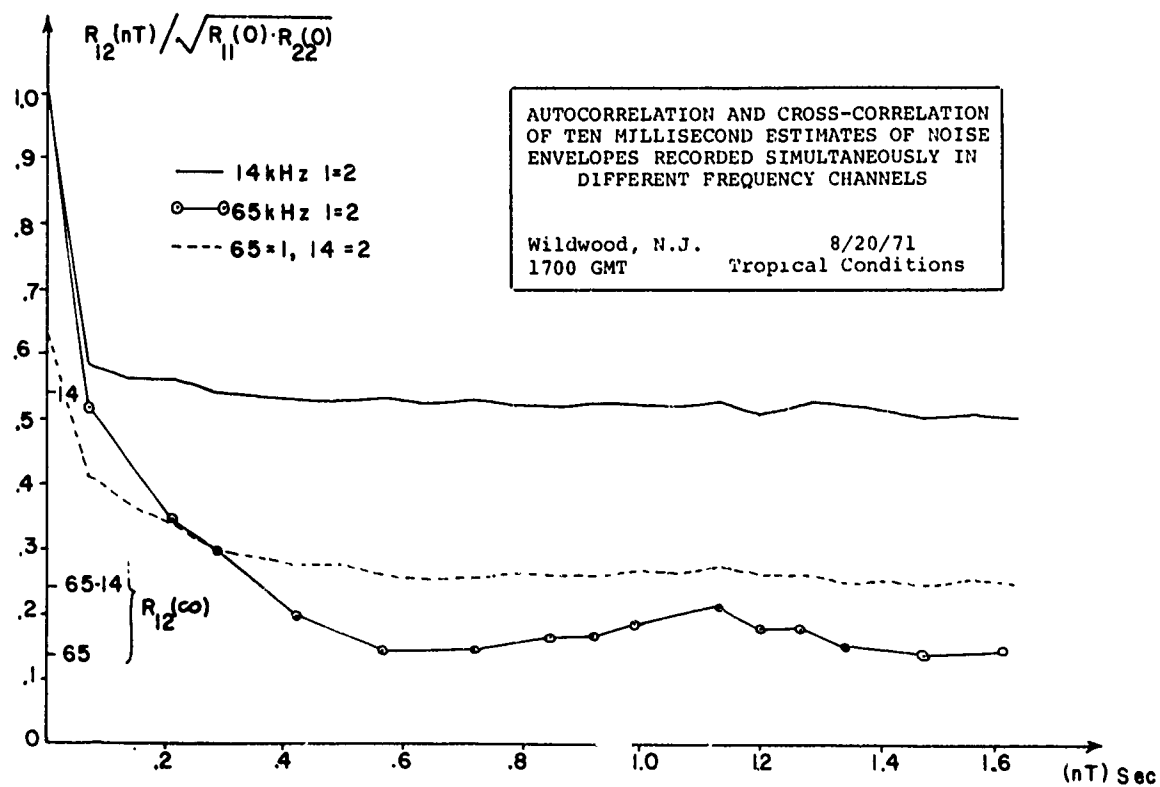
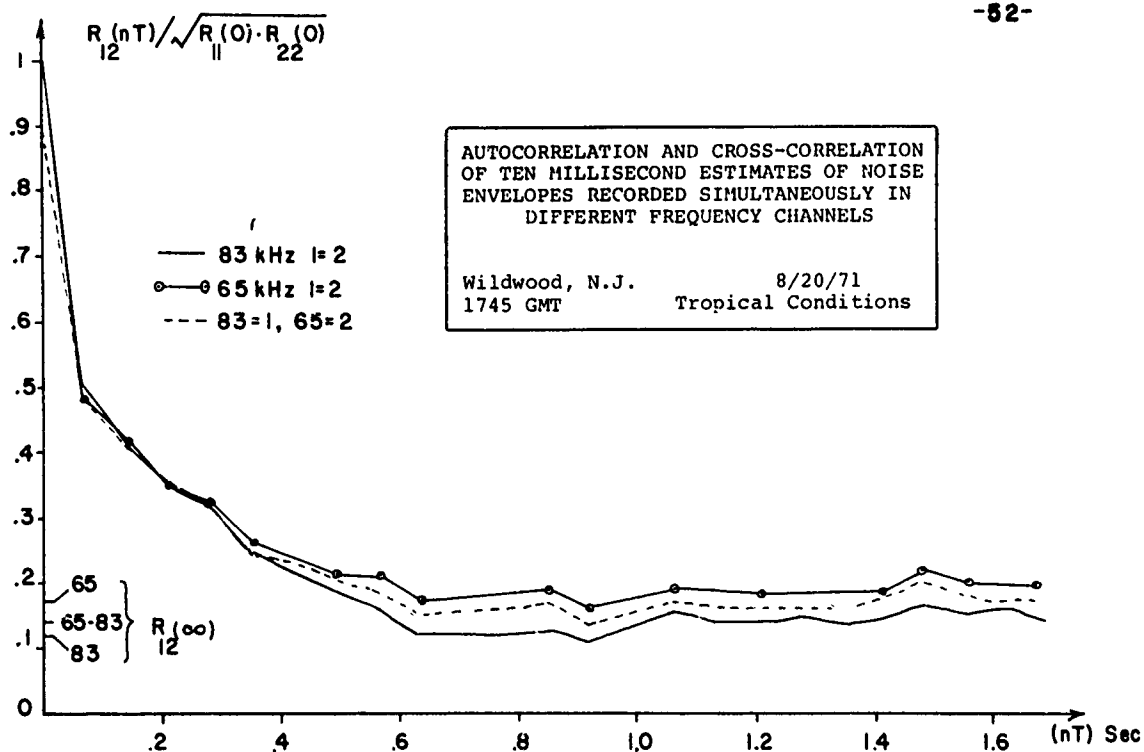


Figure 2-11. Long-Time Correlation Decay Detail

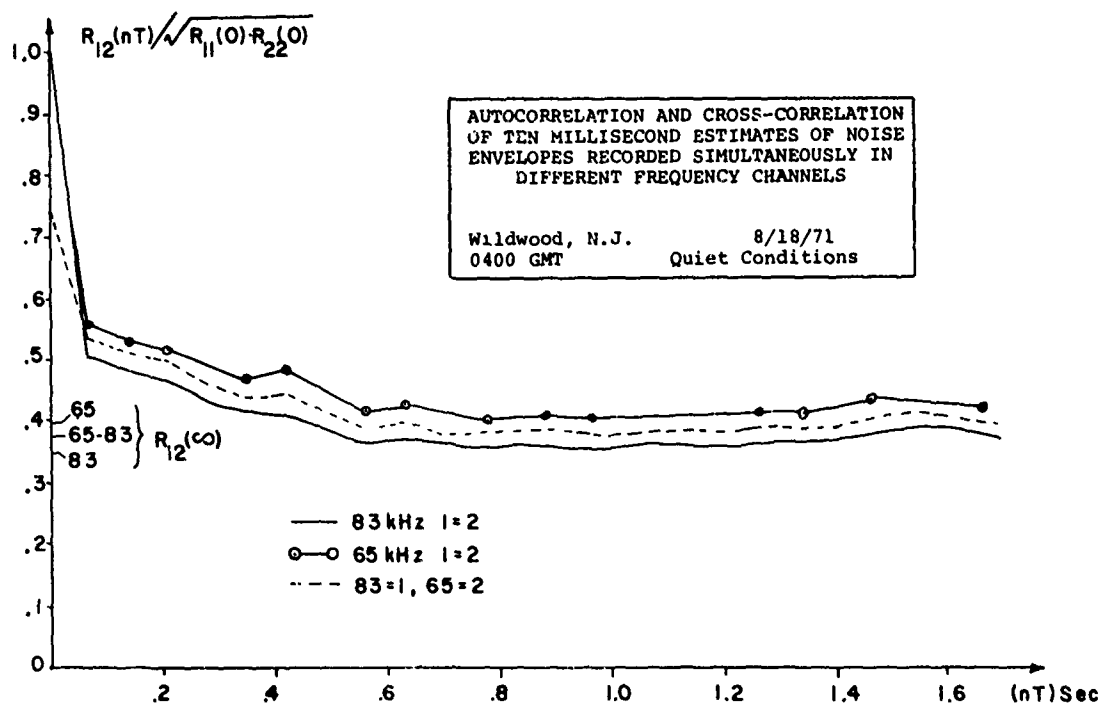
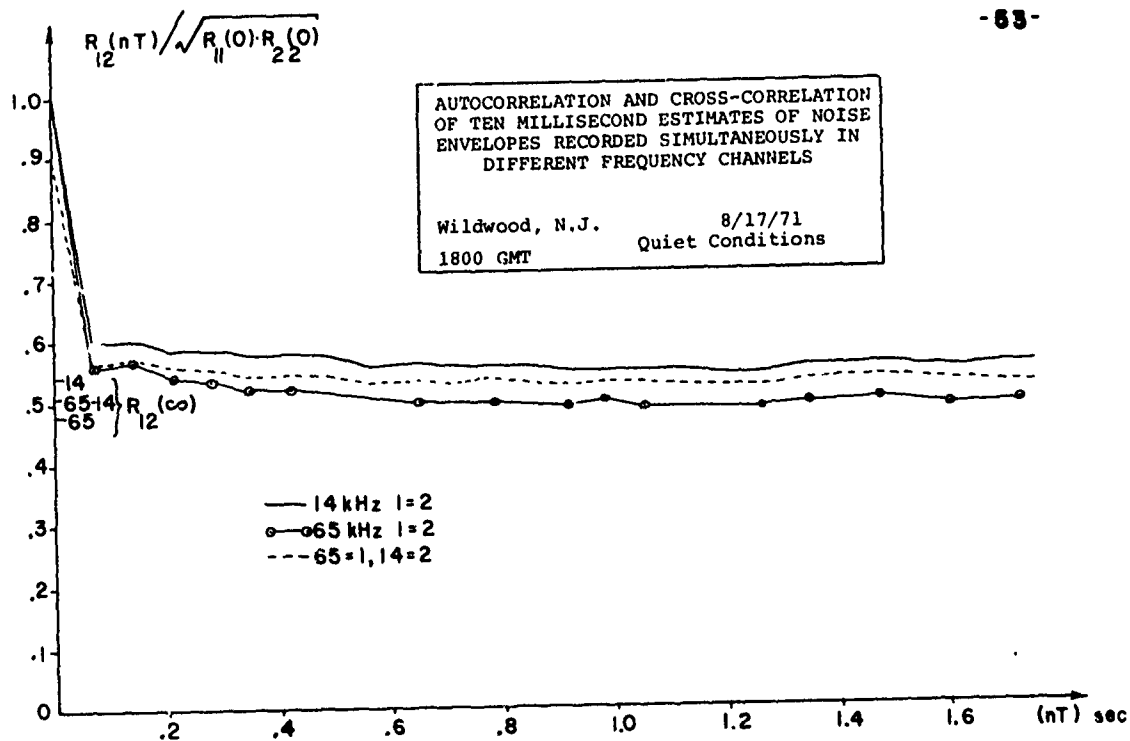


Figure 2-12. Long-Time Correlation for Quiet and Transition Conditions

The principal conclusion that we draw from the correlation analysis of the $A(t_i)$ sample records is that there is not a significant time structure in the time-varying noise power level. By significant, we mean a structure that can be exploited in receiver design to estimate future values of the power level from present observations. We shall find in Chapter 4 that the noise time structure does have a demonstrable effect on receiver performance and that this can be largely compensated for by use of the joint channel information to estimate directly both the correlated and uncorrelated component of $A(t)$, without consideration of a model for $A(t)$ dynamics. Our experimental $A(t_i)$ measurements will be used in the noise model development.

2.6 Summary

In this chapter we have presented a number of statistical measurements of the characteristics of bandlimited VLF and LF atmospheric noise waveforms. These characteristics were measured and interpreted from the point of view of a postulated multiplicative noise model, $y(t) = A(t) \cdot n(t)$. The important results may be summarized as follows.

- a) Atmospheric noise waveforms, especially at LF, exhibit a wide variation in characteristics dependent upon local weather conditions. Since the two physical factors, propagation and noise mechanisms, become more important at frequencies above LF, we expect this variation is similarly more pronounced at higher frequencies.
- b) Measurement of first order joint statistics between a bandlimited rf noise waveform in frequency channel one and an envelope

from frequency channel two show a significant statistical dependence above a threshold value. The model concept that $A(t)$ is independent of frequency attempts to describe these observations.

- c) The received, broadband, atmospheric noise field appears as an uncorrelated random process when observed via narrow-band filters. The average power spectral density of the observed narrow-band noise is proportional to the square of the magnitude of the filter's frequency response.
- d) The hypothetical modulating process, $A(t)$, should be basically uncorrelated beyond 1 msec, with only a small short-time and long-time dynamic damping. This observation is only valid for observation bandwidths of 1 kHz or larger.

In the next chapter we shall develop a noise model based on the multiplicative concept which fits the observed data over the wide range of observed noise/weather conditions.

Chapter 3

AN ATMOSPHERIC NOISE MODEL

In Chapter 1 of this report we gave the motivational background for a multiplicative model for bandlimited atmospheric radio noise. Chapter 2 presented a number of experimental observations of characteristics such a model must possess. In this chapter, we shall develop the specific mathematical form of a multiplicative model. This model will be compared with the observed data and it will be shown that the necessary model parameters can be chosen in a logical manner. Principal weight will be given to the modeling of the first order joint channel statistics since the observations of Chapter 2 show that these are a distinguishing characteristic of atmospheric noise. A method of generating an approximation to the time structure of $A(t)$ will then be given and it will be shown that using the parameters developed for the first order model, acceptable simulation results of the $A(t_1)$ estimates are obtained. Finally, a canonic atmospheric noise generator, suitable for computer implementation using uniform and gaussian random number generators will be given. This is accompanied by a table specifying values of the model parameters which describe the range of experimental data reported in Chapter 2.

3.1 Hall's Noise Model

Hall¹⁸ suggested the multiplicative noise model $y(t) = A(t) n(t)$ as a description of a bandlimited atmospheric noise waveform in a single-frequency channel. Hall proposed that the lowpass random process was generated by the inverse of a chi process, that is,

$$A(t) = \left[\sum_{i=1}^m b_i^2(t) \right]^{-1/2}, \quad (3.1)$$

where the $b_i(t)$ are statistically independent gaussian ($N(0, \sigma)$) lowpass processes. The first order pdf of $A(t)$, the inverse of a $\chi(m, \sigma)$ random variable, is

$$p_A(A) = \frac{(m/2)^{m/2}}{\sigma^m \Gamma\left(\frac{m}{2}\right) |A|^{m+1}} \exp\left[-\frac{m}{2\sigma^2 A^2}\right], \quad -\infty < A < +\infty. \quad (3.2)$$

From (3.2) and the assumption that $n(t)$ is gaussian ($N(0, \sigma_{nH})$) we can compute the pdf of $y(t)$ as

$$\begin{aligned} p_y(y) &= \int_A p_{y|A}(y, \eta) p_A(\eta) d\eta \\ &= \int_{-\infty}^{+\infty} \frac{1}{\sigma_H \eta \sqrt{2\pi}} \exp\left[-\frac{\xi^2}{2\sigma_{nH}^2 \eta^2}\right] \frac{(m/2)^{m/2}}{\sigma^m \Gamma\left(\frac{m}{2}\right) |\eta|^{m+1}} \exp\left[-\frac{m}{2\sigma^2 \eta^2}\right] d\eta \end{aligned}$$

which yields

$$p_y(y) = \frac{\Gamma\left(\frac{m+1}{2}\right) (m\sigma_{nH}^2)^{m/2}}{\Gamma\left(\frac{m}{2}\right) \sqrt{\pi} \left[y^2 + m\sigma_{nH}^2\right]^{\frac{m+1}{2}}}, \quad -\infty < y < +\infty, \quad 0 < m, \quad (3.3)$$

where we have set the σ parameter of the chi process equal to 1 for convenience since it only appears as a divisor of σ_{nH} . Recalling the measured atmospheric noise pdf's given in Figure 2-1, we see that expression (3.3) has the correct basic shape to fit these; a slope of

zero as $y \rightarrow 0$, a single "break-point" on a log-log plot at $y^2 > m\sigma_{nH}^2$ and a hyperbolic decay beyond that point, appearing as straight line of slope $-(m+1)$ on a log vs log plot.

Expression (3.3) is a valid pdf for any $m > 0$, although Hall generally restricted m to be integer. A best-fit selection of m can be made from the large amplitude region of the data pdf. Hall also suggested that the dynamics of $A(t)$ could be provided by specification of a rational power spectral density for $b_i(t)$. Thus we see that m has a second important role in the degree of freedom allowed to effect the dynamics of $A(t)$.

Hall provides a similar closed form expression for the atmospheric noise envelope, from which he computes the exceedance probability (one minus the cumulative probability) of the envelope to compare with published data, principally that given by Watt.⁷ He concludes that his model provides reasonable fits to these data, with a value of $m = 2$ fitting most data reported for moderate mid-latitude noise conditions at VLF. Hall also computes a level crossing statistic. However, since we have taken a different experimental approach to considering time structure, we shall not deal further with the latter comparisons.

3.2 An Extension of Hall's Model

If we compare the pdf of (3.3) in greater detail with the observed probability densities of Figure 2-1, we see that (3.3) does not have sufficient degrees of freedom to account for the second break point seen in the tail of the quiet noise pdf. The occurrence of this breakpoint is indicative of the noise waveform becoming closer to a gaussian process,

and by implication our model should have this capability of being reduced to a gaussian process. A similar difficulty is encountered when we consider the joint channel first order data (Figures 2-5 and 2-6). The generating mechanism of (3.1) does not appear to provide for the uncorrelated portion of the conditional rf noise standard deviation, if we make our assumption that $A(t)$ is deterministically identical for both channels.

A somewhat less important difficulty is encountered if we attempt to associate a time structure for the $b_i(t)$ as that provided by a linear lowpass filter excited by white gaussian noise. As was seen in Figures 2-10 through 2-12 the modulating process, $A(t)$, must be dominated by an uncorrelated component, but have two second order time correlations. However, as will be seen, m values of 2 or 1 are required to match our observations and these do not provide sufficient freedom in the $A(t)$ generator mechanism of (3.1) to meet these time structure observations of Chapter 2.

The basic difficulty noted in the first order behavior of (3.1) is that the bandlimited atmospheric noise waveform has a distinct period when it is in a nearly gaussian state, the so-called background component we have referred to. Our first attempts to deal with this in terms of $A(t)$ consisted of adding a constant bias term to the dynamic $A(t)$ generator of (3.1). This has the effect of suppressing the dynamic component until it exceeds a threshold, and this idea leads naturally to Kapp's¹⁹ idea of a switched process model. We have adapted this to Hall's model as our proposed model, given as

$$y(t) = n_1(t) + x(t) a(t) n_2(t), \quad (3.4)$$

where $y(t)$ is a bandlimited atmospheric noise waveform. The process $a(t) n_2(t)$ is identical to that given by Hall. We shall refer to it as the "Hall component" and use σ_{nH} for the associated parameter of $n_2(t)$. $x(t)$ is a two-state process, assuming values one or zero with probability p_x and q_x , respectively. The process $n_1(t)$ is a narrow-band gaussian process (first order pdf $N(0, \sigma_G)$) and provides the background gaussian component required of our model. The components $n_1(t)$ and $n_2(t)$ are statistically independent, with power spectral densities proportional to the bandlimiting filter's magnitude response squared. The function of $x(t)$ is to "switch-on" the non-gaussian or Hall noise component, modeling those time periods when the atmospheric noise waveform is in a distinctly non-gaussian state. In addition to providing several more degrees of freedom for first order statistics, we also have available the time structure of $x(t)$, coupled with that of $a(t)$, to model the observations of $A(t)$'s time structure.

The first order pdf of $y(t)$, defined by (3.4), is given by

$$\begin{aligned} p_y(y) &= N(0, \sigma_{nG}) \otimes [q\delta(\eta) + p_x p_{yH}(\eta)] \\ &= qN(0, \sigma_{nG}) + p_x N(0, \sigma_{nG}) \otimes p_{yH}(\eta), \end{aligned} \quad (3.5)$$

where \otimes denotes convolution, $\delta(\cdot)$ the Dirac delta function, and $p_{yH}(\eta)$ is the Hall pdf, (3.3). The characteristic function (cf) of $p_y(y)$ can be expressed in closed form, but we have not been able to obtain its inverse transform. We note that the background process, $n_1(t)$, is quite small with respect to the large noise amplitudes provided by the Hall component, hence the gaussian pdf appears as an impulse scanning function at

these large values of the argument y . Thus our model preserves the hyperbolic tail ($\lim_{y \rightarrow \infty} p_y(y) \propto 1/y^{m+1}$) of the Hall component to match the observed large amplitude behavior of atmospheric noise. In most practical cases, the resulting $p_y(y)$ can be approximated as a sum of a gaussian and Hall pdf; however, we have used numerical techniques to evaluate $p_y(y)$ in section 3.6.2 below.

3.3 Noise Envelope

To develop an approximation to the envelope pdf for a bandlimited noise waveform given by (3.4), we begin with the definition of the joint envelope and phase pdf²⁹ as

$$p_{v,\phi}(v,\phi) = v p_{y,\tilde{y}}(v \cos \phi, v \sin \phi), \quad v^2 = y^2 + \tilde{y}^2, \quad (3.6)$$

$$\phi = \tan^{-1} \tilde{y}/y, \quad \tilde{y} \triangleq \text{Hilbert Transform}(y).$$

In our case

$$y = n_1 + x a n_2, \quad \tilde{y} = \tilde{n}_1 + x a \tilde{n}_2,$$

where for $n_{1,2}$ gaussian narrow-band, $\tilde{n}_{1,2}$ are also gaussian narrow-band and statistically independent. The quantity $x a$ need not be hatted if we assume that $x a$ has no frequency overlap with n_2 , that is, it is slowly varying with respect to the band-center frequency. Thus the envelope pdf is formally given as

$$\begin{aligned}
 p_{v,\phi}(v,\phi) &= v \int_a \int_x p_{y,y}(v \cos \phi, v \sin \phi, a, x) da dx \\
 &= v \int_a \int_x p_{y,y|a,x}(\dots) \cdot p_a(\eta) \cdot p_x(\xi) d\eta d\xi \\
 &= v q_x \int_a p_{N(0,\sigma_G)}(v \cos \phi) \cdot p_{N(0,\sigma_G)}(v \sin \phi) \cdot p_a(\eta) d\eta \\
 &\quad + v p_x \int_a \int_a p_{N(0,\sigma_G)}(v \cos \phi - a) p_{N(0,a\sigma_{nH})}(a\alpha) d\alpha \\
 &\quad \cdot \int_\beta p_{N(0,\sigma_G)}(v \sin \phi - \beta) p_{N(0,a\sigma_{nH})}(a\beta) d\beta p_a(a) da \\
 &= \frac{q_x v}{2\pi} R(\sigma_G) + v p_x \int_a p_N(v \cos \phi - a) \cdot \int_\beta p_N(v \sin \phi - \beta) \\
 &\quad \cdot \int_a p_N(a\alpha) p_N(a\beta) p_a(a) da d\alpha d\beta.
 \end{aligned} \tag{3.7}$$

The last integral with respect to "a" is similar in form to that leading to (3.3) and is recognized as Hall's expression for the envelope pdf of his noise model. Expression (3.7) suggests a form of the first order envelope pdf (with phase random 0-2 π) similar to that given for the band-limited noise by (3.5), if we identify the second term as a convolution of a Rayleigh pdf with the Hall envelope pdf. The second term of (3.7) does not reduce to this convolution; however, we shall use this form as an approximation to the noise envelope. This approximation then yields an envelope and associated first order pdf;

$$v(t) = v_1(t) + x(t) a(t) v_2(t), \tag{3.8}$$

where $v_1(t)$ is Rayleigh ($R(\sigma_G)$) and $v_2(t)$ is Rayleigh ($R(\sigma_{vH})$), the pdf of

$a(t) v_2(t) = v_H(t)$ is given by

$$\begin{aligned}
 p_{v_H}(v) &= \int_a p_{v/a}(v, \eta) p_a(\eta) d\eta \\
 &= \int_a \frac{v}{\eta^2 \sigma_{v_H}^2} \exp\left[\frac{-v^2}{2\eta^2 \sigma_{v_H}^2}\right] \frac{(m/2)^{m/2}}{\Gamma(m/2) |\eta|^{m+1}} \exp\left[\frac{-m}{2\eta^2}\right] d\eta \\
 &= \frac{2v(m/2)^{m/2}}{\sigma_{v_H}^2 \Gamma(m/2)} \int_0^\infty \frac{1}{\eta^{m+3}} \exp\left[-\frac{v^2 + m\sigma_{v_H}^2}{2\sigma_{v_H}^2} \cdot \frac{1}{\eta^2}\right] d\eta \\
 p_{v_H}(v) &= \frac{v(m)^{\frac{m+2}{2}} (\sigma_{v_H})^m}{(v^2 + m\sigma_{v_H}^2)^{\frac{m+2}{2}}}, \quad 0 \leq v < \infty, \quad (3.9)
 \end{aligned}$$

and the pdf of $v(t)$ is

$$p_v(v) = q_x R(\sigma_{v_G}) + p_x R(\sigma_{v_G}) \otimes p_{v_H}(\eta). \quad (3.10)$$

We note that this approximate model and resulting pdf for the envelope provides the correct small amplitude behavior ($\lim_{v \rightarrow 0} p_v(v) \propto v$) and a large amplitude behavior following a hyperbolic tail ($\lim_{v \rightarrow \infty} p_v(v) \propto \frac{1}{v^{m+1}}$).

3.4 Joint Channel Model

We can now combine the model for a bandlimited atmospheric noise waveform, observed in frequency channel f1, the approximate envelope model for frequency channel f2, and our assumption that $a(t)$ is identical in both models to determine joint channel characteristics. When $x(t) = 0$, or the Hall noise component is very small ($a(t)$ small) the background

gaussian noise component dominates both envelope and rf noise densities and the joint channel density is simply the product of the two since they are statistically independent. When $x(t) = 1$ and the Hall component is dominant, we can proceed exactly as in developing the envelope and rf Hall noise densities ((3.3) and (3.9)) to develop the joint channel pdf.

Thus

$$\begin{aligned}
 p_{y,v}(y,v) &\approx p_{yH,vH}(y,v) = \int_a p_{y,v|a}(y,v,\eta) p_a(\eta) d\eta \\
 &= \int_a p_{y|a}(y,\eta) p_{v|a}(v,\eta) p_a(\eta) d\eta \\
 &= \int_0^\infty \frac{2}{\eta \sigma_{nH}^2 \sqrt{2\pi}} \exp\left[\frac{-y^2}{2\sigma_{nH}^2 \eta^2}\right] \cdot \frac{v}{\eta^2 \sigma_{vH}^2} \exp\left[\frac{-v^2}{2\sigma_{vH}^2 \eta^2}\right] \\
 &\quad \cdot \frac{2(m/2)^{m/2}}{\Gamma\left(\frac{m}{2}\right) |\eta|^{m+1}} \exp\left[\frac{-m}{2\eta^2}\right] d\eta \\
 &= \frac{\left(\frac{m}{2}\right)^{m/2} \Gamma\left(\frac{m+1}{2}\right) 2^{\frac{m+1}{2}} v}{\sigma_{nH}^2 \sigma_{vH}^2 \Gamma\left(\frac{m}{2}\right) \sqrt{2\pi} \left[\left(\frac{y}{\sigma_{nH}}\right)^2 + \left(\frac{v}{\sigma_{vH}}\right)^2 + m \right]^{\frac{m+3}{2}}}, \\
 &\quad -\infty \leq y < +\infty, \quad 0 \leq v < +\infty. \quad (3.11)
 \end{aligned}$$

In a similar manner, the joint pdf for the Hall component of the envelope in two disjoint frequency channels can be computed as

$$p_{v_{Hf_1}, v_{Hf_2}}(v_1; v_2) = \frac{(m)^{\frac{m+2}{2}} 2\left(\frac{m}{2} + 1\right) v_1 v_2}{\sigma_{vH_1}^2 \sigma_{vH_2}^2 \left[\frac{v_1^2}{\sigma_{vH_1}^2} + \frac{v_2^2}{\sigma_{vH_2}^2} + m \right]^{\frac{m+4}{2}}} \quad (3.12)$$

From the joint pdf's and the single-channel pdf's we can determine the conditional pdf of either variable. For example, the conditional pdf of the rf noise, y , given a pilot channel envelope value v_o , is

$$p_{y|v_o}(y) = p_{y, v_o}(y, v_o) \cdot \frac{1}{p_{v_o}(v_o)} \\ \propto \frac{1}{\left[\frac{y^2}{\sigma_{nH}^2} + \frac{v_o^2}{\sigma_{vH}^2} + m \right]^{\frac{m+3}{2}}} \quad (3.13)$$

Comparing (3.13) to the unconditional pdf of y , (3.3) and the observed data in Figures 2-5 and 2-6 we see that it has the correct form for small values and large values of y , and that the conditional pdf tail decreases by a power of two faster than the unconditional pdf. This behavior will be considered in more detail in section 3.6.3 below.

3.5 First Order Model Statistics

3.5.1 Unconditional Moments

Inspection of the limiting large amplitude behavior of the Hall component of the noise pdf's ((3.3 and (3.9)), given by

$$\lim_{y \rightarrow \infty} p_y(y) \approx \lim_{y \rightarrow \infty} p_{yH}(y) \propto \frac{1}{y^{m+1}}, \quad (3.14a)$$

$$\lim_{v \rightarrow \infty} p_v(v) \approx \lim_{v \rightarrow \infty} p_{vH}(v) \propto \frac{1}{v^{m+1}}, \quad (3.14b)$$

shows that both have unbounded first and second moments for $m = 1$ and unbounded second moments for $m = 2$. These are the values of m required to fit all of our observed data and we are thus faced with a situation of attempting to model a physical phenomenon with a model that has an infinite power level. Hall suggested this difficulty be overcome by truncating the range of the inverse chi process, $a(t)$. We shall simply truncate the complete noise density at a value of y_{\max} or v_{\max} which corresponds to the upper limit of our observed noise density. This truncation was the most convenient in our numerical comparisons of the model to the observed noise characteristics. In the case of realizing the canonic atmospheric noise generator (to be given in section 3.8) in a Monte Carlo computer simulation it is probably more convenient to truncate $a(t)$. Since $n_2(t)$ is gaussian, the resulting distribution will decay rapidly beyond such an $a(t)$ truncation point and hence it is probably not of great practical significance which method is employed since, as we shall find, practical signal processing structures are quite insensitive to the exact probability of the large amplitude noise components.

Distribution moments, the second moment or power level in particular, are well ingrained in engineering thinking due to their role in linear systems and gaussian noise. However, for non-gaussian noise, they are only two parameters of a theoretically infinite set required to completely characterize an arbitrary distribution. In the case of non-

gaussian atmospheric noise, they are only moderately informative, as when the ratio of rms to mean value of the envelope, the so-called V_D parameter,^{14, 17, 30} is used to characterize the degree of non-gaussianity of the pdf. We shall find in Chapter 4 that a simple nonlinear system will perform upwards of 17 dB better in frontal type of noise as compared with gaussian noise of equal power level. Improved signal processing structures of this type are sensitive to the nature of the noise pdf in the low-to-middle amplitude region and almost insensitive to the large amplitude portion, while the latter in many cases can dominate the second moment or power level. For these reasons, as well as the practical one that measurement of the noise power level with analog instruments is a very difficult proposition due to the dynamic range, we have considered first and second moments of the noise model only incidentally, after the model parameters have been selected by other criteria.

Values of the first and second moments of the rf and envelope noise model pdf's are given below for the cases of interest.

a) General

$$\overline{|y|} = \overline{|n_1 + x n_2|} \approx \overline{|n_1|} + x \overline{|y_H|}$$

$$\overline{v} = \overline{v_1 + x v_2} = \overline{v_1} + x \overline{v_H}$$

$$\overline{|y|^2} \approx \overline{n_1^2} + 2x \overline{|y_H|} \overline{|n_1|} + x^2 \overline{y_H^2}$$

$$\overline{v^2} = \overline{v_1^2} + 2\overline{v_1} \overline{v_H} x + x^2 \overline{v_H^2}$$

Using Gaussian/Rayleigh and Hall component pdf's with upper integration

limits of v_{\max} and y_{\max} , the moments of (a) above yield:

b) $m = 1$,

$$\overline{|y|} = .797 \sigma_{nG} + \frac{2p\sigma_{nH}}{\pi} \ln [y_{\max}/\sigma_{nH}] \quad (3.15)$$

$$\overline{v} = \frac{\pi}{2} \sigma_{vG} + p_{\star} \sigma_{vH} \ln \left[\frac{2v_{\max}}{\sigma_{vH}} - 1 \right] \quad (3.16)$$

$$\overline{|y|^2} \approx \sigma_{nG}^2 + p_{\star} \sigma_{nH} \sigma_{nG} \ln \left[\frac{y_{\max}}{\sigma_{nH}} \right] + \frac{2p\sigma_{nH}y_{\max}}{\pi} \quad (3.17)$$

$$\begin{aligned} \overline{v^2} = & 2\sigma_{vG}^2 + \sqrt{2\pi} \sigma_{vG} \sigma_{vH} \left[\ln \left[\frac{2v_{\max}}{\sigma_{vH}} \right] - 1 \right] p_{\star} \\ & + \sigma_{vH}^2 \left[\frac{v_{\max}}{\sigma_{vH}} - 2 \right] p_{\star} \end{aligned} \quad (3.18)$$

c) $m = 2$,

$$\overline{|y|} = .797 \sigma_{nG} + p_{\star} \left[\sqrt{2} \sigma_{nH} - \frac{2\sigma_{nH}^2}{y_{\max}} \right] \quad (3.19)$$

$$\overline{v} = \frac{\pi}{2} \sigma_{vG} + p_{\star} \frac{\pi}{\sqrt{2}} \sigma_{vH} \quad (3.20)$$

$$\overline{|y|^2} = \sigma_{nG}^2 + (2.25) p_{\star} \sigma_{nG} \sigma_{nH} + p_{\star}^2 \sigma_{nH}^2 \left[1 + \ln \sqrt{2} \frac{y_{\max}}{\sigma_{nH}} \right] \quad (3.21)$$

$$\overline{v^2} = 2\sigma_{vG}^2 + 2p_{\star} \sqrt{\frac{\pi^3}{4}} \sigma_{vG} \sigma_{vH} + p_{\star}^2 4\sigma_{vH}^2 \ln \left[\frac{v_{\max}}{\sigma_{vH}} \right] - 3.39 \sigma_{vH}^2 p_{\star} \quad (3.22)$$

3.5.2 Conditional Moments

The second moment of the rf channel noise, conditioned by the value of the pilot channel envelope, can be computed from the assumption that $x(t) a(t)$ is common to both channels, and the pdf of $a(t)$, as follows:

$$\begin{aligned} \int_y \eta^2 p_{y|v, x=0}(\eta, v_o) d\eta &= \int_y \eta^2 p_{y_1}(\eta) p_v(v_o) \frac{1}{p_y(v_o)} d\eta \\ &= \int_y \eta^2 p_{N(0, \sigma_{nG}^2)}(\eta) d\eta = \sigma_{nG}^2, \end{aligned}$$

the unconditional variance of the background component of the rf noise.

b) With $x(t) = 1$, the conditional variance of the dominant Hall component is given by

$$\begin{aligned} \int_y \eta^2 p_{yH|vH, x=0}(\eta, v_o) d\eta &= \frac{1}{p_{vH}(v_o)} \int_y \eta^2 p_{yH, vH}(\eta, v_o) d\eta \\ &= \frac{1}{p_{vH}(v_o)} \int_y \eta^2 \int_a p_{yH, vH|a}(\eta, v_o, \xi) \\ &\quad \cdot p_a(\xi) d\xi d\eta \\ &= \frac{1}{p_{vH}(v_o)} \int_y \eta^2 \int_a p_{yH|a}(\eta, \xi) \\ &\quad \cdot p_{vH|a}(v_o, \xi) p_a(\xi) d\xi d\eta. \end{aligned}$$

Interchanging the order of integration and substitution of a gaussian pdf for $p_{yH|a}(\eta, \xi)$ yields

$$\begin{aligned}
 \int_y \eta^2 p_{yH|vH, x=0}(\eta, v_o) d\eta &= \frac{1}{p_{vH}(v_o)} \int_a p_{vH|a}(v_o, \xi) p_a(\xi) \\
 &\quad \cdot \int_y \eta^2 p_{yH|a}(\eta, \xi) d\eta d\xi \\
 &= \frac{1}{p_{vH}(v_o)} \int_a p_{vH|a}(v_o, \xi) \xi^2 \sigma_{nH}^2 p_a(\xi) d\xi.
 \end{aligned}$$

Substitution of a Rayleigh pdf for $p_{vH|a}(v_o, \xi)$ and the $a(t)$ pdf (3.9) yields

$$\begin{aligned}
 \int \eta^2 p_{yH|vH, x=0}(\eta, v_o) d\eta &= \frac{\left(\frac{m}{2}\right)^{m/2} \sigma_{nH}^2 v_o^2}{p_{vH}(v_o) \sigma_{vH}^2 \Gamma\left(\frac{m}{2}\right)} \int_0^\infty \frac{2}{\xi^{m+1}} \\
 &\quad \cdot \exp - \frac{(v_o^2 + m\sigma_{vH}^2)}{2\xi^2 \sigma_{vH}^2} d\xi \\
 &= \frac{1}{m} \frac{\sigma_{nH}^2}{\sigma_{vH}^2} \left[v_o^2 + m\sigma_{vH}^2 \right]. \tag{3.23}
 \end{aligned}$$

These two results are conditioned on both the value of the pilot channel envelope, v_o , and the state of $x(t)$, whereas the data, such as Figure 2-7, is conditioned only on v_o . Thus, these results are valid for small and large amplitudes of the envelope, where one may infer, in a Bayesian sense, the state of $x(t)$ being 0 or 1, respectively. These results are sufficient to describe all but a small transition region of the conditional rf noise variance.

Using the approximation for the noise envelope (3.8) and the

Rayleigh and Hall component pdf's we obtain similar results for the conditional second moment of the joint envelope-pilot channel envelope;

a) with $x(t) = 0$

$$\int_{v_1} \eta^2 p_{v_1} | v_2, x=0(\eta, v_2) d\eta = 2\sigma_{vG}^2, \quad (3.24)$$

b) with $x(t) = 1,$

$$\int_{v_1} \eta^2 p_{v_1 H} | v_2 H, x=0(\eta, v_2) d\eta = \frac{2\sigma_{v_1 H}^2}{m\sigma_{v_2 H}^2} \left[v_2^2 + m\sigma_{v_2 H}^2 \right]. \quad (3.25)$$

We shall also compare the ratio of mean to variance of the conditional $|rf|$ channel pdf for the model and the data, as a measure of the non-gaussian character of the conditional rf distribution. This is computed from the joint $y-v$ pdf (3.12), with $m = 1$, as follows. The use of the upper limit of integration is not required here because the moments are unbounded, rather it includes the effect of the maximum range of the observations which affects the ratio of interest at large values of the envelope.

$$2 \int_0^{y_{\max}} \eta^2 p_{yH, vH}(\eta, v_o) \cdot \frac{1}{p_{vH}(v_o)} d\eta$$

$$= \frac{\left[(v_o/\sigma_{vH})^2 + 1 \right]^{3/2}}{\pi} \cdot \frac{\left[\tan^{-1} \left[\frac{y_{\max}}{\sigma_{nH} \sqrt{v_o^2/\sigma_{vH}^2 + 1}} \right] \right]}{\left[v_o^2/\sigma_{vH}^2 + 1 \right]^{1/2}}$$

$$- \frac{y_{\max}}{\sigma_{nH} \left[y_{\max}^2 / \sigma_{nH}^2 + v_o^2 / \sigma_{vH}^2 + 1 \right]} \quad (3.26)$$

$$\begin{aligned} & 2 \int_0^{y_{\max}} \eta p_{yH, vH}(\eta, v_o) \cdot \frac{1}{p_{vH}(v_o)} d\eta \\ &= \frac{2}{\pi} \left[\frac{v_o^2}{\sigma_{vH}^2} + 1 \right]^{3/2} \cdot \left[\frac{1}{\left[v_o^2 / \sigma_{vH}^2 + 1 \right]} - \frac{1}{\left[y_{\max}^2 / \sigma_{nH}^2 + v_o^2 / \sigma_{vH}^2 + 1 \right]} \right] \end{aligned} \quad (3.27)$$

3.6 Comparison of Joint Channel Model with Data

3.6.1 General Parametric Dependence

We have used the unconditional probability densities of the rf noise from frequency channel 1 and the envelope from frequency channel 2, plus the conditional standard deviation of the rf noise, as the data base to compare our first order model with observed data. The joint channel model, with parameters, is given by

$$\begin{array}{c} \sigma_{nG} \qquad \qquad \sigma_{nH} \\ y_{f1} = n_1(t) + x(t) a(t) n_2(t) \\ \qquad \qquad \qquad | \qquad | \\ \qquad \qquad \qquad p_x \quad m \\ \qquad \qquad \qquad | \qquad | \\ v_{f2} = v_1(t) + x(t) a(t) v_2(t). \\ \qquad \qquad \qquad | \qquad | \\ \sigma_{vG} \qquad \qquad \sigma_{vH} \end{array} \quad (3.28)$$

The parameter m determines the large amplitude behavior of the rf and envelope pdf's (3.14a, b) and must satisfy $m > 0$. We have restricted m to be an integer which provides the simple generating mechanism for the canonic atmospheric noise generator to be given in section 3.8. The parameter m is thus estimated from the slope of the observed density tail on a log-log plot (see section 3.1).

We found in section 3.5.2 that the conditional rf noise variance is given by the variance of the background gaussian component, $n_1 \leftarrow \sigma_{nG}^2$, for small values of the conditioning envelope. This variance is then the square of the horizontal portion of the conditional standard deviation plot as seen in Figure 2.7. The parameter p_x , the probability that the two state process $x(t)$ is in state 1 ($x(t) = 1$) can be estimated from a simultaneous plot of the conditional rf noise standard deviation versus the conditioning envelope, and the cumulative probability of the envelope. The point where the conditional standard deviation begins to exhibit a dependence upon the conditioning envelope is the envelope value where $x(t)$ must be in state 1 to introduce the dependence via $a(t)$. The intersection of this envelope value with the cumulative envelope probability is then related to p_x as

$$p_x = 1 - P_{v_0}(v \leq v_0).$$

The remaining three parameters, $\sigma_{vG}, \sigma_{nH}, \sigma_{vH}$, must then be chosen to simultaneously provide a best fit to the two unconditional probability densities and the predicted relationship between the conditional standard deviation and the conditioning envelope given by (3.23).

3.6.2 Comparison Results

The general algorithm used to compare the model with the observed joint channel data was the following:

- a) Estimate the parameters m , σ_{nG} , and p_x from the information given above.
- b) Utilize the computer to numerically evaluate the two pdf convolutions (given by (3.5) and (3.10)) as a function of these three parameters plus the three remaining parameters to achieve the best simultaneous fit to the three data plots. This was an iterative procedure in which we subjectively evaluated the data fit, giving principal weight to the fit of the probability densities through the middle region where the variance of the experimental estimate of the density was minimum (see Appendix B).

The results of our comparison and the required parameters are shown in Figures 3-1 through 3-4 for quiet through frontal noise conditions.* We see in Figure 3-1 in the upper right plot the selection of the value of p_x at the break point in the conditional standard deviation curve and the corresponding observation that the noise is in a non-gaussian state for only 10% of the observed sample record. In the lower right plot of the unconditional envelope we note a major deviation of the observed data from the predicted small signal behavior. This is not a characteristic of the noise envelope but is caused by an instrumentation error, a dc offset in the lowpass filter used to recover the envelope from the

*The variables RF and E are data variables corresponding to model variables y and v , respectively. Also, $p_T \equiv p_x$ and $\sigma_{eH} \equiv \sigma_{vH}$.

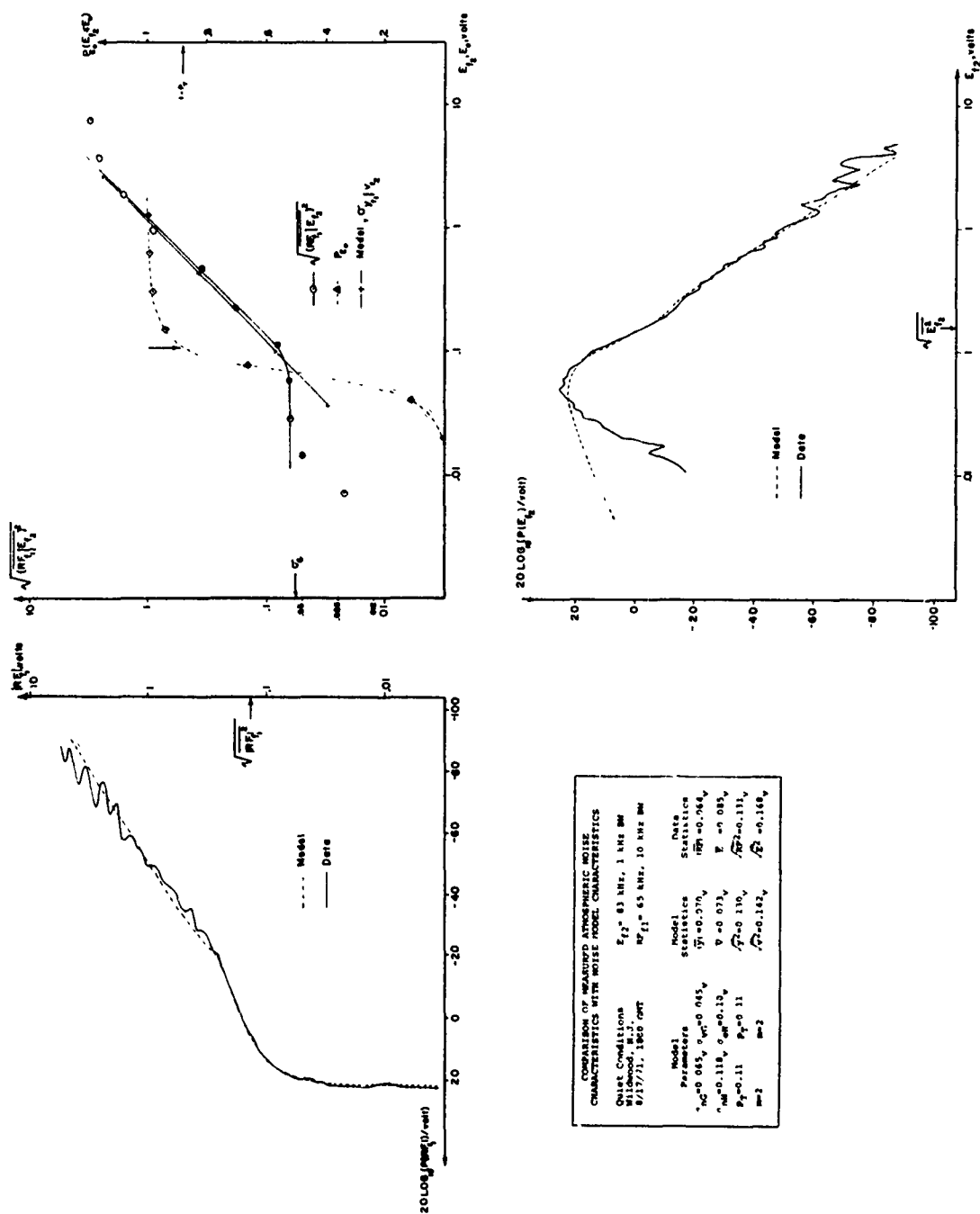


Figure 3-1. Comparison of Model to Quiet Noise Observations



Figure 3-3. Comparison of Model to Tropical Noise Observations

wideband linear rectifier. Since this error does not appear to seriously affect the large amplitude behavior of the envelope, it was not considered to be a fatal flaw in the data. Both the rf noise and envelope noise model data comparisons show that the model does have sufficient flexibility to reproduce the second large amplitude breakpoint which, as noted in Chapter 2, is caused by the low probability-of-occurrence, non-gaussian excursions of the noise waveform. Thus the model parameters (specifically p_x , the probability that $x(t)$ is in state 1, adding the non-gaussian Hall noise component) can be chosen to provide a smooth transition of the model to a purely gaussian noise waveform. On the conditional standard deviation plot, the line labeled "Model, $\sigma_{y_{f1} | v_{f2}}$ " is given by (3.23), assuming $v_o^2 > m\sigma_{nH}^2$. The breakpoint predicted by this relation (i.e., where that assumption does not hold) occurs approximately at the actual data breakpoint, but this is not true for the other data comparisons so that only the linear portion of the curve, dependent upon m, σ_{nH} and σ_{vH} is shown. Finally, the moment statistics of the model and data are given in the title block. These were computed from the relation given in section 3.5.1, and we see that the model agrees quite closely with the data, as we would expect from the generally good fit of the model pdf to the data pd.

The data used in the comparison of Figure 3-2 was recorded during a transition noise condition. The increase in propagation range of the lightning discharge radiation at night provided a much higher geographic density of lightning sources which is reflected in the p_x value of 0.5 and the disappearance of the second large amplitude breakpoint in the pdf tails. The m value of 2 actually fits the tails better here than in the

quiet conditions. This again is reflective of propagation effects; the fewer discharges affecting the quiet data were local and hence had a tendency to larger excursions which implies a shallower slope or lower value of m . For the quiet-night data, on the other hand, the greater distance and the fact that more discharges tended to add together produced the effect of a steeper slope in the tail. Again we note the generally excellent match of the model with the composite data plot, and the individual channel moments given in the title block.

The remaining two figures, Figures 3-3 and 3-4, show progressively more non-gaussian noise conditions as reflected in the increasing value of p_x and the use of an m value of 1. Both of these data records were made during local morning or afternoon and hence tend to reflect dominance of individual excursions ($x(t) = 1$) by strong local discharge radiation. Multiple discharges are also prominent during these conditions as seen in the discussion of section 2.5.2. We note that the modeling of the joint channel dependence continues to provide good results in the conditional standard deviation plots. The unconditional envelope model of Figure 3-4 is probably the worst data match that we obtained with all of our records; this same behavior was found in both of the other two 65 kHz records made during those conditions. The dc offset in the lowpass filter contributed to this error, and it is also probable that the sample record was not long enough (100,000 samples) to collect a representative sample of the long multiple discharges that dominate the frontal noise conditions. This latter effect would not be so predominant in the rf noise record due to the randomizing nature of the phase (or equivalently $n_2(t)$) in this data, hence the better match to the pdf seen in the

upper left plot.

It can be seen that the observed noise conditions span, very nearly, the full range of model parameter values. The frontal conditions, with $p_x = 0.9$ and $m = 1$ represent the largest deviation from gaussianity of which the model is capable. The quiet conditions, with $p_x = 0.11$ and $m = 2$, approach gaussian noise conditions and one might assume that even lower values of p_x and/or larger values of m would be found during temperate latitude winter weather.

A comparison of the noise model with data recorded at 14 kHz is shown in Figure 3-5 for three noise conditions. In the discussion of section 3.6.1 we saw the intimate dependence of the choice of the p_x and σ_{nG} parameters with the joint channel dependency, which was not available for these VLF observations. Thus the parameter estimation procedure was considerably more difficult, and more important, the results do not provide the same degree of uniqueness in parameter values as that for the joint channel data. For example, it is difficult to separate the effect of σ_{nH} and p_x using only the single channel data since these two parameters enter in a product relation for large amplitudes, as seen from the pdf expression for the Hall noise component (3.3) which is scaled by p_x in the pdf convolution of (3.5). In a more general context, if we considered that the observed probability densities were three curves to be represented mathematically, there are four parameters involved, the first breakpoint, the following slope, the second breakpoint, and the final slope (this assumes that the selected mathematical expression provides the correct small signal behavior and that pdf normalization, $\int_{-\infty}^{+\infty} p_y(\eta) d\eta = 1$, provides an overall scale factor). Since

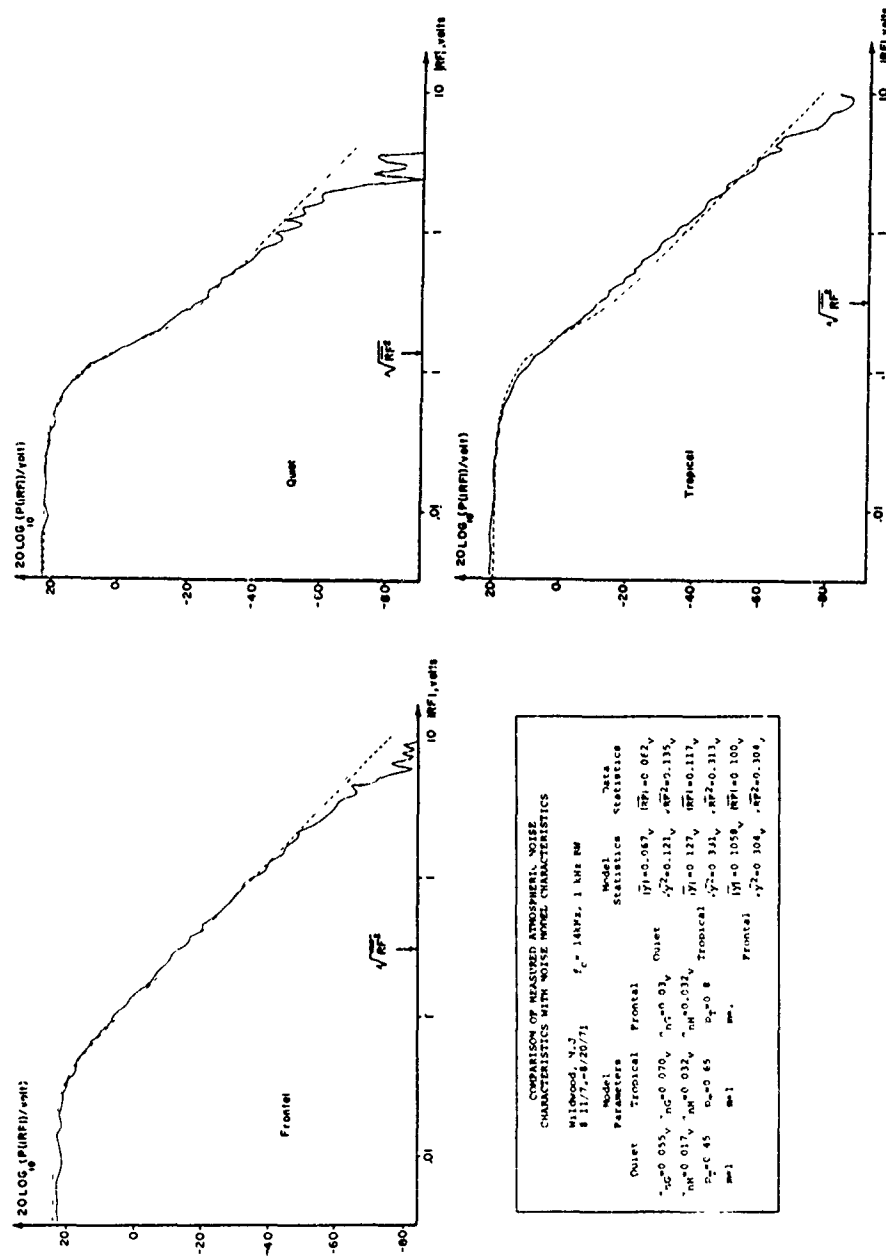


Figure 3-5. Comparison of Model to VLF Noise Observations

our model provides four parameters, we cannot infer that it has any unique aspects as a single channel model, only that it does have the flexibility to match the data to the degree shown in Figure 3-5.

3.6.3 Comparison with Additional Joint Channel Characteristics

To provide further evidence of the validity of the joint channel model, the conditional density of the rf noise was measured using a hardware conditioning circuit. The rf sample was taken from frequency channel 1 and the digitized sample stored in a holding register. This sample was then written into the memory, becoming part of the sample record, only if the next envelope sample from frequency channel 2 fell within a variable threshold window determined by two level detectors. This technique allowed longer sample records at a given conditioning envelope value than were obtained with the continuous joint sample records previously described. This increased length provided better probability density estimate stability.

If we assume that the joint probability density of these samples was dominated by the joint Hall component density, then the conditional rf density is given by

$$p_{y|v_o}(y, v_o) \approx \frac{1}{p_{vH}(v_o)} \cdot p_{yH, vH}(y, v_o).$$

Using pdf expressions (3.9) and (3.11) and transforming to normalized y' and v' variables via the relations $y' = y/\sigma_{nH}$ and $v' = v/\sigma_{vH}$ results in the normalized conditional rf noise density for $m = 1$

$$p_{y'|v'_0}(y', v'_0) = \frac{4(v'_0{}^2 + 1)^{3/2}}{\pi(y'^2 + v'_0{}^2 + 1)^2}, \quad 0 \leq v'_0 < +\infty, \quad 0 \leq |y'| < +\infty. \quad (3.29)$$

Four conditional sample records were used, each 8000 samples long, with the value of the conditioning envelope, v'_0 , related between records by a power of 2. The expression (3.29) was matched to the second record at $y' \rightarrow 0$ and at a large value on the tail of the observed density. This two-point fit provided a value of $v'_0 2^n$, $-1 \leq n \leq 2$, for all of the records and the scale factor for y' relating the normalized coordinates to the observed voltage scales. The conditional pdf (3.29) was then plotted for the remaining three records with the appropriate power of 2 change in v'_0 . The comparative results are shown in Figure 3-6 where we have used two plots to separate the sequential values of conditioning envelope. The normalization was performed relative to the plot labeled $130 \leq E_{f2} \leq 170$ mv. It would appear from these data that the joint channel model pdf does provide a useful description of the actual behavior, in particular, the model predicts the sharp reduction in slope of the density tail, compared to the unconditioned rf noise density of the previous figures in this chapter.

We have noted (section 3.5.1) that the ratio of mean to rms has often been used to characterize the non-gaussian nature of atmospheric noise envelope waveforms. This ratio for a gaussian distribution is 0.797σ , while smaller values would indicate a pdf tail that is larger than gaussian. Expressions (3.26) and (3.27) give the variance and mean value of the magnitude of the conditional Hall noise component of

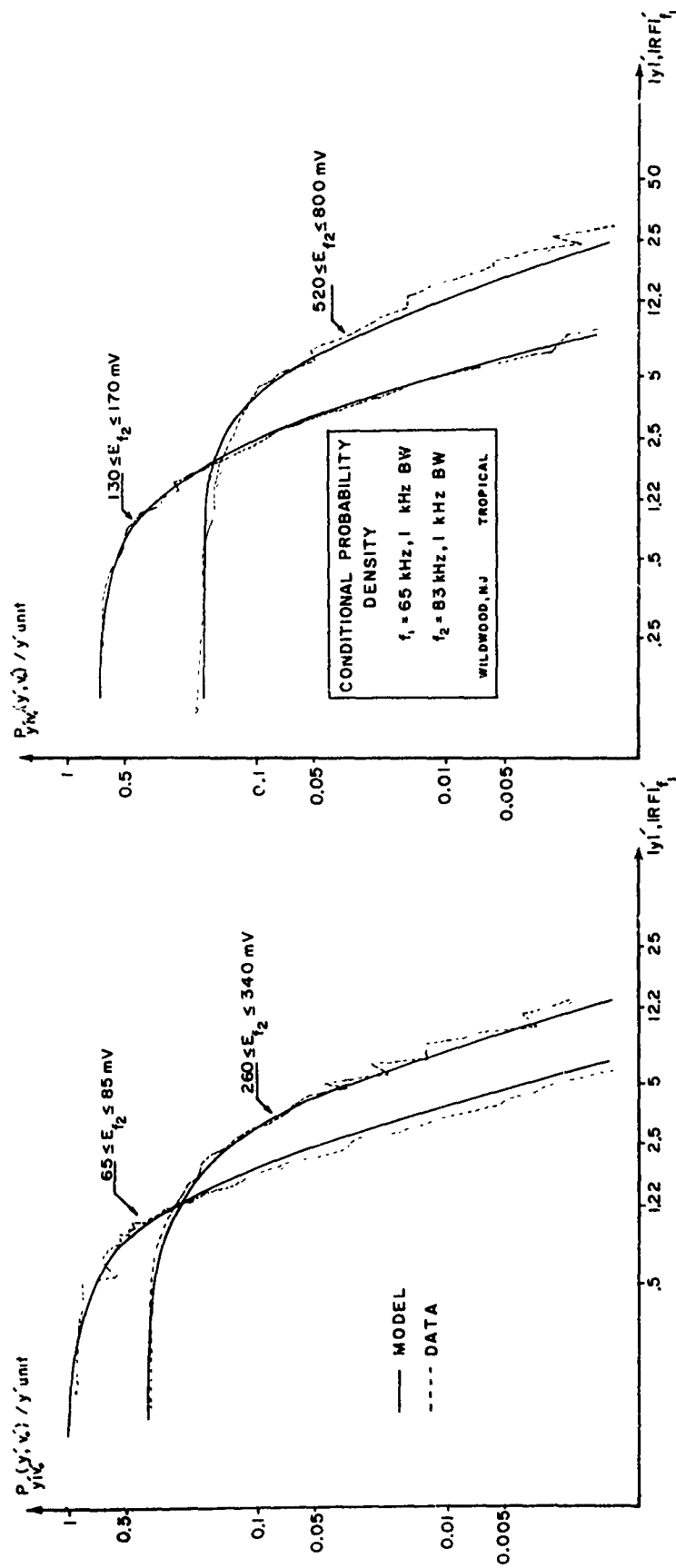


Figure 3-6. Comparison of Model Conditional Density to Tropical Observations

our model, including the effect of the instrumentation system's dynamic range. The limiting value of this ratio, for large values of y_{\max} , is seen to be

$$\lim_{\substack{y_{\max} \rightarrow \infty \\ v_o \ll y_{\max}}} \frac{\text{Expression (3.27)}}{\sqrt{\text{Expression (3.26)}}} = \frac{\frac{2}{\pi} \left[v_o^2 / \sigma_{vH}^2 + 1 \right]^{1/2}}{\left[\frac{2}{\pi} \left(v_o^2 / \sigma_{vH}^2 + 1 \right) \tan^{-1} \infty \right]^{1/2}} = \frac{2}{\pi} \approx .636.$$

For the entire range of our noise model (i.e., background component to Hall component), we would expect that the ratio of the mean to rms of the conditional $|rf|$ noise distribution is gaussian for small values of the pilot channel envelope where only the gaussian background component of the noise is present ($x(t) = 0$), decreasing to the lower Hall component limit given above and then rising towards unity as the upper limit y_{\max} is approached by the pilot channel envelope.

The Hall component ratio was evaluated numerically and found to be relatively insensitive to the exact values of σ_{nH} and σ_{vH} . The result is shown in Figure 3-7 for the case $m = 1$, along with several plots of the actual ratio computed from the joint channel data for $m = 1$ noise conditions. We see that the data ratio follows the general behavior predicted by the model, in particular, the increase towards gaussianity at small values of the pilot channel envelope supports the concept of the background gaussian component of the atmospheric noise. The actual point of this transition is dependent upon relative channels gains and hence has no significance. The subscript at each rf channel frequency is the observation bandwidth in kHz and we see that there is a definite trend

to lower values of the mean-rms ratio at the 10 and 20 kHz bandwidths. This indicates that the specific form of the joint channel pdf is less effective at these bandwidths, even though the particular data match used in Figures 3-1 through 3-4 (conditional $\sigma_{y|v_0}$ statistic) agrees quite well.

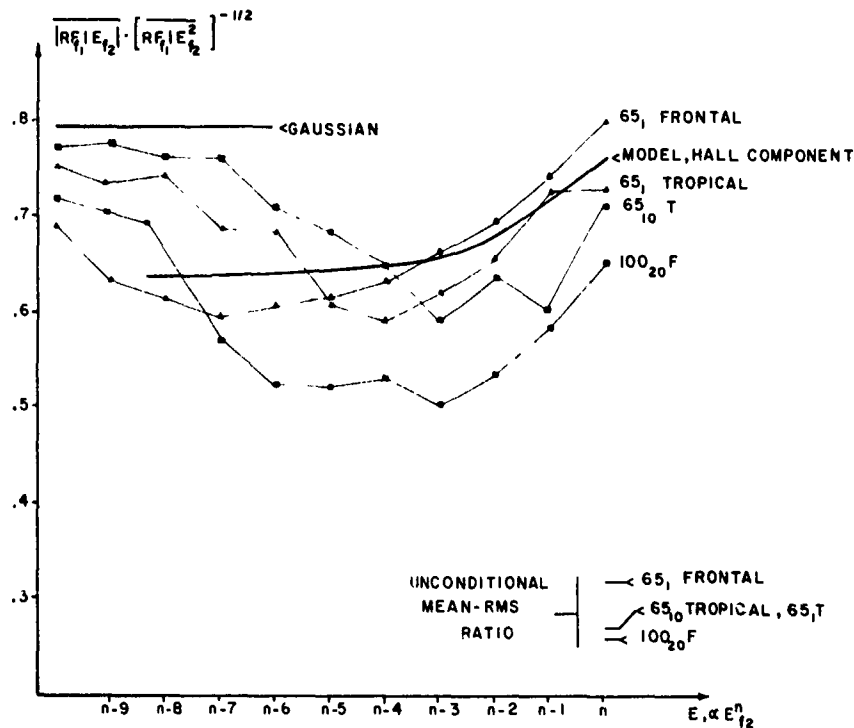


Figure 3-7. Comparison of Mean-RMS Ratio for Conditional RF Noise Magnitude Density

3.7 Noise Model Time Structure

We have specified, at this point, the time structure of two components of our noise model. The gaussian processes $n_1(t)$ and $n_2(t)$, in the model

$$y(t) = n_1(t) + x(t) a(t) n_2(t),$$

are assumed statistically independent, with each having jointly gaussian statistics with correlation determined completely by the bandlimiting filter's impulse response. Since we have specified $x(t)$ as a two-state process, it would be very difficult to specify a time structure of $x(t)$ $a(t)$ that would generate sample records exactly like the type seen in Figure 2-4. However, the fact that we seek principally a model that is useful in radio receiver design relieves a considerable amount of the problem of exact specification of short-time structure. The reason for this is that all VLF-LF receivers must employ sharp bandlimiting filters to remove adjacent channel interference. Signals designed for these radio systems must provide long observation times relative to these bandwidths^{18, 31-33} and thus a noise model that describes the average behavior of the noise waveform over these time intervals is adequate. Our goal in this section is to postulate a time structure for $x(t)$ $a(t)$ that approximates the observed behavior reported in Chapter 2 in the moderate and long-time sense and does not compromise the first order model characteristics given in 3.6.

From the time structure observations reported in Chapter 2, we recall that the bandlimited atmospheric noise waveform has a power spectral density determined by the bandlimiting filter. Measurements of the fluctuating power level of the noise (the estimates $A(t_i)$ closely related to the $x(t)$ $a(t)$ model component) showed that it was essentially uncorrelated beyond the filter correlation time, although secondary correlations of 3-4 msec and 300-500 msec were observed and related to mechanisms of the noise-generating process. In terms of the ultimate problem of receiver design, these observations indicate that the first

order pdf of the noise is the most important characteristic to be modeled. Where the fluctuating noise power level is important due to assumed signal characteristics, one can use the joint channel model to estimate the instantaneous value to $x(t)$ $a(t)$ more accurately than an attempt to exploit the small time structure component in the $A(t_i)$ series. Thus our efforts in this section are directed at completeness of the model and the development of a canonic model, including time structure, suitable for Monte Carlo computer simulation, rather than an ultimate use of the $x(t)$ $a(t)$ time structure in the receiver design problem.

3.7.1 General Time Structure

The proposed time structure of the $x(t)$ $a(t)$ component of our noise model is the following:

- a) The two-state process $x(t)$ is Markov with transition rates $\lambda_{01}(t)$ and λ_{10} . The λ_{10} rate is constant and chosen to provide the short-time correlation of $A(t_i)$. The $\lambda_{01}(t)$ rate is stochastic and controls the time intensity of the non-gaussian excursions caused by $x(t) = 1$.
- b) The stochastic rate $\lambda_{01}(t)$ is driven by a statistically independent, two-state Markov process $w(t)$ with transition rates μ_{01} and μ_{10} . The μ_{10} transition rate is constant and chosen to provide the long-time correlation associated with multiple discharges. The μ_{01} rate is also constant and is chosen to provide an approximation to the magnitude of the long-time correlation observed in the $A(t_i)$ record.
- c) The process $a(t)$ is a nonlinear function of $x(t)$: $a(t)$ assumes a

fixed value, described by the random variable a with pdf given by (3.2), for each discrete transition of $x(t)$ from 0 to 1. Each succeeding value of $a(t)$ is statistically independent of those preceding.

We see that the effect of our model is to describe each burst event, at the output of the bandlimiting observation filter, as a noise burst of constant power level which is a random variable for different burst events. The occurrence intensity of these discrete noise bursts is further modulated by a two-state intensity process, approximating the occurrence of single discharge events and the near continuum of noise found in multiple discharges. This type of model is similar to that originally proposed by Furutsu and Ishida¹⁰ and recently used by Coon⁹ in the development of an analog noise simulator. Their approach used a train of Poisson distributed impulses to excite the bandlimiting filter, with additional burst packets of impulses described by a higher intensity Poisson process to represent multiple discharges. Our noise burst model has a plausible basis in the leader structure of single discharge events which, at frequencies of LF and above, tend to appear as a short burst of noise. Where the burst energy is more time concentrated, we are simply approximating the effect as a noise burst since we are interested in the effects on a scale of milliseconds or longer. For the case of multiple discharges, we observed in Chapter 2 that these events are characterized by an additive combination of a continuum noise burst and shorter, high intensity bursts. Our model tends to provide this behavior, with the continuum noise approximated by the high intensity event rate and the random variable " a ", describing each discrete power level, causing

large excursions to model high intensity bursts. The model implicitly ignores the correlation of noise burst amplitude with time intensity as observed for multiple discharges. This preserves the first order model as presently developed.

3.7.2 Functional Form of the Model Time Structure

The assumed form of the time structure for $x(t)$ $a(t)$ now allows us to determine the functional relationship of the $A(t_i)$ estimates to the model and hence estimate the model parameters necessary to provide the model with the experimentally observed characteristics. The $A(t_i)$ estimates were generated by an integrate-sample-dump technique which is mathematically equivalent to the system shown in Figure 3-8. We see

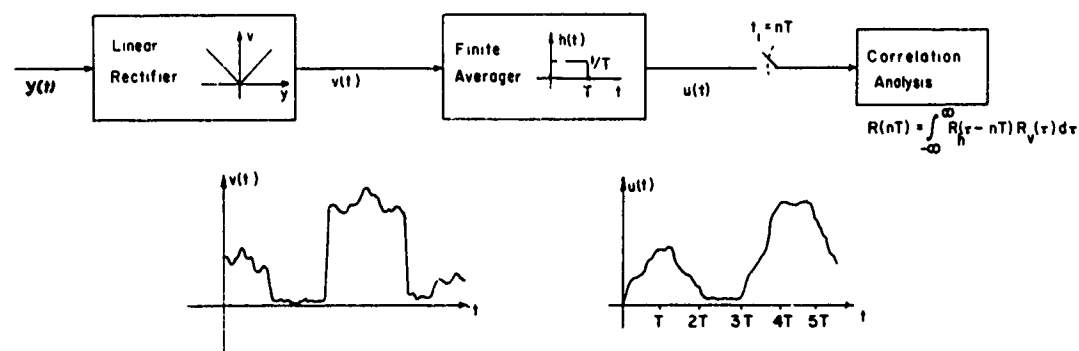


Figure 3-8. Equivalent $A(t_i)$ Generator

from the well-known relations among autocorrelation functions that we can determine the form of the $A(t_i)$ time series autocorrelation by cascading the effect of each autocorrelation function. To determine the form of the autocorrelation of $v(t)$ (where we neglect double frequency

terms from the linear rectification of the bandpass $y(t)$ waveform) we utilize the discrete nature of the Markov $x(t)$ generator to write

$$\begin{aligned} R_v(\tau) = & P(x_t=1) P_{\lambda_{10}}(N_\tau=0) \overline{v_H^2} \rho_v(\tau) + P_x(x_t=0) \left[P_{\lambda_{01}}(N=0) \overline{v_G^2} \rho_v(\tau) \right. \\ & \left. + P_{\lambda_{01}, \lambda_{10}}(N\text{-even}) \overline{v_G^2} + P_{\lambda_{01}, \lambda_{10}}(N\text{-odd}) \overline{v_G} \overline{v_H} \right] \\ & + P(x_t=1) \left[P_{\lambda_{01}, \lambda_{10}}(N\text{-even}) \overline{v_H^2} + P_{\lambda_{01}, \lambda_{10}}(N\text{-odd}) \overline{v_G} \overline{v_H} \right]. \end{aligned} \quad (3.30)$$

In the first term of (3.30) $P(x_t=1)$ is the probability that $x(t) = 1$, which is stochastic and slowly varying as determined by the second Markov generator (3.7.1-(b) above). $P_{\lambda_{10}}(N_\tau=0)$ is the τ dependent probability that zero Poisson distributed transitions, at rate λ_{10} , occur in time τ , and $\overline{v_H^2} \rho_v(\tau)$ is the autocorrelation of the Hall component envelope. The function $\rho_v(\tau)$ is the normalized autocorrelation of a linear envelope detector driven by a narrow-band gaussian process.³⁴ The remaining terms represent the other possible combinations of Poisson events at time $t + \tau$ given $x(t) = 1, 0$ at time t . These terms may be regrouped in order of importance to yield

$$\begin{aligned} R_v(\tau) = & p_x e^{-\lambda_{10}\tau} \overline{v_H^2} \rho_v(\tau) + f_1(\overline{v_H^2}) + f_2(\overline{v_G} \overline{v_H}) \\ & + f_3(\overline{v_G^2}) + f_4(\overline{v_G^2} e^{-\lambda_{10}\tau}) \end{aligned} \quad (3.31)$$

The first term then is dependent upon the variance of the Hall envelope component, the autocorrelation of the noise envelope and the exponential

decay of the $P_{\lambda_{10}} (N=0)$ term. The second term represents uncorrelated averages of v_H caused by $x(t)$ transiting an even number of times during time τ , while the last terms represent much smaller effects.

Neglecting for the moment the time dependence of $p_x(t)$, which will be used to model the 300-500 msec multiple discharge effects and hence will not affect the short term behavior, and assuming the $\rho_v(\tau)$ function decays rapidly to a $\rho_v(\infty)$ value (valid for 1 kHz and larger rf bandwidths with $\tau > 1$ msec), we see that the sampled autocorrelation values are given by

$$R_{A(t_i)}(nT) = \int_{nT-T}^{nT+T} \underbrace{\overline{p_x(t)} e^{-\lambda_{10}\tau} \overline{v_H^2} \rho_v(\infty)}_{R_v(\tau)} \cdot \underbrace{\left[\frac{1 - |nT-\tau|}{T} \right]}_{R_h(nT-\tau)} d\tau$$

+ constant terms, $n \geq 1$

$$R_{A(t_i)}(nT) = \overline{p_x(t)} \overline{v_H^2} \rho_v(\infty) \left[e^{-(nT+T)\lambda_{10}} \left(\frac{1}{\lambda_{10}} + nT \right) \right. \\ \left. + e^{-(nT-T)\lambda_{10}} \left(\frac{1}{\lambda_{10}} + nT \right) - \frac{2}{\lambda_{10}} e^{-nT\lambda_{10}} (nT\lambda_{10} + 1) \right]$$

+ constant terms. (3.32)

Thus the autocorrelation of the model $A(t_i)$ series is, for short-time, dependent upon first order amplitude statistics previously specified $\left(\overline{p_x(t)} \text{ and } \overline{v_H^2} \right)$ and an exponential decay, with parameter λ_{10} of the Markov $x(t)$ generator. Physically, the parameter λ_{10} is related to the average length of single discharge events, which is of the order of 1 msec. The exact choice of this parameter will be based on simulation

results given in section 3.7.3 below.

For correlation times $nT \gg \frac{1}{\lambda_{10}}$ the dominant short-time term of (3.32) will decay to zero and the $A(t_i)$ autocorrelation will be given by

$$R_{A(t_i)}(nT) = \overline{p_x(t) p_x(t+nT)} \bar{v}_H^2 + \text{second order terms } (\bar{v}_G \cdot \bar{v}_H \cdot \bar{v}_G^2), \quad (3.33)$$

where we treat $R_h(\tau)$ as a unit delta function with respect to the slow variation of $\overline{p(t) p(t+nT)}$ which will be of the order of hundreds of milliseconds. The first term of (3.33) is the first term of the second square brackets of (3.30) where we have used the $nT \gg \frac{1}{\lambda_{10}}$ assumption to neglect transients in the $x(t)$ generator. The joint probability, $P(x(t) = 1, x(t+nT) = 1)$, will only be influenced by the stochastic intensity $\lambda_{01}(t)$.

To evaluate $\overline{p_x(t) p_x(t+nT)}$ we make the following definitions and observations concerning the Markov generated $w(t)$ which controls $\lambda_{01}(t)$:

- a) $w(t)$ is the state of the second Markov generator controlling the $x(t)$ intensity. $w(t)$ has rate parameters μ_{01} and μ_{10} .

$$b) \quad w(t) = 1 \longleftrightarrow \lambda_{01}^f \rightarrow p_x^f = \frac{\lambda_{01}^f}{\lambda_{01}^f + \lambda_{10}}$$

$$w(t) = 0 \longleftrightarrow \lambda_{01}^s \rightarrow p_x^s = \frac{\lambda_{01}^s}{\lambda_{01}^s + \lambda_{10}}.$$

$$c) \quad p_w = P(w_t=1) = \frac{\mu_{01}}{\mu_{01} + \mu_{10}}, \quad q_w = 1 - p_w,$$

$$k = \mu_{10} + \mu_{01} = \mu_{10}/q_w.$$

d) The $w(t)$ state equations are given by²⁷

$$\begin{bmatrix} p(w(\tau)=0) \\ p(w(\tau)=1) \end{bmatrix} = \begin{bmatrix} p_w e^{-k\tau} + q_w & q_w(1-e^{-k\tau}) \\ p_w(1-e^{-k\tau}) & q_w e^{-k\tau} + p_w \end{bmatrix} \cdot \begin{bmatrix} p(w(0)=0) \\ p(w(0)=1) \end{bmatrix}.$$

The $\overline{p_x(t) p_x(t+nT)}$ term with $nT \gg \frac{1}{\lambda_{10}}$, can now be evaluated using the discrete states of $w(t)$ as

$$\begin{aligned} \overline{p(t) p(t+nT)} &= P(x_t, x_{t+nT} = 1 \mid w_t, w_{t+nT} = 1) P(w_t, w_{t+nT} = 1) \\ &\quad + P(x_t, x_{t+nT} = 1 \mid w_t = 0, w_{t+nT} = 1) P(w_t = 0, w_{t+nT} = 1) \\ &\quad + P(x_t, x_{t+nT} = 1 \mid w_t = 1, w_{t+nT} = 0). \end{aligned}$$

$$P(w_t = 1, w_{t+nT} = 0) + P(x_t, x_{t+nT} = 1 \mid w_t, w_{t+nT} = 0) P(w_t, w_{t+nT} = 0).$$

Using the chain rule for conditional Markov probabilities and the state equations given above, the expression becomes

$$\begin{aligned} \overline{p_x(t) p_x(t+nT)} &= (p_x^f)^2 p_w (q_w e^{-knT} + p_w) + p_x^f p_x^s q_w (p_w - q_w e^{-knT}) \\ &\quad + p_x^f p_x^s p_w (q_w - q_w e^{-knT}) + (p_x^s)^2 q_w (p_w e^{-knT} + q_w). \end{aligned}$$

This can be rearranged to yield

$$\overline{p_x(t) p_x(t+nT)} = e^{-knT} \left((p_x^f)^2 p_w + (p_x^s)^2 q_w - p_x^2 \right) + p_x^2, \quad (3.34)$$

where

$$p_x \triangleq \overline{p_x(t)} = p_w p_x^f + q_w p_x^s.$$

We recognize the left term of (3.34), which is the dynamic portion, to be the variance of a two state process with state values p_x^f and p_x^s and probabilities p_w and q_w , respectively, while the right term of (3.34) is the average value squared of the process. Combining (3.34) with (3.33) we have the long-time behavior of the $A(t_i)$ model autocorrelation given by

$$R_{a(t_i)}(nT) = \left[e^{-knT} \left(\sigma_{p_x(t)}^2 \right) + p_x^2 \right] \bar{v}_H^2 + \text{second order terms } (\bar{v}_G^2, \bar{v}_G \bar{v}_H). \quad (3.35)$$

The model time structure provides five independent parameters. The first two, λ_{10} and $k = \mu_{10}/q_w$ are chosen to provide the approximate exponential decay of the data for short-time and long-time, respectively. The difference in the form of these two decay parameters is caused by the respective sources of the correlation. For short-time, the correlation depends upon the length of each noise burst which is the probability of zero Poisson distributed transitions in the time interval nT , whereas the latter depends only upon $x(t)$ being in state 1 at the beginning and end of the time interval, independent of the number of intervening transitions or "path" of $x(t)$.

The remaining three parameters are related by two equations and an inequality. The average probability of $x(t)$ must equal that required by the first-order model,

$$\overline{p_x(t)} = p_{\text{model}} = p_w p_x^f + q_w p_x^s = p_x. \quad (3.36)$$

The range of the $x(t)$ probability can be determined from the data as a normalized ratio

$$\overline{p_x(t)^2} / \overline{p_x(t)}^2 = \frac{\left[(p_x^f)^2 p_w + (p_x^s)^2 q_w \right]}{p_x^2}$$

$$\approx R_{A,Data}(10 \text{ msec}) / R_{A,Data}(\infty) \triangleq RDATA, \quad (3.37)$$

and finally, we have the normal probability constraint

$$0 < p_x^s, p_x^f \leq 1. \quad (3.38)$$

In selecting a parameter set to satisfy these relations, two cases arise. The first occurs when $p_x^f < 1$ and a non-unique solution exists. We can arbitrarily select $p_w = q_w$, which leads to symmetric p_x^f and p_x^s values. It can be shown that this choice minimizes the difference, $p_x^f - p_x^s$, for a given RDATA ratio. The parameters for this case are

$$p_w = q_w = 0.5, \quad p_x^f = p_x + p_x \sqrt{RDATA - 1}, \quad p_x^s = p_x - p_x \sqrt{RDATA - 1}. \quad (3.39)$$

It is also possible to arbitrarily assign p_x^f at a large value to represent the near continuum noise of multiple discharges, or find that (3.39) results in $p_x^f > 1$ for given p_x and RDATA values, in which cases the remaining two parameters, p_w, p_x^s , are given by the solutions of

$$p_w^2 \left[(p_x^f)^2 - p_x^f \right] + p_w \left[p_x^f - 2p_x p_x^f + RDATA p_x^2 \right] + \left[p_x^2 - RDATA p_x^2 \right] = 0,$$

$$p_x^s = \frac{p_x - p_x^f p_w}{1 - p_w}. \quad (3.40)$$

The equation set (3.40) reduces to two linear equations for the second

case where $p_x^f = 1$. This is representative of tropical and frontal conditions.

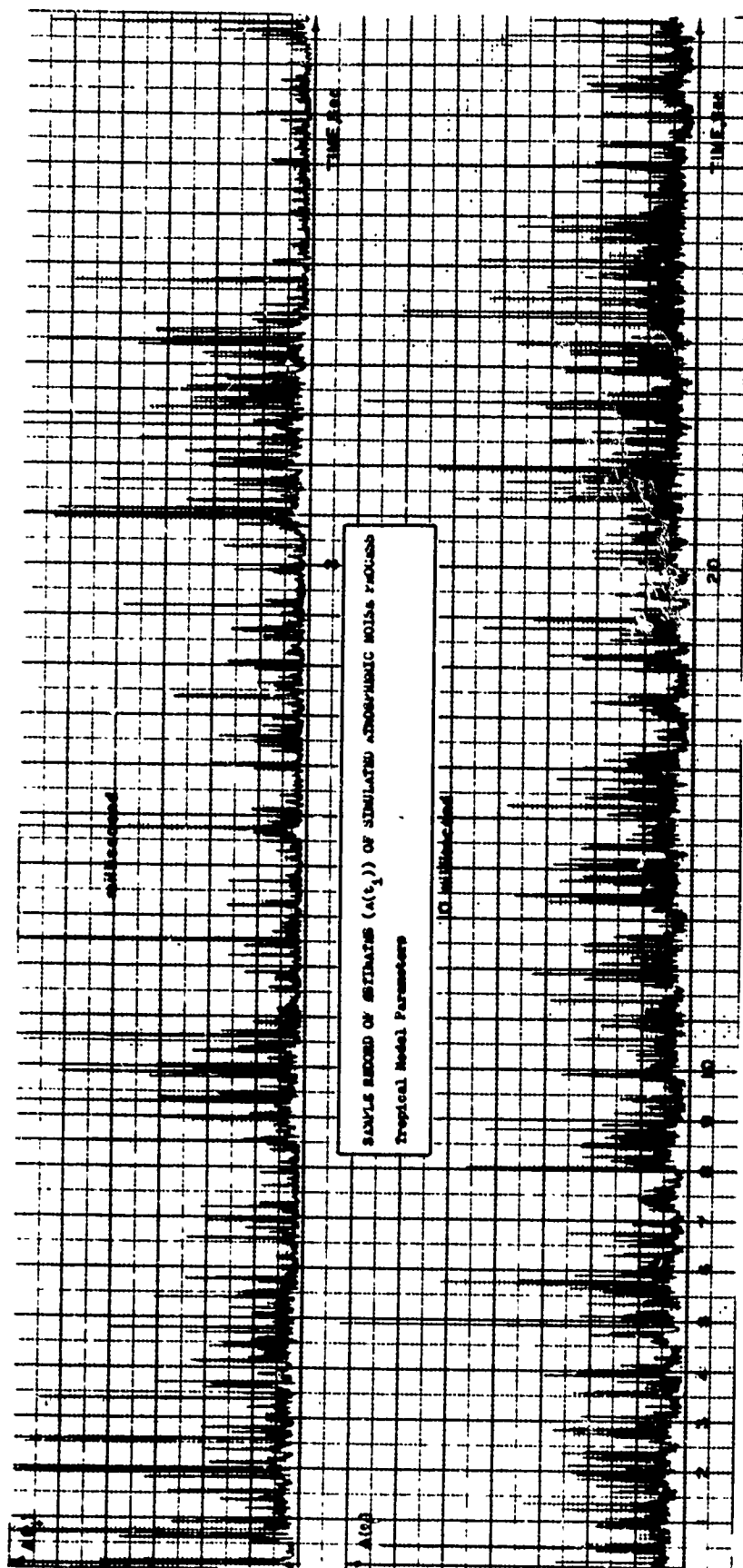
We noted in our discussion of the observed $A(t_i)$ sample record (section 2.5.2) that the behavior suggests a slowly varying continuous modulation of $a(t)$ combined with the uncorrelated fluctuations. The two-state intensity modulation proposed here is a coarse approximation to this and one might wonder why not modulate the intensity of $x(t)$ by a continuous lowpass random process. We explored this idea through computer simulations of $A(t_i)$ and found that the technique works well for moderate values of p_x . For the larger values of p_x , $.6 < p_x < .9$, as required for tropical and frontal conditions, the nonlinear relation between modulation of $\lambda_{10}(t)$ and $p_x(t)$ introduced by the relation $p_x(t) = \lambda_{01}(t)/(\lambda_{01}(t) + \lambda_{10})$ makes it difficult to control either p_x or the effective correlation structure. The former effect then compromises the first-order noise model which is very undesirable. For these reasons we have concluded that a two-state or Poisson-Poisson model is the better form, short of incorporating amplitude correlation with the time noise burst intensity. Our model for $x(t)$ $a(t)$, then, yields a functional behavior similar to that found in the experimental observations and can be related to the physical mechanisms of the atmospheric noise sources. Further, the time structure parameters can be chosen in a manner consistent with the first order model parameters and these choices do not depend in an absolute sense upon moment statistics of the first order model. In the next section we shall demonstrate, via a computer simulation, that the combined first-order and time structure parameters lead to simulated $A(t_i)$ sample records and autocorrelation that agree well with observations.

3.7.3 Time Structure Simulation Results

To verify that the model time structure produces the type of behavior predicted in the previous section, and that the results are compatible with the first-order model parameters, a Monte Carlo simulation was run for several cases. The details of the complete atmospheric noise simulation generator are given in section 3.8 and Figure 3-11. For our purposes here, the $x(t)$ and $v(t)$ two-state generators were simulated with uniform random generators mapped to an exponential pdf to produce the time of the next switching event. Each $A(t_i)$ 1-msec sample was composed of the sum of five Rayleigh-distributed, statistically independent, samples $(R(\sigma_{vG}))$, plus additional Rayleigh-distributed samples $R(a_x \sigma_{vH})$ for the time period that $x(t) = 1$. The second Rayleigh parameter, a_x , was generated for each $x(t)$ 0-1 transition from a $\chi(m, 1)$ distribution, generated according to (3.1). All of the parameters in these distributions were taken from the first first-order model parameters summarized in Table 3-1 in section 3.8.

A simulated sample record of the $A(t_i)$ estimates is shown in Figure 3-9 with tropical first-order parameters and time structure parameters described below. Comparison of this record with Figure 2-7, the observed $A(t_i)$ time series, shows a reasonable imitation, although the distinct undulating behavior of the observed data is not present in the simulation.

An autocorrelation of the simulated $A(t_i)$ estimates is shown in Figure 3-10. The two decay parameters were empirically selected to produce the results shown there. Equations (3.40) were used to determine the remaining three parameters as



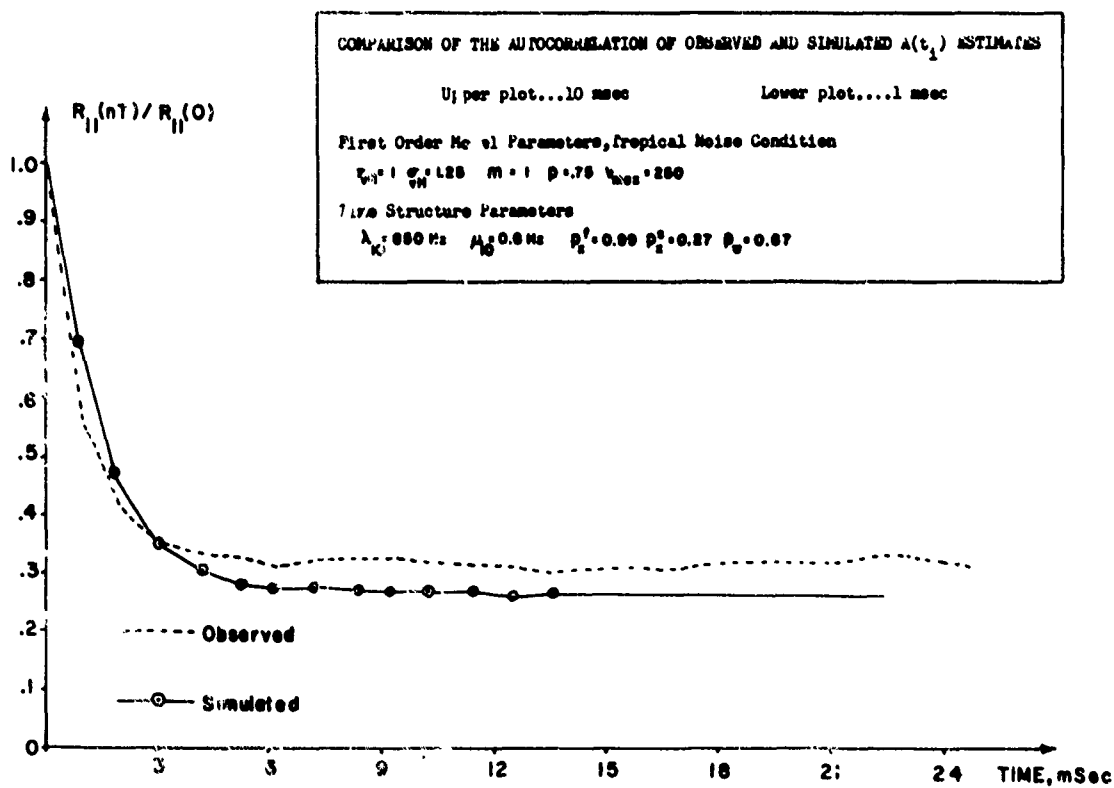
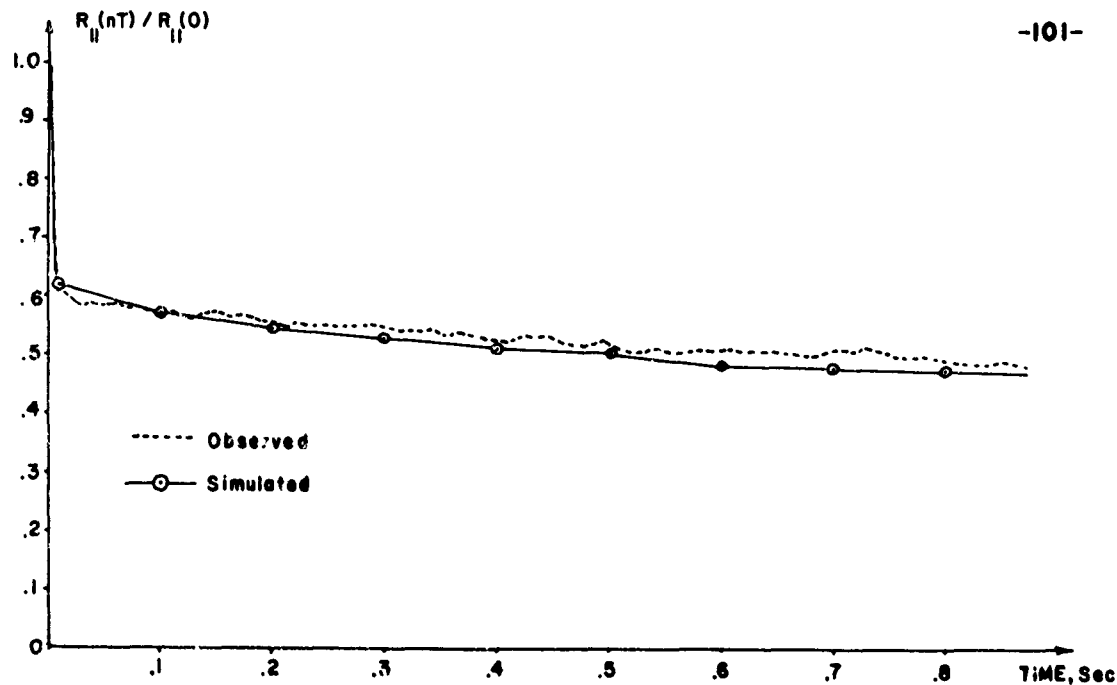


Figure 3-10. Autocorrelation of Simulated $A(t_1)$ Sample Record

RDATA estimated by (3.37) = 1.22

$$p_x^f = .99, \rightarrow p_w = 0.66, \rightarrow p_x^s = 0.27.$$

Since the short-time decay parameter, λ_{10} , is independent of all other parameters and our observations indicated that this decay was found for all noise conditions, the empirical value of 850 Hz is similarly valid for all noise conditions. The long-time decay parameter, μ_{10} , must be computed for each parameter set as $\mu_{10} = 2q_w$, where k value of 2 Hz is assumed to be representative of all multiple discharge phenomena. The model time structure produces the results shown in Figure 3-10 for all noise conditions except frontal where the large value of p_x , combined with the model's lack of amplitude correlation with $x(t)$ intensity, prevents a sufficiently large value of $\sigma_{p_x}^2$ to match the observed autocorrelation. All of the time structure parameters are summarized in section 3.8 below.

3.8 A Canonic Atmospheric Noise Generator

The combined first-order and time structure model for bandlimited atmospheric noise, including the joint channel model, can be conveniently realized for digital computer simulation. The noise generator is shown in Figure 3-11, where the portion above the dashed line realizes the time structure and $a(t)$ of the Hall component, whereas the lower realizes the actual envelope or rf noise samples. The upper portion is iterated each time the state of that portion changes, as determined by the random event-time samples, $TNXT$. The nonlinear mappings from Random Number Generators (RNG's) with uniform distribution ($U(0, 1)$) are

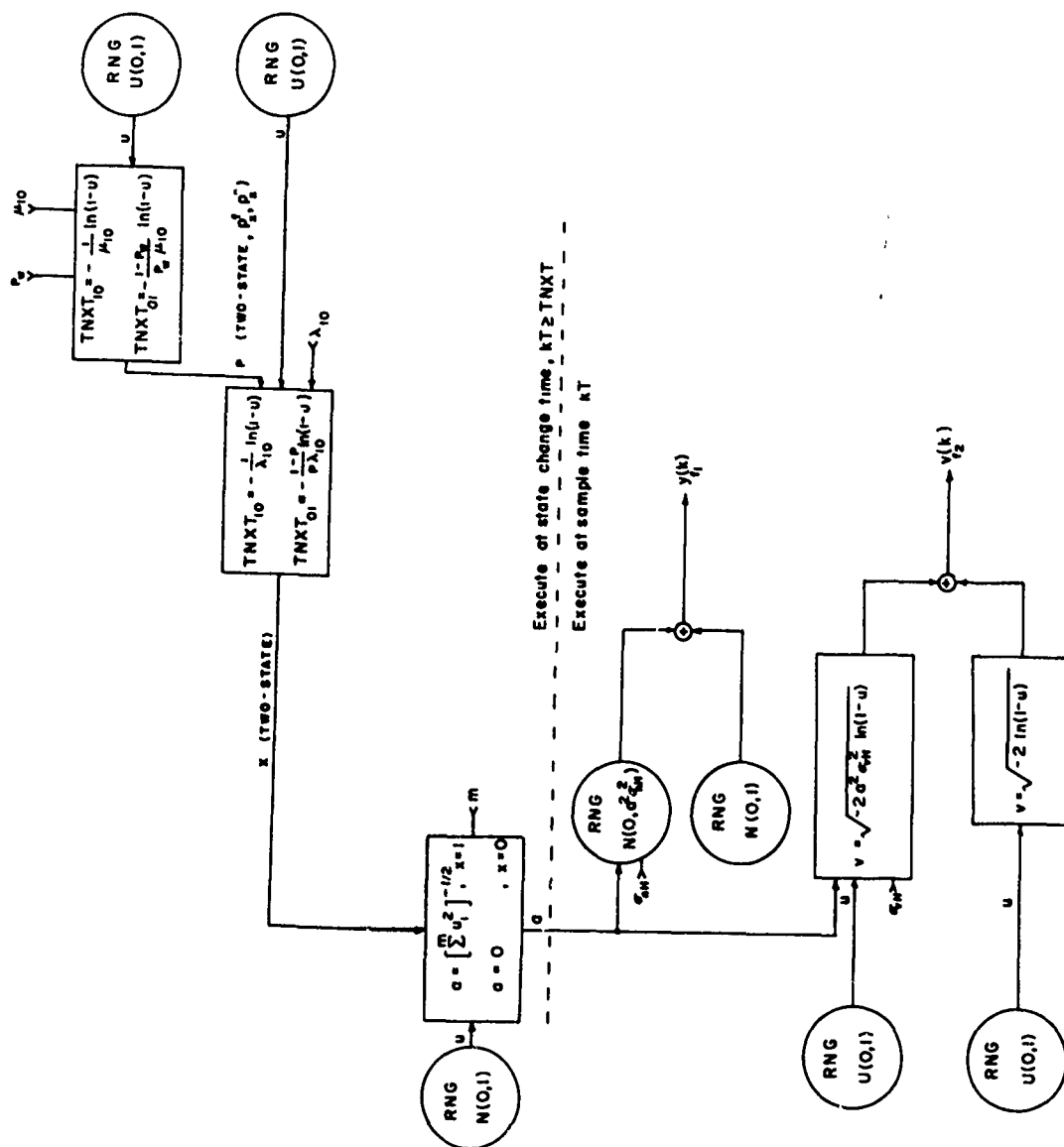


Figure 3-11. Atmospheric Noise Generator for Computer Simulation

conventional inversion formula which can be used when a desired pdf has an analytic cumulative distribution from which the inverse mapping can be obtained.³⁵ Other generator forms, such as the in-phase and quadrature phase components of the bandlimited atmospheric noise waveform can be similarly constructed. If one is interested only in statistically independent atmospheric noise samples, without consideration of time structure, the Hall component of either envelope or rf noise or the joint samples of both can be realized with U(0, 1) RNG's and the appropriate mapping. These mappings can be determined for the integer values of m that we have considered in our first-order model. Figure 3-11 does not show the truncation of sample values at the maximum upper limit of

Table 3-1. Canonic Noise Generator Parameters

CONDITION	ν_c	BW	σ_{en}	σ_{em}	m	\overline{V}	\overline{RF}	\overline{V}	\overline{E}	$\overline{V^2}$	$\overline{RF^2}$	$\overline{V^2}$	$\overline{E^2}$	max	\overline{E}	ρ_1'	ρ_2'	ρ_3'	ρ_4'	ρ_{10}
QUIET	65	10	1.8		2	1.07	0.98			4.0	4.12			92	0.11	0.11	0.11			
QUIET	65	1	2.6		2	1.19	0.96			9.06	4.25			92	0.11	0.11	0.11			
QUIET	83	1		2.22	2			1.62	1.30			9.92	11.9	120	0.11	0.11	0.11			
QUIET-NIGHT	65	1	1.2		2	1.66	1.30			10.9	12.6			100	0.5	0.75	0.25	0.5	1.0	
QUIET-NIGHT	83	1		1.34	2			2.71	3.04			18.5	25.8	134	0.5	0.75	0.25	0.5	1.0	
TROPICAL	65	10	0.6		1	2.51	2.12			74.8	63.2			250	0.75	0.99	0.27	0.66	0.6	
TROPICAL	65	1	0.54		1	2.23	1.91			57.0	47.5			250	0.75	0.99	0.27	0.66	0.6	
TROPICAL	83	1		1.28	1			6.16	6.36			289	295.8	285	0.75	0.99	0.27	0.66	0.6	
FRONTAL	200	20	3.5		1	12.78	11.5			2300	1936			1000	0.9	0.99	0.15	0.89	0.2	
FRONTAL	65	1	4.1		1	11.3	11.5			858	918			500	0.9	0.99	0.15	0.89	0.2	
FRONTAL	83	1		4.6	1			22.2	27.0			2840	3470	700	0.9	0.99	0.15	0.89	0.2	
QUIET-NIGHT	14	1	0.3		1	1.21	1.13			4.86	6.0			40	0.45	0.66	0.24	0.5	1.0	
TROPICAL	14	1	0.45		1	1.81	1.66			22.2	20.0			107	0.65	0.66	0.64	0.5	1.0	
FRONTAL	14	1	1.05		1	3.52	3.33			102	102			200	0.8	0.99	0.15	0.84	0.3	

NOTES: $\sigma_{en} = \sigma_{em} = \lambda_{0.0001} \cdot \lambda_{0.0001} / (1 - \rho_{11})$

the various pdf's. This can be accomplished either directly as the Hall component output by iterating for a new value if the maximum is exceeded or by limiting the a_i generator range as suggested by Hall. While these produce slightly different pdf's at the maximum range the differences would probably not be important in most simulation applications.

The parameters required by the model and canonic generator are given in normalized form in Table 3-1. This table is a representative summary of all of the sample records that we analyzed from the data collection program in New Jersey.

3.9 Summary

3.9.1 Model Results

In Chapter 1 we briefly described the nature of electromagnetic radiation from lightning discharges, which is the principal source of low frequency atmospheric radio noise. The complex time structure of these discharge radiations, especially at frequencies above 40-50 kHz, provide motivation for a multiplicative model of the noise, $y(t) = A(t) n(t)$, as originally suggested by Hall. This model describes the noise waveforms observed at the output of a bandlimiting filter, rather than employing the more difficult approach of statistically modeling the discharge process itself and then determining the resulting filter output statistics from this source model. We extended Hall's model by suggesting that $A(t)$ could be considered to be independent of frequency and thus provide a statistical link between noise waveforms observed in different frequency channels.

In Chapter 2 we reported various experimental observations made

at VLF and LF to explore what statistical and dynamic behavior of $A(t)$ was required to approximate actual noise waveforms. Chapter 3 has developed two aspects of a mathematical model based on the multiplicative concept and compared them to the observed data to determine appropriate parameters. Our proposed model for bandlimited atmospheric noise waveforms is given by $y(t) = n_1(t) + a(x(t)) n_2(t)$, where $n_1(t)$ is a statistically independent background gaussian process, $x(t)$ is a two-state Markov process with a time-varying transition rate parameter and $a(x(t)) n_2(t)$ is the multiplicative process given by Hall where the $x(t)$ process acts to "turn-on" or "turn-off" this Hall component in a particular manner. In addition, $a(x(t))$ is independent of frequency over significantly large frequency increments and is thus identically the same for noise waveforms observed over this increment. This noise model represents a synthesis of three previously suggested models, including Hall's, with the addition of our concept of the frequency independence of $a(x(t))$.

Our principal comparison of this noise model to experimental observations was based on records of effectively simultaneous samples of the noise envelope in one channel and the rf noise in a second, both in the LF band. We found that the model and associated six parameters would satisfactorily describe each channel's unconditional probability density and a conditional statistic's variation linking the channels. These six parameters compare to eleven parameters required to simply fit mathematical expressions to all three curves. We further demonstrated that the joint channel model (the fact that $a(x(t))$ is common) predicted the basic form and relation of the conditional rf noise pdf measured with a different technique, and predicted the basic relationship of a

-107-

different joint channel statistic than used in comparing the model with the data.

The basic time structure of our model, introduced to model the observed dynamics of $A(t)$, is provided by the stochastic nature of the $x(t)$ transition which acts to "turn-on" the $a(x(t)) n_2(t)$ noise burst. The average length of each burst is approximately equal to that reported for individual lightning discharge events. This behavior of $a(x(t))$ provides a basically uncorrelated structure for $A(t)$, with a small second-order correlation extending over several milliseconds. The long-time correlation observed of $A(t)$ is approximated in the model by modulating the intensity (Poisson rate parameter) of $x(t)$ with a second two-state process which corresponds roughly with long multiple discharge phenomena. The model also provides the correct autocorrelation of $y(t)$ itself via the time structure of $n_1(t)$ and $n_2(t)$, although this fact is relatively unimportant in typical low frequency signal processing design problems.

Finally, we interpreted the noise model relations in terms of a block diagram of a canonic noise generator, suitable for Monte Carlo computer simulations. This generator, together with both first-order and time structure parameters, was used to demonstrate that a simulated $A(t_i)$ time series yielded the same autocorrelation as that of the data.

3.9.2 Additional Questions

The experimental program described here was, of necessity, an attempt to collect specific data based only on the general concept of a multiplicative noise model. The final form of the model in turn suggests

a number of more specific experimental questions. In general these relate to the variation of the model parameters with band center frequency, joint channel frequency separation and observation filter bandwidth. We suspect that the form of the model is applicable to much higher frequencies than those tested here, principally because the leader structure of the lightning discharges, which appear as a noise burst, becomes dominant with increasing frequency. Appropriate questions regarding joint channel separation might involve more precise measurement of conditional densities at varying separations, using matched filter envelope responses, and perhaps experimentation with other channel waveforms or the use of more than one additional channel.

Questions relating to the effect of the observation filter bandwidth are perhaps the most important since this enters intimately into any radio system design. We have used bandwidths of 1, 10, and 20 kHz and have not found significant differences in the first-order model parameters at these bandwidths, although the results of section 3.6.3 indicated that the specific form of the conditional rf noise density seemed less appropriate at the larger bandwidths. A check of the absolute values of σ_{nG} and σ_{nH} used in the tropical model at 1 and 10 kHz showed that they differed by approximately the ratio of the square root of the noise power bandwidths of the two filters used. This is the result one would expect for a process that appeared as bursts of noise, relative to the filter impulse response. Conversely, this would imply that one could scale the model parameters given in Table 3-1 for differing bandwidths, using this bandwidth factor, at least above 1 kHz. However, as the bandwidth is reduced significantly below this value, the time width of individual discharges will approach

the time constant of the filter and clearly this will affect the model parameters in a nonlinear manner since the lower limit of such bandwidth reduction must be a gaussian noise process. In terms of the qualitative changes in our model parameters, we would expect that the relative level of the gaussian background process would increase and the value of p_x would decrease with decreasing rf bandwidth. This means that a noise pdf such as associated with tropical conditions would trend towards that found for quiet-night or quiet with a decreasing rf bandwidth.

This type of change in noise pdf is important in signal processing design for, as will be seen in the next chapter, there is an 8 dB difference in signal-to-noise ratio improvement that can be obtained, with a simple nonlinearity, for tropical as compared to quiet noise conditions. Intuitively, the wider rf bandwidth preserves the effects of individual discharges whereas the smaller bandwidth tends to blend the lower level effects of these together, contributing to the rise in the apparent background level. In terms of signal processing, the lower level blending "gaussianizes" the noise in those time regions and prevents the processing structure from discriminating against the effects of the original discharges. In general, then, one would want to use the smallest rf bandwidth at which significant changes in the noise pdf's begin, and our observations do not provide this information. However, since there are relatively few changes in pdf character from 1 to 10 kHz, our noise model and supporting parameter table does represent the "best" (in a signal processing sense) noise characteristics one could obtain from such an optimum bandwidth selection.

In the next chapter we shall apply the noise model to the design and performance analysis of a phase-locked-loop for use in low frequency navigation systems. The predicted performance, based on the model, will be verified using computer simulations and sample records from various noise conditions.

AN OPTIMUM DESIGN FOR NAVIGATION RECEIVERS

One of the most significant problems in the design of low frequency radio receivers is the development of a performance analysis and optimization which includes the effects of non-gaussian atmospheric noise. This development requires a quantitative description of noise characteristics. We have endeavored in the preceding three chapters to develop such a quantitative model, with associated parameter sets, to describe certain aspects of bandlimited atmospheric noise. We appealed at several points in that work to our ultimate goal of developing a noise model that was useful in the receiver design problem. This, for example, justified our focus on noise characteristics at the output of the bandlimiting filter and provided our motivation for development of the joint channel noise model. In this chapter we shall use this model as a tool to analyze several typical navigation receiver processors and to specify a near optimum receiver.

We shall assume a linear signal generator model and use a sampled data phase-locked-loop (PLL) as the basic navigation receiver processor structure, with a linear time-invariant loop providing a performance reference for our analysis. This loop can be optimized for the atmospheric noise power level and for a statistically independent, gaussian distributed noise sequence, such a loop would be optimum in the mean-square error sense without restriction as to structure. We have seen that a principal characteristic of atmospheric noise is that its first-order probability density is not gaussian. To account for this we shall introduce a zero memory nonlinearity in the loop and show that we can

determine the approximate performance of such a loop by using only the first-order probability density of the noise model. We shall use the noise model pdf to compare the performance of several nonlinearities such as a hard limiter, clipper, and hole puncher to the optimum performance achievable with this loop structure.

Our experimental observations have shown that not only is the first-order probability density of atmospheric noise non-gaussian, but that samples of the noise, separated by a spacing greater than the bandlimiting filter correlation time, are uncorrelated but are not statistically independent (this produces the correlation of the $A(t_i)$ sequence, in some cases, of 0.5 to 1 second). To account for this in the navigation processor we shall use the joint channel noise model and the simultaneous pilot channel envelope observations to approximate the atmospheric noise as a gaussian process with a time-varying, random, power level. The filter which is unconditionally optimum in the mean-square error sense will then be given by a time-varying Kalman-Bucy filter. This filter will optimally compensate for the non-gaussian probability density of the atmospheric noise and for the noise time structure and its interaction with signal dynamics. Finally, all of these filters will be simulated on a computer and, for two types of simulated stochastic signal processes, the filter performance will be determined by using recorded noise sequences for all types of noise conditions, from nearly gaussian to the most severe noise associated with frontal weather systems. These tests will show that the simple nonlinear loop, with a practical nonlinear element, provides performance improvements of 6 to 16 dB compared to the time-invariant linear loop, and that for loop time constants less

than several seconds the near-optimum time-varying filter provides further improvements of 3 to 5 dB over the simple nonlinear loop.

4.1 Definition of the Problem

4.1.1 Navigation Problem

Phase coherent navigation systems transmit radio signals from two or more known geographic locations, where all of the system signals are at least phase stable with respect to each other and today are often synchronized to a universally accepted time-frequency scale through the use of atomic resonance oscillators. A receiver on a mobile platform receives a signal from each station which is given by

$$r(t) = y(t) + B(t) \sin \left(\omega_c t + \int_{-\infty}^t \langle \underline{x}(\tau), \underline{\nabla} \Theta \rangle d\tau + \text{Zero Reference Phase} \right),$$

where $y(t)$ is the additive atmospheric noise, the vector inner product yields a scaled platform velocity component perpendicular to lines of constant transmitted phase, and the "Zero Reference Phase" represents a reference geographic position in phase coordinates. The two types of signal formats currently in operational use are time multiplexed (LORAN) in which $B(t)$ is a bandlimited pulse waveform which each station transmits at a prescribed sequential time at the same carrier frequency, or frequency multiplex (DECCA, OMEGA) in which $B(t)$ is a constant for each station, which transmits at a different frequency. The engineering of a complete receiver system of a given type is a complex problem involving questions such as determination of the "Zero Reference Phase," acquisition, interference, noise reduction and the structure of an

optimum geographic position estimator from received phase estimates. We shall be concerned only with the problem of estimating the received phase from one station when the received carrier is corrupted by additive low frequency atmospheric noise.

4.1.2 Signal Generator Model

To model the dynamics of the received phase component perpendicular to lines of constant transmitted phase, we shall assume that this may be prepresented by a linear mapping from a vector Markov process as follows:

- a) Random phase process generator ($s(t)$ in radians)

$$\dot{\underline{s}}(t) = \underline{F} \underline{s}(t) + \underline{G} u(t), \quad E[u(t) u(t+\tau)] = Q\delta(t-\tau) \text{ radian}^2, \quad E[u(t)] = 0,$$

- b) Received phase,

$$s_1(t) = [1 \ 0 \ . \ . \ 0] \underline{s}(t) = \underline{H} \underline{s}, \quad \underline{H} \text{ volts/radian},$$

- c) Atmospheric noise process, $y(t)$,

$$E[y(t) y(t+\tau)] = R(t-\tau) \text{ volts}^2, \quad E[y(t)] = 0,$$

- d) Received carrier and signal-to-noise ratio,

$$B(t) \equiv 1, \quad \text{SNR} = \frac{1}{2} R$$

The matrices \underline{F} and \underline{G} can be chosen as a model of platform dynamics plus oscillator dynamics. We shall consider only sampled data systems in which the sampling interval, ΔT , is equal to or larger than the correlation time of the bandlimited atmospheric noise process, whence $R(t-\tau) = R\delta(t-\tau)$. As we noted in section 3.7, this is not a restrictive

assumption since all low frequency receivers must employ bandlimiting to remove adjacent channel interference. Thus the performance of continuous systems can be approximated by an equivalent sampled system with ΔT set equal to the noise correlation time. For the case of LORAN, a time multiplexed system, a sampled data model is an exact description of the receiver processing that must be employed. Using the state transition matrix of the continuous time signal model, $\Phi(t, t_0)$, the equivalent sampled data signal model is given by³⁶

$$\underline{s}(k+1) = \underline{\Phi}(\Delta T, 0) \underline{s}_k + \underline{I} \underline{u}(k) \quad (4.1)$$

$$E[\underline{u}(k) \underline{u}(k)^T] = Q \int_0^{\Delta T} \underline{\Phi}(\Delta T, \tau) \underline{G} \underline{G}^T \underline{\Phi}(\Delta T, \tau)^T d\tau \quad (4.2)$$

$$r(k+1) = \underline{H} \underline{s}(k+1) + y(k+1) \quad (4.3)$$

$$y(k) \leftarrow E[y(k) y(k+n)] = R \delta(k-n) = \frac{1}{2 \text{SNR}} \delta(k-n). \quad (4.4)$$

Specification of the continuous time signal process matrices \underline{F} and \underline{G} (assumed time-invariant) then determines the equivalent linear difference equations (4.1) for the sampled data model and the covariance matrix (4.2) of the driving random process. We note in equation (4.4) that we have parametrized the noise power in terms of received signal-to-noise power ratio, where the signal is the rf carrier, not the phase message process $s(t)$ which in general is nonstationary. This is the sampled signal-to-noise ratio that one would measure at the output of the antenna bandlimiting filter.

4.1.3 Signal Processing Structure

In considering signal processing structures, we shall assume that the error in the local estimate of the received phase message is small. Under this condition it is well known³⁸ that a phase-locked-loop (PLL) provides a statistically optimum estimate for the case of the corrupting noise being white and gaussian. Most important for our purposes is the fact that such a PLL in sampled data form can be directly interpreted, via state variables, as a Kalman-Bucy linear estimator which brings considerable insight and useful results to bear on our problem. The majority of the research into PLL performance has been directed towards analysis when the linearized assumption does not hold and problems such as acquisition, cycle slipping and threshold behavior become the dominant considerations. In the navigation context, however, these problems (except acquisition) are largely irrelevant because if cycle slipping has any significant probability of occurring the phase estimate becomes useless as a measure of position since one does not know which is the correct rf cycle, or the Zero Reference Phase, thus losing the measure of absolute position. Our linearized restriction is, in fact, the only case of practical interest in navigation receiver design. Our problem, for low frequency systems, is that the assumption of gaussian noise does not hold, as we have demonstrated in Chapters 1, 2, and 3, and we require design and analysis techniques to specify an improved or optimum signal processing structure for these atmospheric noise conditions.

For a sampled data system, the mixing operation of a PLL in which the local reference is multiplied by the received signal to generate the

lowpass phase error is performed by sampling the received signal at the zero crossing time of the local reference oscillator whose phase is the estimate. If our local phase estimate is given by $\hat{s}(t)$, the sampling times are defined by solutions of

$$\sin(\omega_c t + \hat{s}(t)) = 0 \rightarrow t = \frac{2(k+1)\pi - \hat{s}_1(k+1|k)}{\omega_c},$$

at which times the received signal samples are given by (using the small error assumption)

$$\begin{aligned} r(k+1) &= y(k+1) + \sin(2(k+1)\pi + s_1(k+1) - \hat{s}_1(k+1|k)) \\ &\approx y(k+1) + s_1(k+1) - \hat{s}_1(k+1|k) \end{aligned}$$

We note that this is also the sampled loop error and we introduce the following notational definitions:

- a) $\hat{s}(k+1|k)$; local estimate at $k+1$ using observations to k
- b) $\tilde{s}(k+1|k) = s_1(k+1) - \hat{s}_1(k+1|k)$; local estimate error at $k+1$ using observations to k
- c) $z(k+1) = y(k+1) + \tilde{s}(k+1|k)$, actual error signal at $k+1$ using observations to k
- d) $\tilde{s}(k+1|k+1)$, local error at $k+1$ using $k+1$ observations.

The design problem now is to determine the transformation from the sequence of loop error samples, $z(k+1)$ to the estimates $\hat{s}(k+1|k+1)$.

We know that if the noise sequence is uncorrelated, then the linear time-invariant minimum mean-square error estimator is given by the steady state Kalman-Bucy filter in which the error process is weighted and

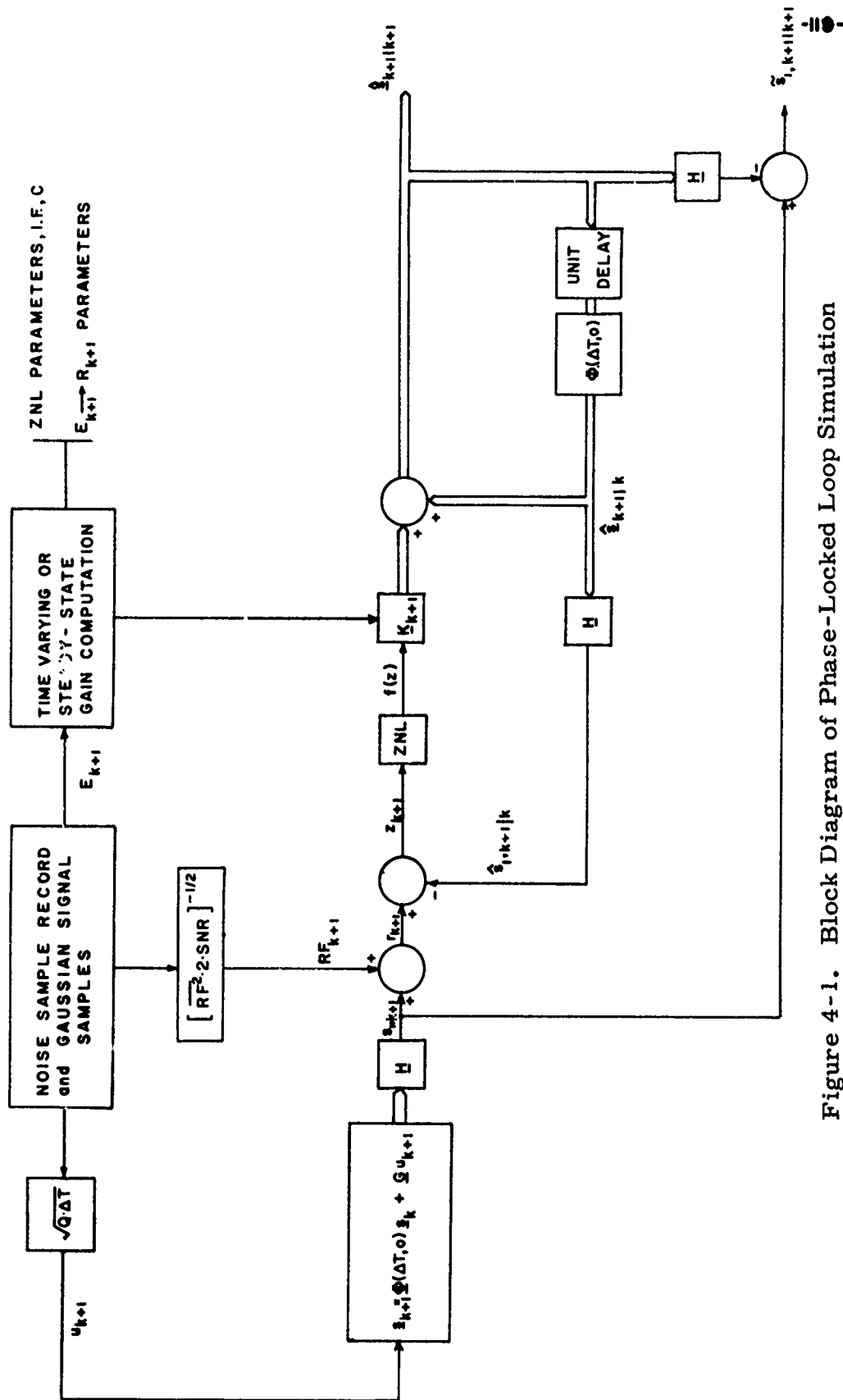
applied to a model of the signal generator as a correction. The signal generator model state then provides the updated local estimate $\hat{\underline{s}}(k+1|k+1)$, which in turn is mapped to the local estimate at the next sampling time. These relations are summarized in Figure 4-1, which includes details of the simulation to be discussed in sections 4.5 and 4.6 below.

We see in Figure 4-1 that the loop error process passes through a block labeled ZNL, Zero Memory Non-Linearity, and a possibly time-varying gain matrix $\underline{K}(k+1)$. In the following sections we shall consider the rationale for using the ZNL at this location and develop an approximate method of determining the complete estimator performance. The time-varying gain matrix \underline{K} will also be driven by a real-time computation of the matrix variance equation based on using the pilot channel envelope sample as an estimate of the time-varying power level of the noise sequence $y(k+1)$. This estimator structure provides a near optimum estimate in the minimum mean-square error sense (MMSE) without restriction as to estimator class.

4.2 Optimum Linear Time-Invariant Estimator

4.2.1 Kalman-Bucy Equations

The experimental observations of atmospheric noise waveforms reported in section 2.5.1 indicate that the noise process is uncorrelated beyond the correlation time of the bandlimiting filter. Samples of this process, with the sampling interval meeting this requirement, are similarly uncorrelated. Thus, with the specified signal process model and this observation, the MMSE linear filter is known to be the



Kalman-Bucy filter. For a gaussian noise process and our assumed signal model, the Kalman-Bucy (K-B) filter is the MMSE estimator of all possible types of filters. For our non-gaussian atmospheric noise process, the first-order amplitude statistics are non-gaussian and samples spaced beyond the filter correlation time are uncorrelated but not statistically independent (our model attempts to describe the power level correlation of such samples). Hence the K-B filter is, in our case, only an optimum filter of the linear class although it is easy to implement, requiring only the signal model and uncorrelated noise assumptions plus a measure of the power level of the atmospheric noise. Sections 4.3 and 4.4 to follow will attempt to exploit the two differences noted above for atmospheric noise to improve upon the linear filter, although we will find that design complexity increases accordingly.

The Kalman-Bucy filter equations are listed here to establish notational conventions.

a) Continuous Time Equations

i) Estimator

$$\dot{\hat{\underline{s}}}(t) = \underline{F} \hat{\underline{s}}(t) + \underline{K}(t)[r(t) - \underline{H} \hat{\underline{s}}(t)] \quad (4.5)$$

ii) Gain

$$\underline{K}(t) = \underline{\Sigma}(t) \underline{H}^T \underline{R}^{-1}(t) \quad (4.6)$$

iii) Error Covariance

$$\dot{\underline{\Sigma}}(t) = \underline{F} \underline{\Sigma}(t) + \underline{\Sigma}(t) \underline{F}^T - \underline{\Sigma}(t) \underline{H}^T \underline{R}^{-1}(t) \underline{H} \underline{\Sigma}(t) + \underline{G} \underline{Q} \underline{G}^T \quad (4.7)$$

iv) Steady State

$$\underline{K} = \underline{\Sigma}(\infty) \underline{H}^T \underline{R}^{-1} \quad (4.8)$$

where $\underline{\Sigma}(\infty)$ is a positive definite solution of

$$0 = \underline{F} \underline{\Sigma}(\infty) + \underline{\Sigma}(\infty) \underline{F}^T - \underline{\Sigma}(\infty) \underline{H}^T \underline{R}^{-1} \underline{H} \underline{\Sigma}(\infty) + \underline{G} \underline{Q} \underline{G} \quad (4.9)$$

b) Sampled Data Equations

i) Estimator

$$(\underline{\Phi} \triangleq \underline{\Phi}(\Delta T, 0)) \quad (4.10)$$

$$\hat{\underline{s}}(k+1 | k+1) = \underline{\Phi} \hat{\underline{s}}(k | k) + \underline{K}(k+1) [z(k+1)] \quad (4.11)$$

ii) Gain

$$\underline{K}(k+1) = \underline{\Sigma}(k+1 | k+1) \underline{H}^T \underline{R}^{-1}(k+1) \quad (4.12)$$

iii) Error Covariance

$$\underline{\Sigma}(k+1 | k) = \underline{\Phi} \underline{\Sigma}(k | k) \underline{\Phi}^T + \underline{G} \underline{Q}(\Delta T) \underline{G}^T \quad (4.13)$$

$$\underline{\Sigma}(k+1 | k+1) = \underline{\Sigma}(k+1 | k) - \underline{\Sigma}(k+1 | k) \underline{H}^T [\underline{R}(k+1) + \underline{H} \underline{\Sigma}(k+1 | k) \underline{H}^T]^{-1} \underline{H} \underline{\Sigma}(k+1 | k) \quad (4.14)$$

iv) Steady State

$$\underline{K} = \underline{\Sigma}(\infty) \underline{H}^T \underline{R}^{-1} \quad (4.15)$$

where $\underline{\Sigma}(\infty)$ is a positive definite solution of

$$\underline{\Sigma}(\infty)^{-1} = \underline{H}^T \underline{R}^{-1} \underline{H} + [\underline{\Phi} \underline{\Sigma}(\infty) \underline{\Phi}^T + \underline{G} \underline{Q}(\Delta T) \underline{G}^T]^{-1}$$

4.2.2 Sampled Data/Continuous Time Relations

We have included the continuous time equations above because it is often easier to solve these steady state equations than the sampled data equations. For reasonably dense sampling with respect to the estimator filter's impulse response there should, of course, be a correspondence between these two solutions. For the signal model, we have defined the sampled equations in terms of continuous time parameters and hence the correspondence is immediately established via \underline{F} , \underline{G} and \underline{Q} . For the white observation noise samples, we have a time series with a known variance, however, the variance of a continuous time white noise process is infinite. The difficulty is that the definition of a white noise process in terms of an impulse correlation function is only useful in terms of that function's action on an integral operator. Thus we must seek an equivalent white noise definition that results in the specified noise sequence variance when acting over the sampling interval ΔT . This can be done as follows:

$$y(t) \rightarrow E[y(t) y(t+\tau)] \triangleq R_{eq} \delta(\tau)$$

$$y(k) = \frac{1}{\Delta T} \int_0^{\Delta T} y(\tau) d\tau$$

$$\begin{aligned} E[y(k)^2] \triangleq R &= E \left[\frac{1}{\Delta T^2} \int_0^{\Delta T} y(\tau) d\tau \int_0^{\Delta T} y(\eta) d\eta \right] \\ &= \frac{1}{\Delta T^2} \int_0^{\Delta T} \int_0^{\Delta T} R_{eq} \delta(\tau-\eta) d\eta d\tau = \frac{R_{eq}}{\Delta T}, \end{aligned}$$

$$\therefore R_{eq} = \Delta T R.$$

(4.16)

This relation for the equivalent area of the continuous time white noise correlation function will be shown in section 4.6.1 to yield results that are accurate to better than 1% in predicting the steady-state behavior of sampled data equations from the continuous time steady-state solutions when ΔT is less than 1% of the estimator filter's time constant.

4.2.3 Relation to Classical Design Procedures

Classical design procedures for linear navigation PLL's³⁹ have generally been based on a specification of a Type I or Type II servo loop (single or double integrator, respectively) where the loop parameters have been chosen to meet a transient response specification. Noise performance has been evaluated via the noise power bandwidth of the resulting linear transfer function, assuming a white noise input. Our results, when a single or double integrator signal generator model is specified, can be related to this point of view by relating a given PLL bandwidth specification to an equivalent noise model. This relationship will be pointed out below when the two signal models are specified. The principal advantage of our approach is that we bring to bear on the problem many useful results and insights from modern communication theory and, at the same time, prescribe an unambiguous method of testing the performance of different receiver structures. This becomes important when we consider nonlinear or time-varying PLL's where there is no general relationship between a deterministic signal response, such as an impulse response, and the performance of the loop when stimulated by signal plus noise. Our testing procedure will consist of measuring the error of various PLL structures in tracking a simulated stochastic

signal in the presence of the recorded atmospheric noise sample sequences. In a classical context this parallels the technique⁴² of measuring the small signal loop bandwidth by adding a deterministic wide-band signal to a noise sequence and then estimating the signal content at the loop output through correlation techniques, such as Fourier analysis.

If one accepts the model assumption that the combined effects of platform movement and oscillator dynamics can be described as a random process (paralleling the classical requirement that the PLL have a nonzero signal bandwidth) then our approach provides an objective method of comparing the performance of various structures, specifying an optimum performance, and testing these theoretical results.

4.3 Time-Invariant Nonlinear Estimator

4.3.1 Definition of Nonlinear Filter Class

In Figure 4-1 we indicated the general type of time-invariant nonlinear filter that we shall consider; the use of a Zero Memory Non-Linearity (ZNL) in the path of the loop error signal followed by a time-invariant linear filter to generate the estimate. The selection of this filter class can be qualitatively justified by considering the basic signal processing problem. The phase message is a slowly varying process, as determined by platform and oscillator dynamics, whereas the noise is uncorrelated over milliseconds and statistically independent over seconds. Thus we expect that any filter matched to the signal will have a similarly long time constant and it would be desirable to limit in some way the large amplitude excursions of the noise prior to being weighted

by the long filter time constant. Since by assumption $\tilde{s}(k+1|k)$ is small, the loop error is principally composed of the noise component and it would seem logical to perform the nonlinear amplitude limiting at that point, which is the ZNL location of Figure 4-1. A ZNL followed by a linear filter with memory is Zadeh's class (η_1) nonlinear filter and is often used⁵² as a first approximation to a general nonlinear filter. In section 4.3.5 we shall give a qualitative argument that the limiting form of the optimum ZNL in our filter provides an optimum estimate in the maximum likelihood sense and our experimental results will bear this out. However, in the following sections we shall be concerned with analysis and optimization of this filter class which we have specified on an intuitive basis.

4.3.2 Linearized Analysis

To analyze the approximate ZNL class filter performance, we replace the ZNL, defined by $f(z)$, by a gain normalized ZNL, $f(z)/c$, where c is chosen as

$$c \triangleq \frac{\overline{\tilde{s}(k+1|k) f(z(k+1))}}{\overline{\tilde{s}(k+1|k)^2}}. \quad (4.17)$$

This choice allows us to define a new noise component at the output of $f(z(k+1))$, as

$$n(k+1) \triangleq \frac{1}{c} f(z(k+1)) - \tilde{s}(k+1|k) \quad (4.18)$$

which is orthogonal to the signal, $\tilde{s}(k+1|k)$,

$$\overline{\tilde{s} \left[\frac{1}{c} f(z) - \tilde{s} \right]} = \frac{\overline{\tilde{s} f(z)}}{\overline{\tilde{s} f(z)}} - \overline{\tilde{s}^2} = 0.$$

The gain, c , is Booton's equivalent gain⁴¹ and the retention of the distortion as a noise term is an extension of Booton's method due to Caron.⁴¹ This type of linearized analysis of a given nonlinear control system appears to be the most practical technique available^{41, 54} and has been used by several workers in analyzing PLL's operating in gaussian noise.^{45, 53}

Recalling our assumption that $\tilde{s}(k+1|k)$ is small relative to the noise power, R , a further assumption that we will make is that the noise sequence at the output of the ZNL is uncorrelated, $\overline{n(k) n(i)} = 0$, $k \neq i$. This assumption requires that the uncorrelated atmospheric noise sequence, $y(k)$, dominates the error sequence, $\tilde{s}(k)$, and that the resulting ZNL output noise sequence $n(k)$ does not couple significantly back to the ZNL input. This assumption is equivalent to the qualitative conditions listed by Smith⁴¹ as to when linearization of the nonlinear element can be used, such as requiring the bandwidth of the ZNL input to be significantly larger than the following linear filter. If this assumption is valid, then we can optimize any ZNL type filter by using the K-B equations with a new noise power $n(k)^2$ replacing the input noise power R . Further, we can specify the optimum filter of this class by choosing the ZNL to minimize the noise power $n(k)^2$. The filter, optimized for a given ZNL, can then be used to check the $n(k)$ uncorrelated assumption by comparing the ratio of resulting steady-state estimation error (the

signal input to the ZNL, \tilde{s}) with the atmospheric noise input to the ZNL. Our results, both theoretical and those derived from tests, indicate that the $n(k)$ uncorrelated assumption is acceptable for most problems of practical interest.

If we define a signal-to-noise ratio improvement factor

$$I.F. \triangleq SNR_{ZNL\ OUT}/SNR_{ZNL\ IN},$$

then using the definition of a gain normalized ZNL and (4.17) and (4.18) we have

$$I.F. = \left[\frac{R}{\tilde{s}^2} \right] \cdot \left[\frac{\overline{\tilde{s} f(z)}^2}{\tilde{s}^2 \cdot \overline{f^2(z)} - \overline{\tilde{s} f(z)}^2} \right]. \quad (4.19)$$

If the assumption that $n(k+1)$ is an uncorrelated time series is valid, then the relations between the I.F. and the performance of a system of our class, optimized in a specified ZNL, is given functionally as

$$I.F. = g(R, \tilde{s}^2 \approx \Sigma_{11}(\infty), p_z(z)) \quad (4.20)$$

$$\Sigma_{11}(\infty) = h(R/I.F., \text{Signal Model}), \quad (4.21)$$

where (4.20) depends upon the first-order pdf of $z(k+1)$ and $\Sigma_{11}(\infty)$ is the K-B steady-state solution (4.15) using a new effective noise power, $R/I.F.$ Thus, to determine the performance of the given estimator class we can study the I.F. (4.19) for various types of ZNL's and predict the resulting performance with a simultaneous solution of (4.20) and (4.21).

If we assume the signal generator model to be controllable and observable, then the steady-state solution (4.21) will exist and it will be a monotone function of the effective noise power $R/I.F.$ ³⁶ The minimum mean-square error of the nonlinear class we have specified $(\Sigma(\infty))_{\min}$ will then be provided by the ZNL which maximizes the Improvement Factor. Hause⁴⁰ has shown that the I.F. is maximized, at a given R/\bar{s}^2 , by the conditional expectation ZNL which provides the MMSE estimate of $\tilde{s}(k+1|k)$ given $z(k+1)$ and is defined by

$$f(z) = \int_{-\infty}^{+\infty} \eta p_{\tilde{s}|z}(\eta, z) d\eta.$$

We can study the I.F. of various ZNL's versus R/\bar{s}^2 and compare them to the optimum MMSE ZNL as a measure of relative ZNL quality. If the $n(k+1)$ uncorrelated assumption is valid, we can also determine the simultaneous solution of (4.20) and (4.21) for a specific signal generator model from the evaluation of I.F. The resulting operating point solution will then provide an indication of the validity of the assumption in terms of the ratio R/\bar{s}^2 .

4.3.3 ZNL Improvement Factor

To study the ZNL I.F. for a given R/\bar{s}^2 ratio, we must evaluate (4.19) which, in terms of the first-order pdf's is given by

$$I.F. = \left[\frac{R}{\bar{s}^2} \right] \cdot \left[\frac{(E[E[\tilde{s} f(z) | \tilde{s}]_z])^2}{\bar{s}^2 E[E[f^2(z) | \tilde{s}]_z] - (\text{Numerator})} \right]$$

$$= \left[\frac{R}{\tilde{s}^2} \right] \cdot \left[\frac{\left[\int_{\tilde{s}} p_{\tilde{s}}(\xi) \int_z \xi p_y(\eta-\xi) f(\eta) d\eta d\xi \right]^2}{\tilde{s}^2 \int_{\tilde{s}} p_{\tilde{s}}(\xi) \int_z f^2(\eta) p_y(\eta-\xi) d\eta d\xi - [\text{Numerator}]} \right],$$

where $E[\cdot]_x$ is a conditional expectation wrt, x . Interchanging the order of integration yields

$$\text{I. F.} = \left[\frac{R}{\tilde{s}^2} \right] \cdot \left[\frac{\left[\int_z f(\eta) \int_{\tilde{s}} \xi p_y(\eta-\xi) p_{\tilde{s}}(\xi) d\xi d\eta \right]^2}{\tilde{s}^2 \int_z f^2(\eta) \int_{\tilde{s}} p_{\tilde{s}}(\xi) p_y(\eta-\xi) d\xi d\eta - (\text{Numerator})} \right].$$

In this expression $p_y(\cdot)$ is the atmospheric noise pdf and $p_{\tilde{s}}(\cdot)$ is the estimation error pdf. To proceed further we must know the latter pdf which is formally related to the estimator structure and non-gaussian observation noise by the Chapman-Kolmogorov functional equations. We shall assume that this pdf can be approximated by a zero-mean gaussian distribution, an assumption that is consistent with previous assumptions concerning the fact that $\tilde{s}(k+1|k)$ is small, the estimator time constant is long and that the ZNL will attenuate the large amplitude excursions of the atmospheric noise so that no single noise sample will dominate the weighted sum within the time constant window.

We now observe that the interior integration in the left term of the denominator is a convolution that defines $p_z(\cdot)$ and that the interior integration of the numerator is proportional to the derivative of a gaussian pdf convolved with the noise pdf. Interchanging these latter two linear operations yields

$$\begin{aligned} \int_{\tilde{s}} \xi p_y(\eta-\xi) p_{\tilde{s}}(\xi) d\xi &= -\tilde{s}^2 \frac{d}{d\eta} \int_{\tilde{s}} p_y(\eta-\xi) p_{\tilde{s}}(\xi) d\xi \\ &= -\tilde{s}^2 \frac{d}{d\eta} p_z(\eta). \end{aligned}$$

Thus the right-hand term of I. F., the ZNL SNR, becomes

$$\text{SNR}_{\text{ZNL}} = \frac{[\int_z f(\eta) p'_z(\eta) d\eta]^2}{\frac{1}{\tilde{s}^2} \int_z f^2(\eta) p_z(\eta) d\eta - [\int_z f(\eta) p'_z(\eta) d\eta]^2}, \quad (4.22)$$

where $p'_z(\eta)$ represents the derivative of $p_z(\cdot)$ wrt its argument.

The ZNL SNR, (4.22), is maximized by the ZNL which generates the conditional expectation of \tilde{s} , which is

$$\begin{aligned} f(z)_{\text{MMSE}} &= \int_{\tilde{s}} \eta p_{s|z}(\eta, z) d\eta = \int_{\tilde{s}} \frac{\eta p_{z|\tilde{s}}(z, \eta) p_{\tilde{s}}(\eta)}{p_z(z)} d\eta \\ &= \frac{\int_{\tilde{s}} \eta p_y(z-\eta) p_{\tilde{s}}(\eta) d\eta}{p_z(z)}. \end{aligned}$$

Using the gaussian assumption for $p_{\tilde{s}}(\eta)$ as above, this reduces to

$$f(z)_{\text{MMSE}} = -\tilde{s}^2 \frac{p'_z(z)}{p_z(z)}, \quad p_z(z) = p_y(\xi) \otimes p_{\tilde{s}}(\xi). \quad (4.23)$$

It can be shown using calculus of variations that (4.23) does maximize (4.22).

Recalling the definition of the atmospheric noise pdf (3.5) we see that $p_z(\cdot)$ is given by

$$\begin{aligned}
 p_z(z) &= N(0, \bar{s}^2) \otimes \left[q_x N(0, \sigma_{nG}^2) + p_x N(0, \sigma_{nG}^2) \otimes p_{yH}(\eta) \right] \\
 &= q_x N(0, \sigma_{nG}^2 + \bar{s}^2) + p_x N(0, \sigma_{nG}^2 + \bar{s}^2) \otimes p_{yH}(\eta). \quad (4.24)
 \end{aligned}$$

For small values of z , the low amplitude gaussian component of (4.24) will dominate the pdf and $f(z)_{\text{MMSE}}$ from (4.23) will be a straight line passing through the origin, the optimum ZNL estimator for gaussian signal and noise. For large amplitude values of z , the hyperbolic component of $p_{yH}(z)$ will dominate and (4.23) will yield a function behavior

$$\frac{-\bar{s}^2}{p_z(z)} \frac{p'_z(z)}{p_z(z)} \propto \frac{-\bar{s}^2}{\bar{s}^2} \cdot \frac{\frac{d}{dz} \frac{1}{z^m}}{\frac{1}{z^m}} = \frac{m \bar{s}^2}{z}. \quad (4.25)$$

Thus the MMSE ZNL has a small signal linear portion, reaches a point of maximum value and decays hyperbolically for large z , irrespective of the integer m value of the atmospheric noise tail. We have evaluated (4.24) numerically and find that this general behavior is followed, although the nature and position of the peak value is strongly dependent upon the atmospheric noise weather conditions and resulting pdf. We shall not consider $f(z)_{\text{MMSE}}$ as a viable candidate ZNL to use in a practical estimator since one has to know a great deal about the specific noise pdf. We shall use the SNR_{MAX} produced by $f(z)_{\text{MMSE}}$ as a comparison for practical ZNL's to be discussed below.

4.3.4 Improvement Factor of Four Types of ZNL's in Atmospheric Noise

A practical ZNL should have two attributes, achieve near optimum performance, and have parameters that are not critically sensitive to

specific noise characteristics, or that can be adjusted in a noncritical manner. The first and most obvious candidate ZNL is a hard limiter, defined by

$$f(z) = \begin{cases} 1 & z \geq 0 \\ -1 & z < 0. \end{cases} \quad (4.2)$$

The hard limiter in this position in a sampled data PLL can be simply realized by hard limiting the received rf signal at the output of the antenna bandlimiting filter and sampling the resulting two-state waveform at the time of the reference carrier (VCO output) zero crossing. This is not exactly the same type of system that one obtains by hard limiting both received signal and carrier (often termed bandpass limiting), multiplying and then processing the resulting waveform with a lowpass loop filter.⁴⁵ One continuous time dual of the hard limiter that we are considering is the use of the limiter, after lowpass filtering to recover the baseband phase error signal, i. e., a bang-bang control system application. The hard limiter ZNL does not have a parameter explicitly associated with its transfer function, however, one must know the value of c , (4.17), the signal suppression of the limiter, so that the optimum loop gain, K/c , can be specified for optimum performance for a given signal model and noise condition.

Two other types of ZNL's that have been proposed in the literature are clipping and hole-punching, defined by

$$f(z)_{\text{clip}} = \begin{cases} z, & |z| \leq Z_t \\ Z_t, & z \geq Z_t \\ -Z_t, & z \leq -Z_t \end{cases}, \quad f(z)_{\text{hp}} = \begin{cases} z, & |z| \leq Z_t \\ 0, & |z| > Z_t. \end{cases} \quad (4.27)$$

These two ZNL's are shown in Figure 4-2, along with the limiter and the qualitative behavior of the MMSE ZNL as numerically evaluated from (4.23). The clipping and hole-punching ZNL's have a single threshold parameter to define their transfer function, and we must either carry this as an additional parameter in the analysis or specify them as a function of the noise characteristics. We have adopted the latter and used a suggestion by Feldman⁴² that the threshold be set so that a fixed percentage of the samples, $z(k+1)$, fall in the nonlinear region. This behavior can be easily controlled by a long-time constant digital servo loop that simply counts samples exceeding the threshold and then adjusts the threshold in the correct direction at the end of each averaging period. Thus the technique is not dependent upon a specific knowledge of noise conditions; however, we must evaluate the I.F. for various noise conditions to determine if the performance using this technique is insensitive to noise conditions.

Substitution of (4.23) into (4.22) yields the maximum I.F. for a given noise pdf,

$$(I.F.)_{\max} = \frac{R}{\tilde{s}^2} \cdot \frac{1}{\frac{1}{\tilde{s}^2} \int_z \frac{(p'_z(\eta))^2}{p_z(z)} dz - 1} \quad (4.28)$$

Substitution of the hard limiter characteristic results in a simple expression for the I.F.

$$I.F._{h.l.} = \frac{R}{\tilde{s}^2} \cdot \frac{1}{\frac{1}{\tilde{s}^2} \frac{1}{4p_z^2(0)} - 1} \quad (4.29)$$

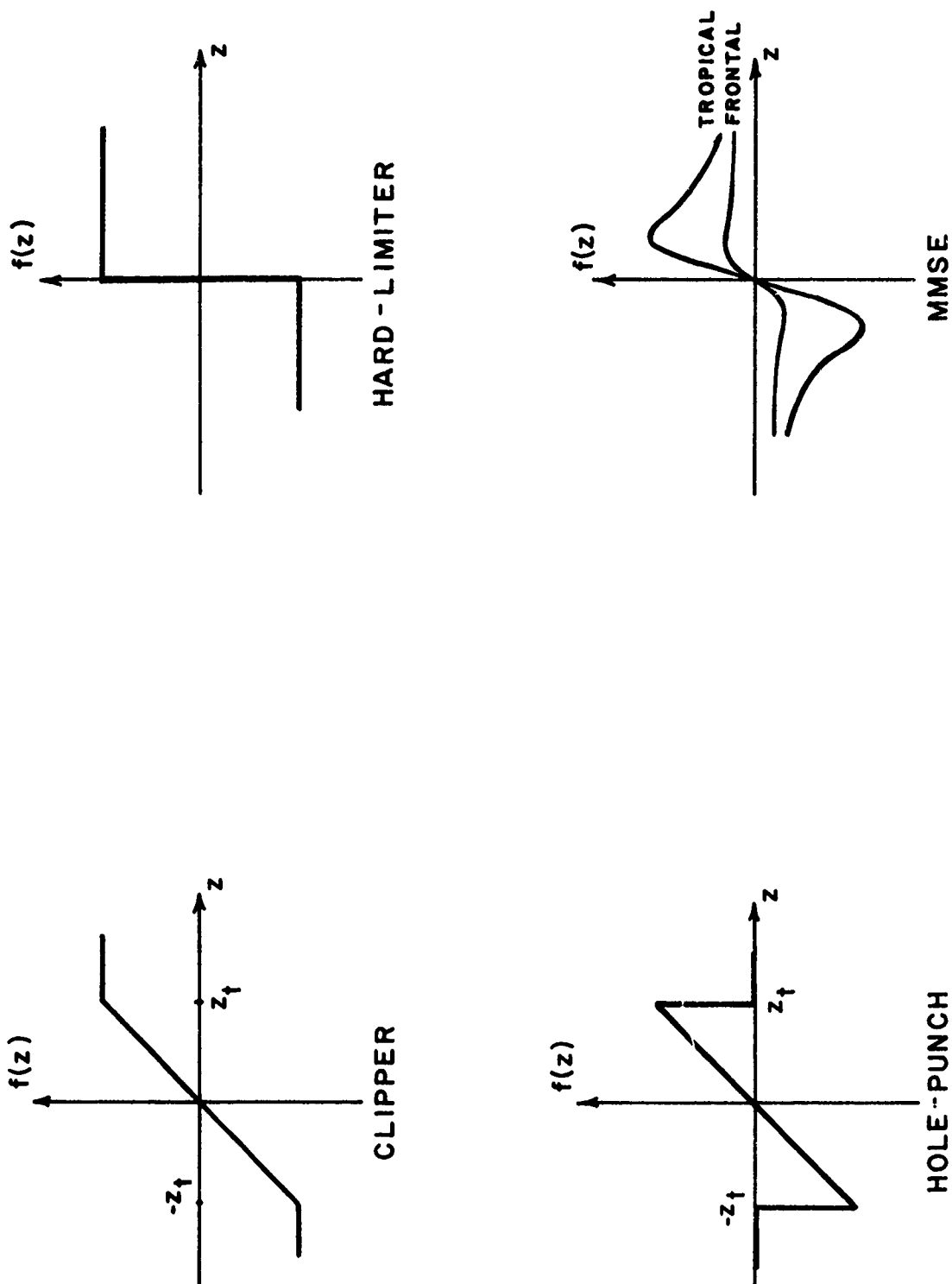


Figure 4-2. Various ZNL Transfer Functions

These I.F.'s, including the clipper and hole-puncher, were numerically evaluated for all four atmospheric noise conditions of Chapters 2 and 3, and for gaussian noise. The results are shown in Fig. 4-3 through 4-5 representative Z_t percentages and the hard limiting and optimum cases.*

Inspection of these results suggests the following comments:

- a) The ZNL I.F. plots show only a 15% clip percentage. Performance was evaluated at 5% increments from 5% to 50% and this percentage was selected as providing the best I.F. over the widest possible range of conditions. We note that the 15% clipper provides near optimum performance over the widest range of R/\bar{s}^2 value of any practical ZNL. It is thus insensitive to both the range of input signal-to-noise as well as being relatively insensitive to the type of atmospheric noise.
- b) Hole punching is clearly more sensitive than clipping to both the type of atmospheric noise and the R/\bar{s}^2 ratio. While it is possible to select a good hole punch percentage for a specified operating point, significant changes in conditions will render this selection a poor one. Similar results for hole punching have been reported by Kapp¹⁹ and Griffiths⁵¹ for the signal detection problem. They plotted a measure of detection performance against a single noise parameter and found hole punching exhibited a much sharper performance peak than clipping (they did not use our percentage-threshold technique).
- c) Hard limiting performs quite well for most regions of low R/\bar{s}^2

* Notes: The straight lines on these plots are the functions (4.21) for two signal models to be given in section 4.5; $\sqrt{R/\bar{s}^2} \approx [\Sigma_{11}/R]^{-1/2}$.

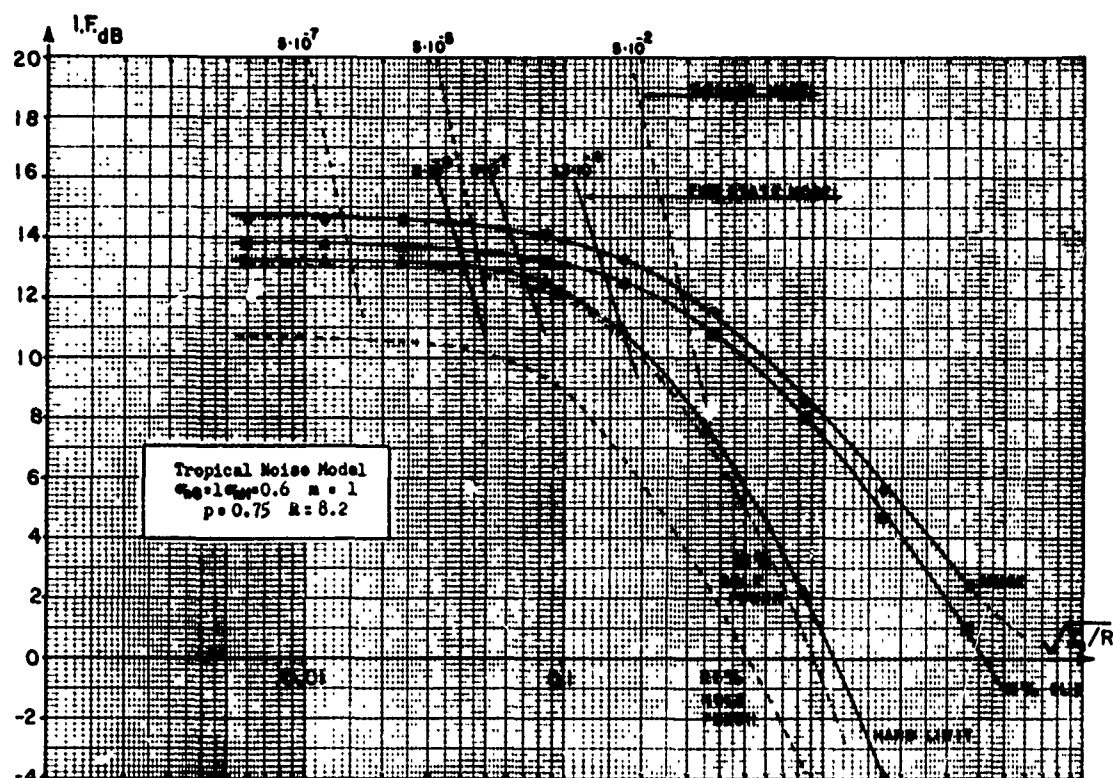
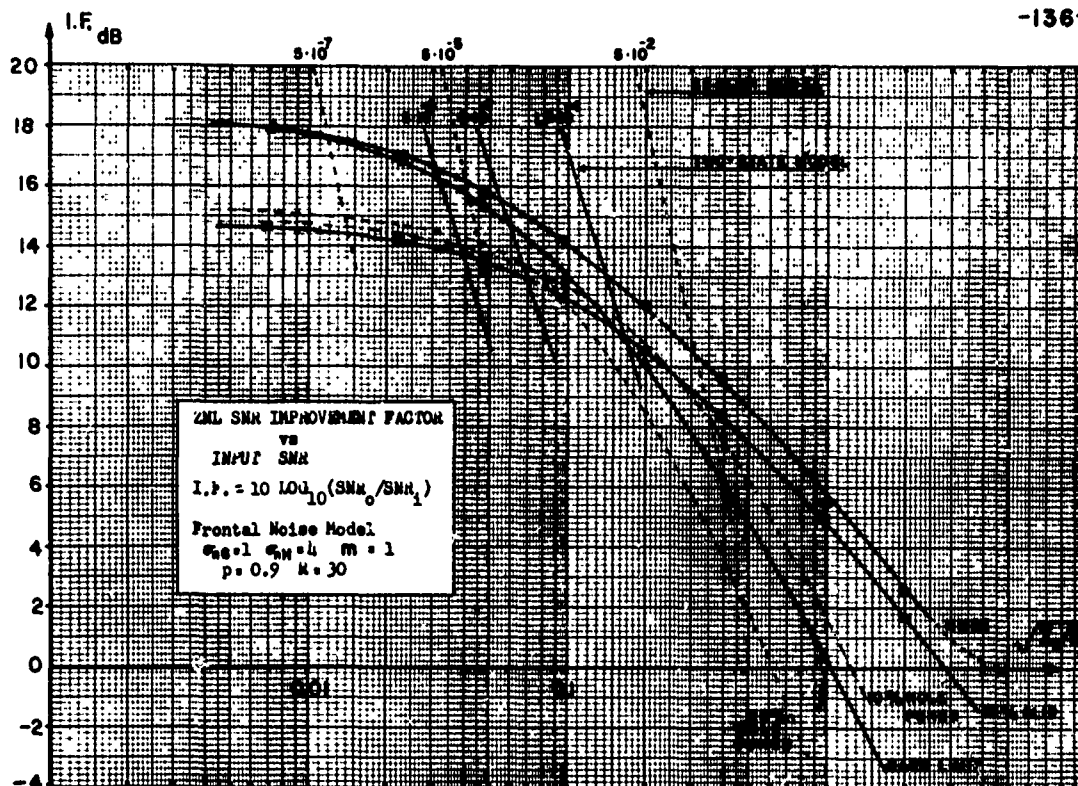


Figure 4-3. ZNL Improvement Factor for Frontal and Tropical Noise Conditions

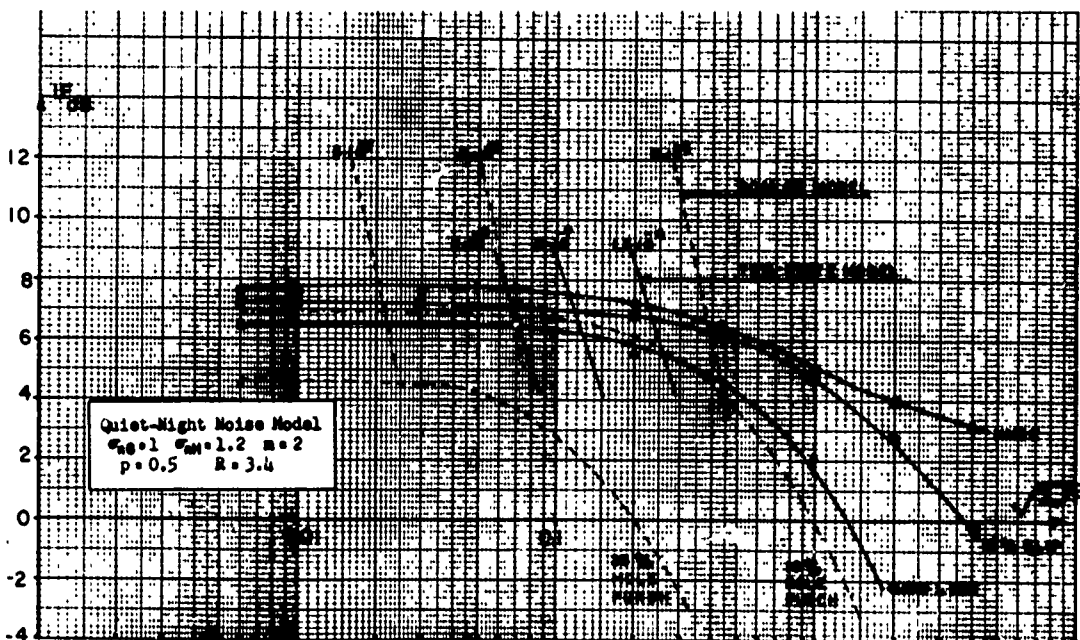
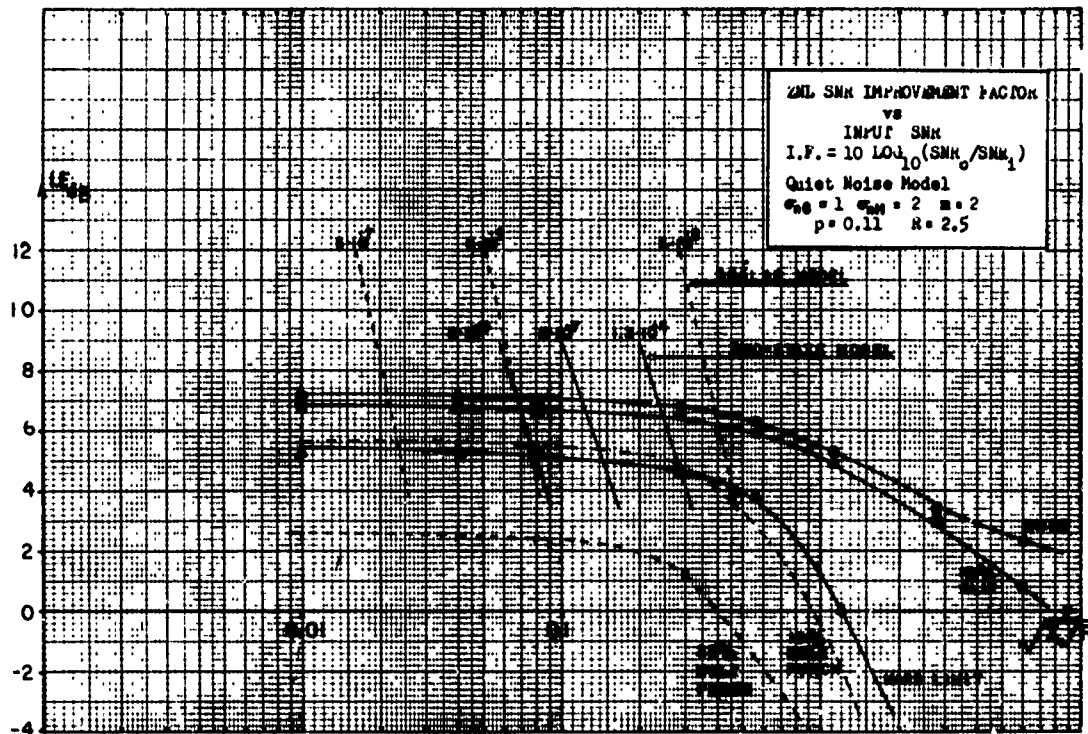


Figure 4-4. ZNL Improvement Factor for Quiet and Quiet-Night Noise Conditions

ratio where we expect operating solutions of the estimator structure to validate the $n(k)$ uncorrelated assumption. In regions where the hard limiter performance decreases rapidly, this uncorrelated assumption will also break down since the correlated signal, \tilde{s} , will cause a significant portion of the hard limiter distortion (noise $n(k)$). This will in general make the actual performance less than predicted by the combination of the I.F. curves and K-B equations which assume that $n(k)$ is uncorrelated.

- d) Figure 4-5 also shows the variation of c (4.17), with noise condition, for hard limiting and 15% clipping. Following the development of 4.3.3 it can be shown that this parameter is given by

$$c = -\int_{-\infty}^{\infty} f(\eta) p'_z(\eta) d\eta, \quad c_{h.l.} = 2p_2(0) \quad (4.30)$$

which, as noted, is Booton's equivalent gain.

Since the hole punching ZNL has distinct performance disadvantages compared to the clipper and is only marginally easier to implement, we have not considered it further in this research. In sections 4.5 and 4.6 the ZNL performance analysis developed here will be combined with a scalar and two-state signal model to analyze ZNL estimator performance. The predicted performance, based on the linearized analysis given here will be found to agree well with tests using noise sample records and a simulated signal process.

4.3.5 Optimality of ZNL Estimator Class

The ZNL I.F. curves given above share a common characteristic in that for decreasing \tilde{s}^2/R ratio they approach a constant value for any

-140-

ZNL characteristic. This value is determined by $\lim_{\tilde{s}^2 \rightarrow 0} p_z(z) = p_y(z)$.

For the MMSE ZNL we see that this results in

$$f(z)_{\text{MMSE}} = -\tilde{s}^2 \frac{p'_z(z)}{p_z(z)} \rightarrow -\tilde{s}^2 \frac{p'_y(z)}{p_y(z)} = -\tilde{s}^2 \frac{d}{dz} \ln [p_y(z)]. \quad (4.31)$$

Several workers^{43, 44, 50} have shown that this ZNL (4.31), followed by a matched filter, is the asymptotically optimum, weak signal detector, for known signals in non-gaussian noise where noise samples are statistically independent. It can be shown, combining Van Trees'³⁷ development of a maximum likelihood estimate of a discrete parameter, \tilde{s} , with Antonov's⁴⁴ technique for a Taylor series expansion of the likelihood ratio, that an asymptotic optimum estimate of a parameter \tilde{s} is given by the ZNL of (4.31) followed by an averaging function. Furthermore, the large amplitude form of the noise pdf (3.14a) satisfies Capon's condition⁵⁵

$$0 < \int_{-\infty}^{+\infty} (p'_y(\eta))^2 / p_y(\eta) d\eta < \infty,$$

to ensure that the resulting estimate $\hat{\tilde{s}}$ tends to gaussianity. We can argue that our assumed ZNL estimator structure, feeding back the estimate of $\hat{s}(k+1|k)$ to maintain \tilde{s} small, should provide an optimum estimator structure for a long observation time where we can "open" the feedback loop and consider the estimation of $\hat{s}(k+1)$ to be a sequence of discrete parameter estimation problems. We have not obtained a formal proof that the optimum ZNL class filter is asymptotically equivalent to an unstructured optimum due to the difficulty of including a model for

the signal dynamics within the loop. However, we shall find that the near optimum estimate obtained with the use of the pilot channel information and the time-varying gaussian noise model never improves upon the error performance predicted for MMSE ZNL. We suspect that the MMSE ZNL estimator provides the optimum estimate of all filters when sufficiently dense sampling is employed and the noise samples are statistically independent. For the case of non-independent samples, as is found in several atmospheric noise conditions, the optimum performance will be less than the MMSE ZNL estimator.

4.4 Linear Time-Varying Estimator

4.4.1 Use of Joint Channel Noise Model

We demonstrated in Chapters 2 and 3 that a useful model for a band-limited atmospheric noise waveform is a time-varying gaussian process. It is well known^{36, 37} that the general time-varying Kaman-Bucy filter provides the MMSE estimate of a rational spectrum signal process additively combined with a time-varying gaussian noise process where

$$E[y(t) y(t+\tau)] = R(t) \delta(t-\tau).$$

The experimental sample records on which we have based our noise model utilized the pilot channel envelope as a measure of the rf noise variance. Equation (3.23) gave the conditional estimate of the noise power, conditioned by the pilot channel envelope value v_o , as

$$\sigma_y^2 | v_o, x=1 = \frac{1}{m} \frac{\sigma_{nH}^2}{\sigma_{vH}^2} \left[v_o^2 + m \sigma_{vH}^2 \right], \quad (3.23) \text{ repeated}$$

for noise excursions above the background gaussian noise process. To utilize the pilot channel envelope as a measure of the time-varying rf noise power we shall implement the following algorithm:

$$R(k) = \sigma_{y_k}^2 | v_{o_k} = \begin{cases} \sigma_{nG}^2, & v_{o_k} < v_t \\ \frac{1}{m} \begin{bmatrix} \sigma_{nH}^2 & \sigma_{vH}^2 \end{bmatrix} \begin{bmatrix} v_o^2 \end{bmatrix}, & v_{o_k} > v_t \end{cases} \quad (4.32)$$

The threshold value of the envelope, v_t , was selected as the intersection of the relation (3.23) with the σ_{nG} value as seen on the model-data comparison Figures 3-1, 3-2. Therefore, $v_t^2 = m \sigma_{nG}^2 \sigma_{vH}^2 \sigma_{nH}^2$.

Both the joint channel model and the experimental observations show that the pdf of the rf noise samples, $y(k)$, is not gaussian when conditioned on the pilot channel envelope even though the model utilizes a noise process in each channel which is gaussian when conditioned on the frequency independent random variable "a". If the model were an exact description of the joint channel noise relations, one could use a better estimator of $\sigma_{y|v_o}^2$ than provided by the pilot channel envelope. However, the envelope was used, based on empirical evidence that it provided the highest correlation coefficient with $|RF|_k$ and hence we must adapt our use of the joint channel model and time-varying filter to our experimental records. To consider the effect of the non-gaussian pdf of $y|v_o$ we evaluated the MMSE ZNL Improvement Factor, as described in section 4.3, for the conditional distribution (3.11) with $m = 1$ and found that a 1.35 dB improvement was possible in estimating \tilde{s} given z . To reflect this possible improvement in an ad hoc manner in the time-varying estimator,

we utilized a clipper ZNL with threshold set, at each iteration, to plus and minus three sigma of the sum of the estimate error and noise for that iteration. This algorithm will be given in sections 4.5 and 4.6 when we consider the actual simulations. Thus the algorithm that we shall use to specify the time-varying power level of the atmospheric noise sample sequence will not result in a precisely MMSE estimate of the signal process since the conditional noise distribution is not gaussian. The above computation and the ad hoc correction scheme should result in performance that is within 1 dB of optimum.

4.4.2 Performance of the Time-Varying Linear Estimator

The qualitative effect of the time-varying power level on the estimator can be understood by referring to the K-B sampled data equations (4.12), and (4.13) and (4.14). The time-varying gain, $K(k+1)$, responds to each $R(k+1)$ value in an inverse manner, thus attenuating samples, $z(k+1)$, that are caused by large noise excursions beyond the background noise level. To the extent that we can associate an expected magnitude with the $R(k+1)$ estimate, $|z(k+1)| = a \cdot R(k+1)^{1/2}$, we see that the $R^{-1}(k+1)$ portion of (4.12) provides a transfer relation quite similar to the MMSE ZNL (4.25); it is linear for $R(k+1) < v_t$ and decays hyperbolically beyond this point.

The second time-varying term of (4.12) introduces a dynamic behavior into the attenuator. This term, $\Sigma(k+1|k+1)$ reflects the growth in uncertainty of the signal state at each iteration (4.13) and the decrease in uncertainty caused by optimal weighted observations (4.14). When a significant number of sequential observations are heavily contaminated

by noise, the growth of $\Sigma(k+1|k+1)$ will increase the weighting of subsequent samples that have a small noise contamination. This increase will be above the quiescent value caused by $R_{\min}(k+1) = \sigma_{nG}^2$ and will be a stochastic manifestation of the well-known fact³⁶ that a K-B filter has a step response that is "faster" than a time-invariant filter equal to the steady-state K-B filter.

Applying this description to our atmospheric noise model we see that for quiet conditions where there is no significant multiple discharge activity and the noise samples are statistically independent beyond several milliseconds, the time-varying estimator should have a performance quite similar to the ZNL estimators. For heavier noise conditions such as tropical and frontal, where the samples are not statistically independent due to the multiple discharge activity, we would expect that the time-varying filter's optimal compensation for this via $\Sigma(k+1|k+1)$ should result in improved performance over the ZNL estimator.

To predict the performance of the time-varying filter we must determine the average value of $\Sigma(k+1|k+1)$. From (4.13) and (4.14) we see that this requires that we determine the first-order output statistics of a nonlinear difference equation driven by a non-gaussian, colored process, $R(k)$, as defined by (4.31). There are no practical solution techniques for this problem short of linearization of the equation and approximation of the driving process with a gaussian process. Since the actual driving process is very non-gaussian, this latter step would seem to make the approximation of questionable value. The one practical answer that can be obtained is to place an optimistic lower bound on the error variance by considering the steady-state error for a K-B

-145-

filter with constant noise power $R_{\min} = \sigma_{nG}^2$, i.e., ignoring the effect of all the non-gaussian excursions. Thus

$$\Sigma_{T.V.}(\infty) \geq \Sigma_{RMIN}(\infty).$$

In the two simulation examples that we have explored, a tighter bound is found to be given by the predicted MMSE ZNL estimator error. If this ZNL filter does provide an asymptotic optimum estimator for statistically independent noise and long observation times (dense sampling wrt filter time constant) as we suspect, then it follows that shorter observation intervals and statistically dependent noise, though processed in an optimal manner by a time-varying filter, cannot result in better performance than the asymptotic optimum.

4.5 Test of Estimators for Scalar Signal Model

4.5.1 Operating Equations

The first signal model we shall consider is a scalar case with $F=0$, which is a single integrator. This model is useful for certain navigation applications where the mobile platform uses a precision reference oscillator and the single integration of the white gaussian driving process represents phase instabilities in the transmitting and receiving oscillator³⁸ and a random velocity description of the mobile platform movements. The sampled data description of the signal generator is seen to be (equations (4.1)-(4.4))

$$\Phi(\Delta T, 0) = 1, \quad E[u(k) u(k)^T] = Q\Delta T.$$

The sampled data estimator equations can be solved directly for steady-

state to yield

$$\Sigma_{11}(\infty) = - \frac{Q\Delta T + \sqrt{(Q\Delta T)^2 + 4RQ\Delta T}}{2}$$

$$\approx \sqrt{RQ\Delta T}, \quad R \gg Q\Delta T \quad (4.33)$$

$$K \approx \sqrt{\frac{Q\Delta T}{R}}$$

$$\hat{s}(k+1|k+1) = \left[1 - \sqrt{\frac{Q\Delta T}{R}} \right] \hat{s}(k|k) + \sqrt{\frac{Q\Delta T}{R}} r(k+1), \quad R \gg Q\Delta T.$$

$$(4.34)$$

The estimator is thus a filter with a sampled exponential impulse response.

To relate our model to classical design techniques (section 4.2.3) one would specify a noise power level and filter time constant, $N_f \Delta T$, and determine the required signal model driving process variance, $Q\Delta T$, from

$$\left[1 - \sqrt{\frac{Q\Delta T}{R}} \right]^{N_f} = .37, \quad Q\Delta T = R[1 - .37^{1/N_f}]^2.$$

To determine the steady-state estimate error of the ZNL estimator we utilize (4.32), the definition of the Improvement Factor and R to obtain

$$\Sigma_{11} = \sqrt{\frac{RQ\Delta T}{\text{I.F.}}}, \quad \text{I.F.} = \frac{RQ\Delta T}{\Sigma_{11}^2} = \frac{2\text{SNR} \cdot Q\Delta T}{(\sqrt{\Sigma_{11}}/R)^4}, \quad (4.35)$$

where we have used $\Sigma_{11} \approx \overline{\tilde{s}^2(k+1|k)}$. The equation (4.35) has been

plotted on the ZNL I. F. curves, figures 4-3 through 4-5 for representative values of the $\text{SNR} \cdot Q$ product, with $\Delta T = 1$ for convenience. The intersection of these lines with the ZNL I. F. curves then represent a graphical solution of the two conceptual relations (4.20) and (4.21). For a given set of model parameters, Q , and SNR , one determines the estimator operating point $\sqrt{\Sigma_{11}}/\bar{R}$, at this intersection, which can be converted to estimation error variance in radians using $R = 1/2 \text{ SNR}$. The operating point for the linear time-invariant system is the intersection of the $Q \cdot \text{SNR}$ line with the horizontal, 0 dB I. F. axis.

4.5.2 Simulation Technique

Figure 4-1 shows the general estimator block diagram plus the interaction with the atmospheric noise sample record. This sample record is described in Chapter 2 and consisted basically of 10-second bursts of nearly simultaneous samples of the rf noise in frequency channel 1 and the envelope in channel 2. The sampling rate was 1 kHz and with total length of approximately 10^5 samples. Only the magnitude of the rf noise samples was recorded and this sample record was converted to a bipolar record using a random number generator to assign a sign bit to each sample. This provided an uncorrelated time series as the results of Chapter 2 indicated was appropriate for sampling intervals greater than the bandlimiting filter time constant. A computer generated time series of statistically independent, normal samples with unit variance, was written "alongside" the atmospheric noise record to provide the signal model driving process. As indicated on Figure 4-1 the noise and signal samples were scaled by the appropriate factor as they were read from

the magnetic tape for each simulation run to provide the specified Q and R levels for that simulation.

For the linear time-invariant estimator, the loop parameters are given by (4.33). For the two ZNL types that were tested, 15% clipping and hard limiting, (4.34) was used with R given by

$$R = \frac{1}{2\text{SNR} \cdot \text{I. F. (Solution)}},$$

where I. F. (solution) indicates the I. F. at the predicted estimation error operating point in Figures 4-3, 4-4. In addition, the c value curve, Figure 4-5, was used by entering at the predicted $\sqrt{\Sigma_e/R}$ operating point and reading the c/\sqrt{R} value. The factor, $1/c$, was applied following the ZNL to maintain average signal gain through the device at unity. In the case of 15% clipping, the threshold yielding 15% clipping, which was computed in the ZNL performance analysis, was used and rescaled to the R value of each simulation. This threshold can be easily set by a long-time digital servo loop as previously noted. This approach was not used here to allow use of the entire sample record for testing of the performance analysis. To recognize the fact that the ZNL estimator analysis was only approximate, three simulations were run in parallel for the clipper and hard limiter with slightly smaller and larger loop bandwidths than predicted (realized with a change in c value) to verify that the composite gain term, yielding minimum estimation error, was correctly given by the analysis.

For the time-varying filter, two parameters, $\sigma_{nG}^2 \triangleq R_{\min}$ and v_t , were entered for each noise record to describe the experimental curve,

$\sigma_y^2(k) | v_o(k)$. These were related to $R(k+1)$ by the algorithm of section 4.4.1.

The time-varying value of $K(k+1)$ was then computed from (4.12)-(4.14) with $\Sigma(0|0) = 0$ although this initial condition decayed so quickly with respect to the sample record length as to have no effect. The time-varying clipper, recognizing the fact that the conditional rf noise distribution was not exactly gaussian (section 4.4.1), was implemented as

$$Z(k+1) = \begin{cases} Z(k+1), & |Z(k+1)| \leq 3\sqrt{\Sigma(k+1|k) + R(k+1)} \triangleq Z_t \\ \pm Z_T, & Z(k+1) \geq \pm Z_T. \end{cases} \quad (4.36)$$

The complete simulation then consisted of four types of PLL estimators being driven by the same sample record of simulated signal and recorded atmospheric noise samples. The resulting estimation error was evaluated at each iteration as seen in Figure 4-1, with this error used to plot the time evolution of the error and determine the error variance. The results of the scalar simulation for all noise conditions is given below.

4.5.3 Simulation Results for Scalar Model

Four plots of the standard deviation of the estimate error are shown in Figure 4-6 for the scalar model simulation. The effective noise improvement scale is computed from (4.35). The upper right plot represents the widest effective estimator bandwidth tested and we see that the time-varying filter performs slightly better under all conditions, while the hard limit ZNL is definitely the poorest estimator form. Referring to Figure 4-3, the hard limit I.F. for frontal noise conditions falls below that of clipping at this Q SNR product and this fact is reflected in the

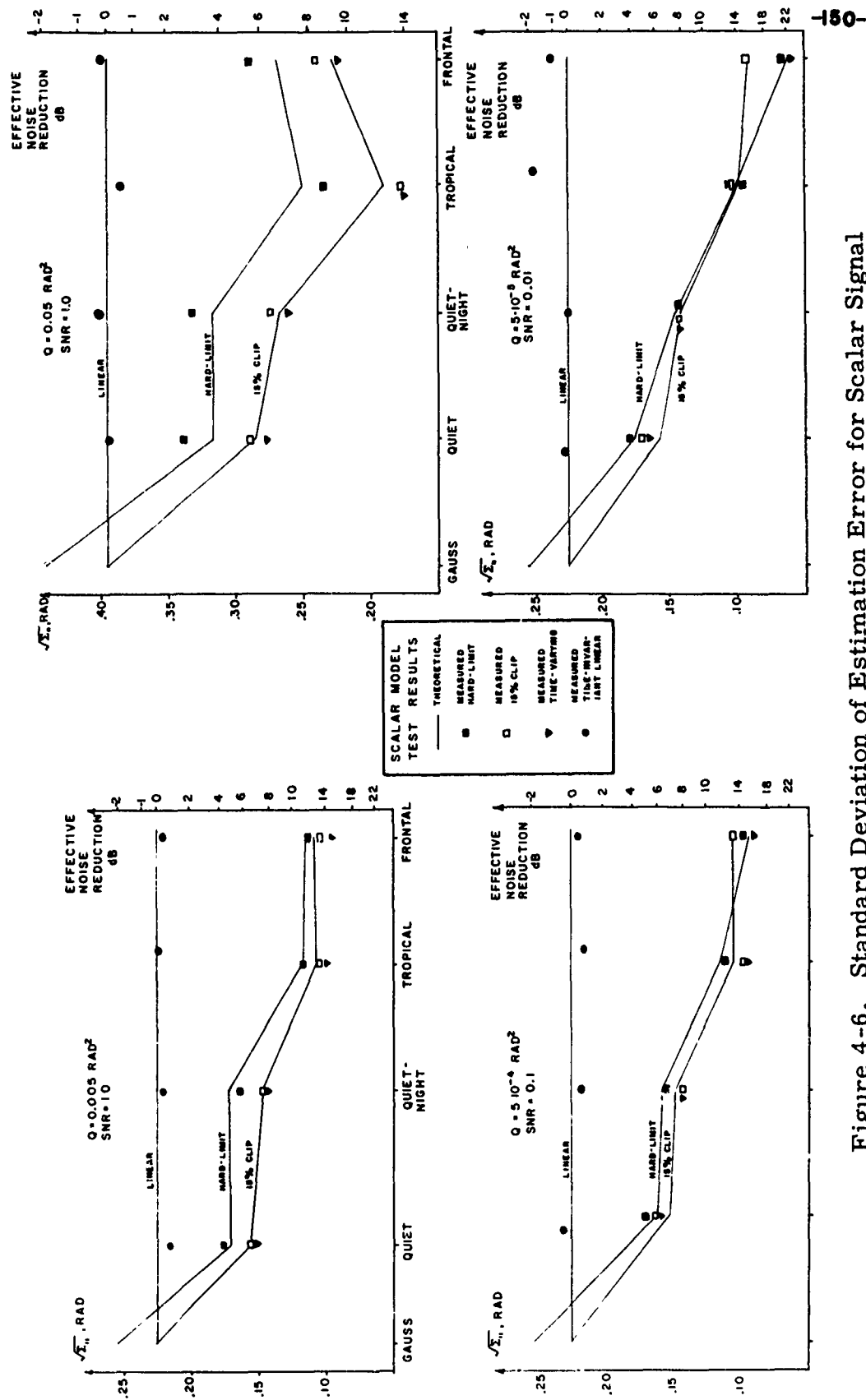


Figure 4-6. Standard Deviation of Estimation Error for Scalar Signal Model

simulation results. The other noise conditions, where the hard limiter is poorer at this Q SNR product, predict similar large separations in the performance between hard limiting and clipping and this is found in the simulations.

As the estimator bandwidth is reduced by decreasing Q and SNR (upper left, lower left, lower right in that order) we see that the performance of hard limiting and clipping draws closer together, both predicted and tested. In the lower left, a crossover between clipping and hard limiting is predicted and found in the test results. This is clearly seen in Figure 4-3 for frontal noise conditions. The time-varying optimum filter follows the best ZNL performance and generally exceeds it slightly as the MMSE ZNL performance predicts. The least separation between the best ZNL tested and time-varying is found in the narrowest estimator bandwidth test, lower right. Here, the effects of noise power level correlation are erased by the long processing time involved. All that is required is the proper ZNL noise limiting in the estimator, the dynamic performance advantage of the time-varying filter is averaged out by the processing time.

A plot of the time evolution of the estimation error is shown for two conditions in Figure 4-7. In the upper traces, the time-varying filter is seen to be clearly superior while in the lower plot the hard limiter appears somewhat better. Both of these traces are plotted on the same time scale, illustrating the differences in estimator bandwidth. We shall defer comments as to the implications of these results for receiver design until section 4.7. The results do appear to varify, at least for the scalar signal model, the applicability of the linearized ZNL estimator

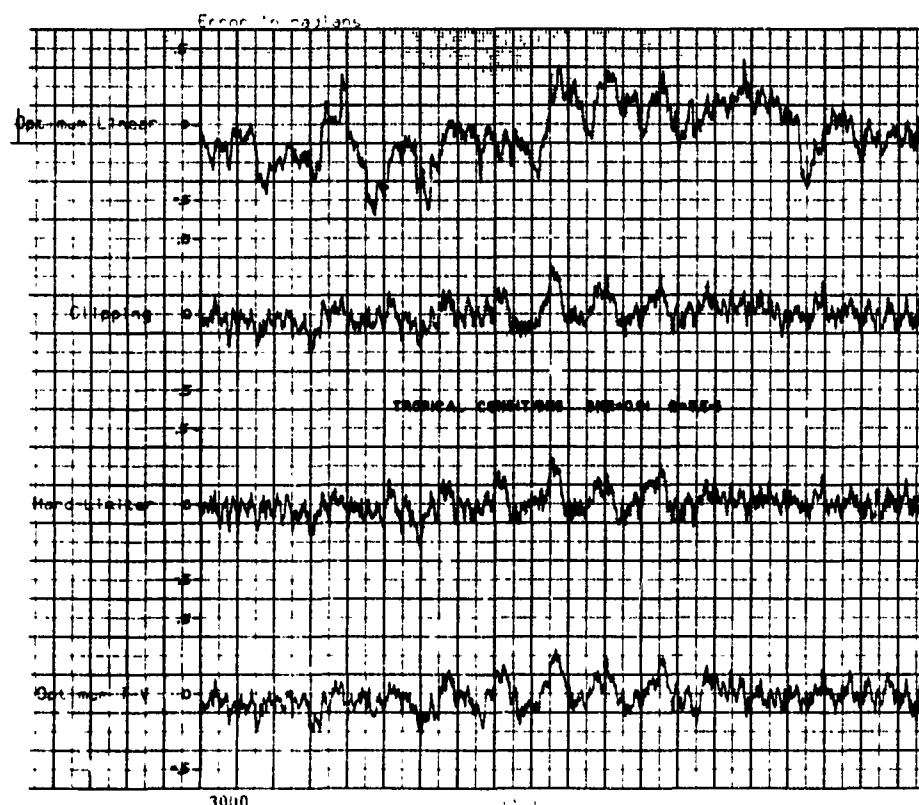
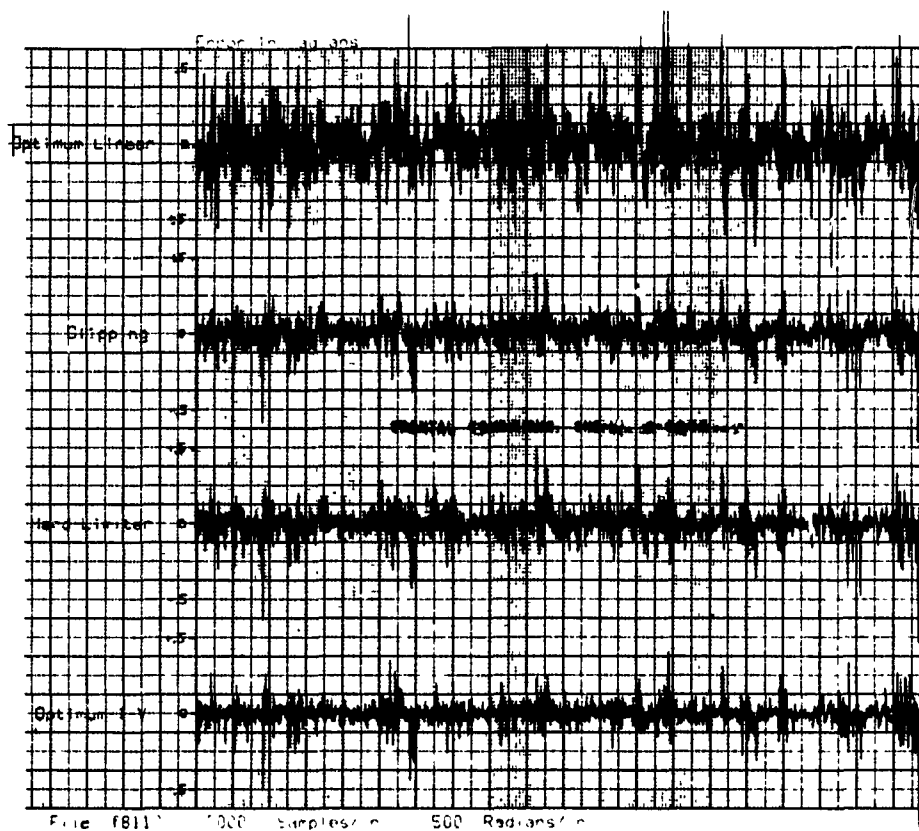


Figure 4-7. Time Evolution of Estimation Error for Scalar Signal Model

analysis and this application of the joint channel noise model with attendant concept of a time-varying gaussian noise process.

4.6 Performance of Estimators for Two-State Signal Model

4.6.1 Operating Equations

The most commonly used signal model for the navigation problem is two-state,

$$\begin{bmatrix} \dot{s}_1(t) \\ \dot{s}_2(t) \end{bmatrix} = \begin{bmatrix} 0 & 1 \\ 0 & 0 \end{bmatrix} \begin{bmatrix} s_1(t) \\ s_2(t) \end{bmatrix} + \begin{bmatrix} 0 \\ 1 \end{bmatrix} u(t)$$

a double integrator model. Physically, this form of signal generator, models platform movement as a random acceleration and allows for both phase ($s_1(t)$) and frequency ($s_2(t)$) offsets between the transmitter and receiver oscillators. The sampled data equations ((4.10)-(4.14)) for this continuous signal model are

$$\Phi(\Delta T, 0) = e^{\underline{F}(\Delta T)} = \begin{bmatrix} 1 & \Delta T \\ 0 & 1 \end{bmatrix}, \quad (4.37)$$

$$E[u(k) u(k)^T] = Q \begin{bmatrix} \Delta T^2/3 & \Delta T^2/2 \\ \Delta T^2/2 & \Delta T \end{bmatrix} \approx \begin{bmatrix} 0 & 0 \\ 0 & Q\Delta T \end{bmatrix}$$

The sampled data steady-state covariance equations ((4.13), (4.14)) lead to fourth-order algebraic equations for this model and they cannot be solved analytically. We therefore solve the steady-state continuous time equations, (4.9), to obtain

$$\underline{\Sigma}(\infty) = \begin{bmatrix} \sqrt{2} R^{3/4} Q^{1/4} & \sqrt{RQ} \\ \sqrt{RQ} & \sqrt{2} R^{1/4} Q^{3/4} \end{bmatrix}, \quad \underline{K} = \begin{bmatrix} \sqrt[4]{\frac{4Q}{R}} \\ \sqrt{\frac{Q}{R}} \end{bmatrix}. \quad (4.39)$$

The steady-state continuous time estimator is then given as

$$\begin{bmatrix} \dot{\hat{s}}_1(t) \\ \dot{\hat{s}}_2(t) \end{bmatrix} = \begin{bmatrix} -\sqrt[4]{\frac{4Q}{R}} & 1 \\ -\sqrt[4]{\frac{4Q}{R}} & 0 \end{bmatrix} \underline{\hat{s}}(t) + \underline{K} r(t),$$

which, when converted to a scalar transfer function, is

$$H(s) = \frac{\sqrt{\frac{Q}{R}} + \sqrt[4]{\frac{4Q}{R}} s}{s^2 + 2 \left[\frac{1}{\sqrt{2}} \right] \left[\sqrt[4]{\frac{Q}{R}} \right] s + \left[\sqrt[4]{\frac{Q}{R}} \right]^2}. \quad (4.40)$$

$H(s)$ is recognized as a critically damped second-order filter as is usually specified for navigation PLL's.³⁹ Thus to relate our model to classical specifications, one need only solve for Q , for a given filter bandwidth and noise variance specification,

$$\omega_f = \sqrt[4]{\frac{Q}{R}}, \quad Q = \frac{\omega_f^4}{2 \text{ SNR}}.$$

The steady-state estimation error and gain coefficients for the equivalent sampled data system is obtained by substituting the results

of section 4.2.2 into (4.39). For the phase estimate variance we obtain, with the introduction of the ZNL Improvement Factor,

$$\Sigma_{11}(\infty) = \sqrt{2} \left[\frac{R\Delta T}{\text{I.F.}} \right]^{3/4} Q^{1/4},$$

$$\text{I.F.} = \frac{(8Q \cdot \text{SNR} \cdot \Delta T^3)^{1/3}}{(\sqrt{\Sigma_{11}/R})^{8/3}} \quad (4.41)$$

Expression (4.41) is plotted on the ZNL I.F. curves, Figures 4-3, 4-5, for a representative range of $Q \cdot \text{SNR}$ products, with ΔT again set equal to one for convenience. These plots show that the two-state estimator operating point lines have less slope than in the scalar case, which is due to the coupling of errors between the phase and frequency states ($s_1(k)$, $s_2(k)$). We also note that a large spread of parameter values is more concentrated in a region of the I.F. curves indicating that there should be less change in relative estimator performance for different ZNL's with this signal model. The sampled data estimator for the time-invariant simulations is given by

$$\begin{bmatrix} \hat{s}_1(k+1|k+1) \\ \hat{s}_2(k+1|k+1) \end{bmatrix} = \begin{bmatrix} 1 & \Delta T \\ 0 & 1 \end{bmatrix} \hat{\underline{s}}(k|k) + \begin{bmatrix} \sqrt[4]{\frac{8Q \cdot \text{SNR I.F.}}{\Delta T}} \\ \sqrt{\frac{2Q \cdot \text{SNR I.F.}}{\Delta T}} \end{bmatrix}$$

$$\cdot \frac{1}{c} f(r(k+1) - s_1(k+1|k)); \quad (4.42)$$

$c = 1$, I.F. = 1, $f(\cdot) = \cdot$ for linear; c , I.F., $f(\cdot) \rightarrow$ ZNL solutions for nonlinear.

Using the two-state sampled data signal model, (4.37) and (4.38) and the time-varying covariance matrix recursions (4.13) and (4.14) we can determine the sampled data covariance recursion as

$$\underline{\Gamma}(k+1|k) = \begin{bmatrix} \Sigma_{11} + 2\Delta T \Sigma_{12} + \Delta T^2 \Sigma_{22} & \Sigma_{12} + \Delta T \Sigma_{22} \\ \Sigma_{21} + \Sigma_{22} \Delta T & \Sigma_{12} + Q \Delta T \end{bmatrix}, \quad (4.43)$$

$$\Sigma_{ij} = \Sigma_{ij}(k), \quad \Sigma_{21} \equiv \Sigma_{12}, \quad \underline{\Gamma}(k+1|k) = \underline{\Sigma}(k+1|k),$$

$$\underline{\Sigma}(k+1|k+1) = \begin{bmatrix} \frac{\Gamma_{11} R(k+1)}{\Gamma_{11} + R(k+1)} & \frac{\Gamma_{12} R(k+1)}{\Gamma_{11} + R(k+1)} \\ \frac{\Gamma_{21} R(k+1)}{\Gamma_{11} + R(k+1)} & \frac{\Gamma_{11} \Gamma_{22} - \Gamma_{12}^2 + \Gamma_{22} R(k+1)}{\Gamma_{11} + R(k+1)} \end{bmatrix}, \quad (4.44)$$

$$\Gamma_{ij} = \Gamma_{ij}(k+1|k), \quad \Gamma_{12} = \Gamma_{21}.$$

Note that here we are using the actual sampled data model based on the physical continuous time system and hence use $Q\Delta T$ and R as the signal driving process and noise variance, respectively. The recursions (4.43) and (4.44), which cannot be solved analytically for the steady state $\Sigma(\infty)$ value, are required in the time-varying filter to compute the gain $\underline{K}(k+1)$. This gain is computed for each sample iteration from (4.43), (4.44), and (4.12). To verify that the approximate sampled-data/continuous relations, in conjunction with (4.39), yield the value to which (4.43)

and (4.44) converge, they were iterated numerically using a sampling interval

$$\Delta T = \frac{2\pi}{N} \cdot \sqrt[4]{\frac{R}{Q}},$$

where N is the number of samples per unit of filter time constant. The actual iterated values of the $\underline{\Sigma}(\infty)$ matrix agreed to within 1% of those given by substituting $R_{eq} = R\Delta T$ into (4.39) for $N \geq 100$.

4.6.2 Simulation Technique

The simulation technique used for the two-state signal model was essentially that given for the scalar case. The estimator recursion was given by (4.42) with the appropriate ZNL parameters determined by the graphical solutions of (4.41) with the I.F. curves. The same mapping from $E(k+1)$ to $R(k+1)$ was used for the time-varying filter, with the estimator equations given by (4.43) and (4.44) plus the general K-B equations. The time-varying clipper was also used as per (4.36).

4.6.3 Simulation Results for Two-State Model

The standard deviation of the phase estimate error is shown in Figure 4-8, in the same format as used for the scalar model results. The three plots are for decreasing estimator bandwidth, upper left, lower left, and right, respectively. In the first plot, we note the magnitude of the error is such that we cannot conclude that the small $\tilde{s}(k+1|k)$ assumption holds and we must interpret this as merely an extension of the linear model to determine the effects of bandwidth versus the noise conditions and estimator structures.

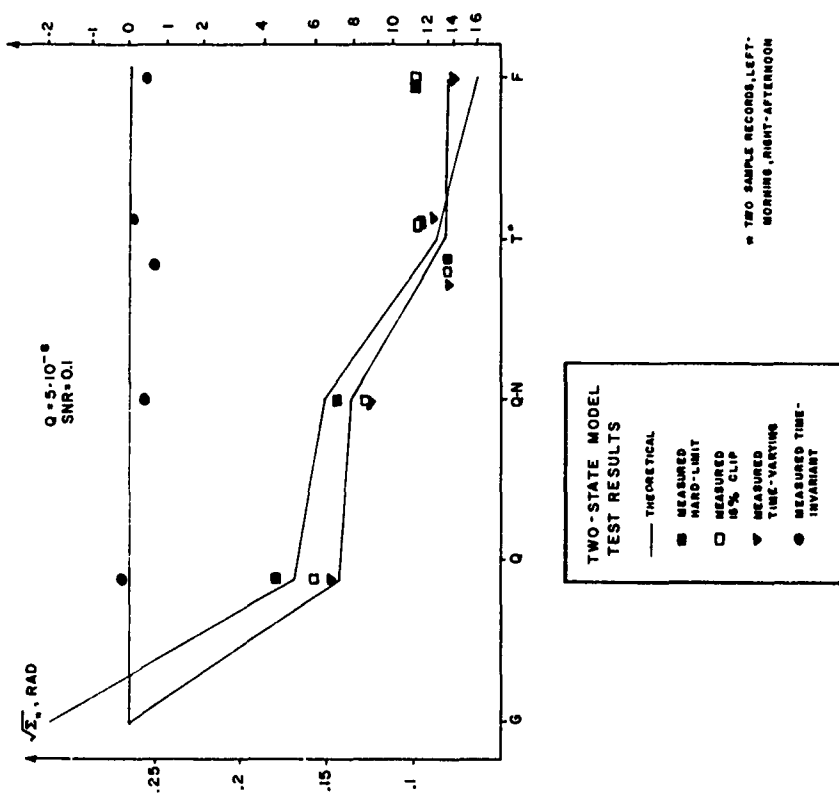
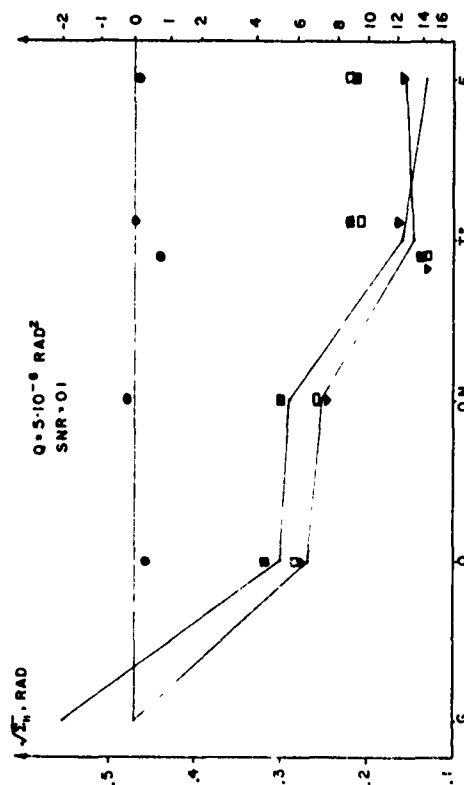
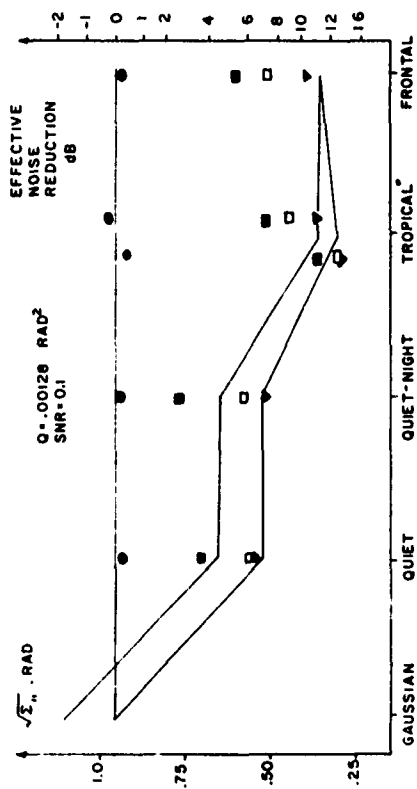


Figure 4-8. Standard Deviation of Estimation Error for Two-State Signal Model.

A general comment that applies to all of these results is that the two-state model, with its coupling between phase and frequency state errors, produces many instances of significant deviations between linearized predictions and actual results. We attribute this to the state coupling and the effect of multiple discharges in the atmospheric noise record that reduce the information content of long sample sequences. In all of the frontal noise simulations the optimum time-varying filter performs at least 3 dB better due to its improved dynamic response and optimal weighting of uncontaminated samples. This improvement is also seen in the tropical noise record recorded in the afternoon (right-hand set of points) as compared to the morning. These two records yielded essentially the same joint first order analysis and model parameters, yet the particular time structure differences of the two sample records produced these simulation differences.

We note also in these three simulations that the discrepancies between linearized predictions and actual test results are reduced for decreasing estimator bandwidths (increasing observation intervals) as we would expect. Thus the quiet-night conditions, which we noted in Chapter 2 exhibited a long-time correlation in the $A(t_i)$ estimates, produced a performance difference at the largest estimator bandwidth which disappeared for the other two bandwidths. A similar comment applies to the right-hand (afternoon) tropical noise record. The cross-over in the hard limiting versus clipping performance for frontal noise, predicted by the ZNL I. F. curves and observed in the scalar simulations, does not occur for the two-state model although again the differences

decrease with decreasing estimator bandwidth.

In contrast to these observations, we see that the quiet noise conditions, which had no significant multiple discharge activity, produce results agreeing with the linearized analysis for all signal models and Q/SNR conditions. We can conclude then that the performance prediction discrepancies are directly attributable to this noise time structure wherein successive samples are not statistically independent, although uncorrelated.

Two representative plots of the time evolution of the estimate error are shown in Figure 4-9 where the relative differences in performance given by the error statistics can be seen.

The results of the two-state simulation indicate that the linearized ZNL analysis is valid for most noise/signal conditions of interest, although this begins to break down for short estimator bandwidth relative to the noise time structure. Using (4.43), the upper left simulation has approximately 50 samples per estimator time constant, which for the 1 kHz sampling rate used for all of the noise records corresponds to a 50-100 msec observation interval. We recall from Chapters 2 and 3 that multiple discharge phenomena have typical lengths in the 200-400 msec region. Thus significant growth of signal state uncertainty (refer to section 4.4.2 discussion) can occur during such a noise burst which is not optimally compensated for by the ZNL estimators, or, reflected in the linearized analysis. Corresponding samples per time constant figures for the other two simulations are 200 and 628, indicating that the effect of multiple discharges becomes progressively less significant with the

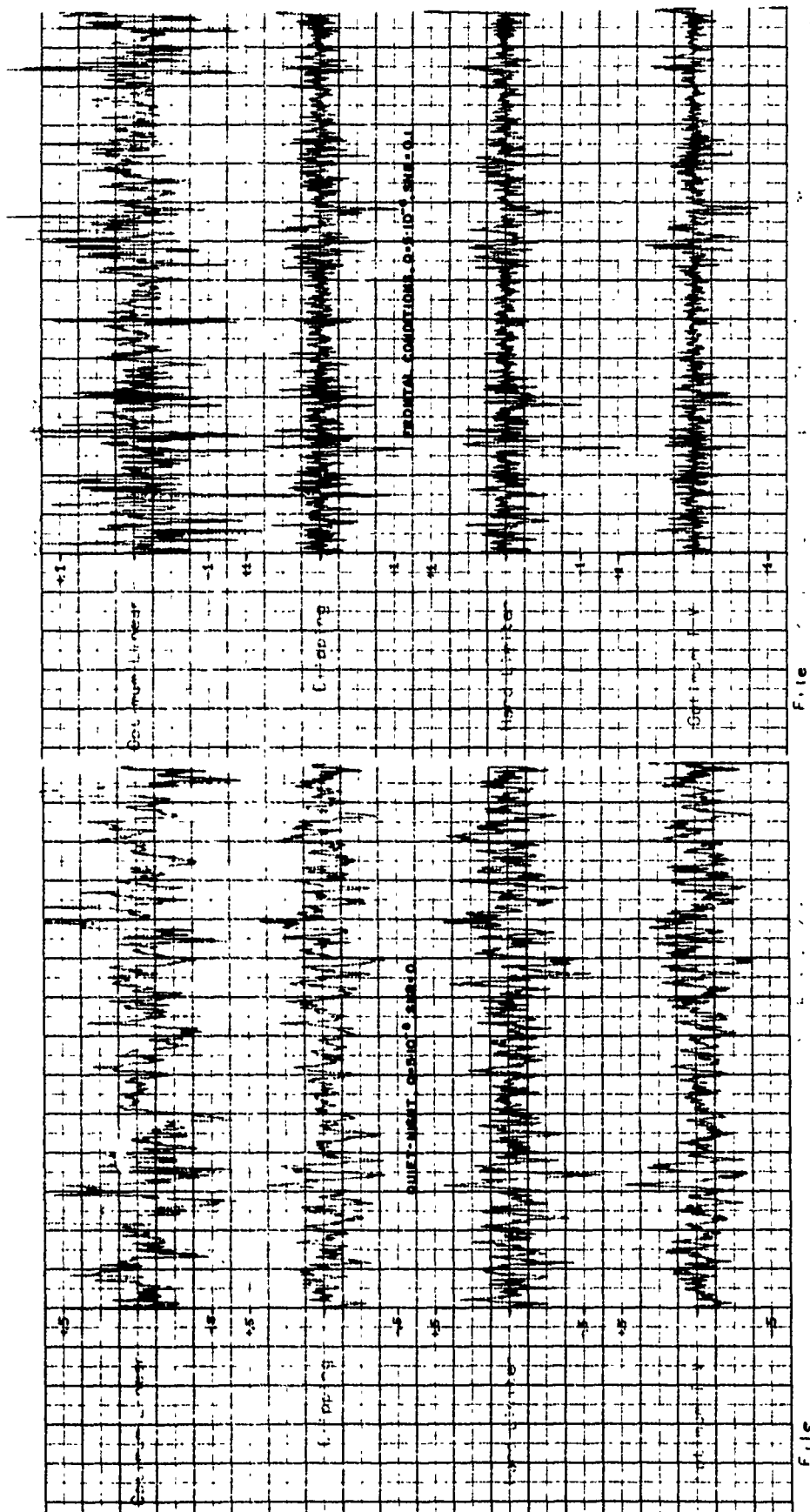


Figure 4-9. Time Evolution of Estimation Error for Two-State Signal Model

performance results noted. The general improved performance of the time-varying estimator again validates the joint channel model concept and also indicates under what noise/bandwidth conditions the use of this model and filter results in significant performance improvement. Generally, this improvement is significant for more complex signal dynamics and/or observation intervals that are comparable to, or less than, the longest interval of noise statical dependence.

4.7 Summary and Remarks

4.7.1 Summary of Navigation Receiver Design Results

In this chapter we have considered the problem of estimating the phase of a received rf carrier when the observations are corrupted by additive atmospheric noise. The phase of the rf signal may be considered as a random signal process representing the geographic position of the receiver relative to the transmitting station. As such, this problem is the most fundamental sub-problem in the design of a navigation receiver. A linearized approximation to the sampled received phase was used, and three types of estimator structures were considered; a linear time-invariant estimator matched to the received noise power and signal model, a time-invariant estimator using a zero memory nonlinearity (ZNL) acting on the loop error signal to attenuate large noise excursions, and a near optimum time-varying estimator utilizing samples of the noise envelope from an adjacent frequency channel as a measure of the time-varying power level of the received noise.

The performance of the ZNL type of estimator was analyzed by

replacing the ZNL with an equivalent gain and replacing the received noise with the difference between the ZNL output and actual error signal. For the case of a small error signal, this loop could be optimized through the use of a linear time-invariant estimator following the ZNL, which was matched to the effective noise power at the ZNL output and the signal model. This approximate analysis allowed complete estimator performance to be specified from an analysis of the ZNL based on the first-order pdf of the noise and error signal. This analysis was carried out using the first-order noise model from Chapter 3. Four types of ZNL's were analyzed in this manner, the optimum (MMSE) ZNL, hard limiter, clipper and hole puncher. Based on this analysis two types of ZNL's were considered most practical for actual use, a hard limiter and clipper.

The performance of the third type of estimator, the time-varying Kalman-Bucy filter, could not be quantitatively analyzed due to the non-linear dynamic covariance equations involved. The qualitative operation of the loop was discussed and shown to provide essentially the same behavior as the ZNL in terms of attenuating large noise excursions and, in addition, providing a dynamic compensation for the loss of signal information during large atmospheric noise bursts. An optimistic lower bound on estimator error was related to the variance of the background component of atmospheric noise which is of constant power level and uncorrelated between frequency channels. A more practical lower bound was suggested to be that predicted by the MMSE ZNL estimator, although a formal proof of this conjecture was not obtained.

Four estimator structures, linear time-invariant, hard limiting, clipping and time-varying were simulated on a computer. Actual

atmospheric noise sample records were used to provide the noise component and a computer-generated gaussian random process was used to represent the signal. The results of these simulations showed that the linearized ZNL analysis, based on the atmospheric noise model, provided quite accurate predictions of actual performance. Where the actual error variance was found to be greater than that predicted, the optimum time-varying estimator generally provided improved performance, approaching the optimum predicted. The conditions required to realize this improvement over a time-invariant ZNL estimator were complex signal dynamics (a two-state signal model as compared to a scalar) and an effective estimator time constant, or observation interval, on the same order, or less than, the longest time interval of correlated noise statistics, approximately 0.5-1 second. These application results verify our hypothesis from Chapters 2 and 3 that the most significant characteristic of atmospheric noise is the first-order pdf, with the noise-burst time structure of second- or third-order significance. Where the latter is, or thought to be, important, it can be optimally accounted for through the use of the joint channel noise model and the concept that the noise waveform can be modeled as a time-varying gaussian process, which leads to the optimum time-varying estimator.

4.7.2 Remarks on Receiver System Design

Prior to offering some general conclusions on the suitability and realization of the three basic types of PLL's we have studied, we shall consider two related topics.

- a) Other ZNL's. The generally excellent results we have obtained in analyzing three specific types of ZNL's, operating in all types of atmospheric noise conditions, suggests that other ZNL types, of interest in a particular application, can be similarly analyzed with confidence in the resulting performance predictions. The use of the ZNL Improvement Factor and noise model parameter sets provide the designer the tools necessary to do this.
- b) RF Bandwidth Effects. If we compare the effective noise reduction factor from the plots of simulation results with the changes in normalized rms noise level given in Table 3-1, we see that the best ZNL estimator will achieve a performance nearly equal to that caused by the background gaussian noise component (except for the severe and atypical frontal noise conditions). In other words, the estimator will be nearly insensitive to increases in noise level caused by changing weather/noise conditions. We recall from section 3.9.2 that the effect of reducing the bandwidth of the rf bandlimiting filter is to increase the apparent background gaussian noise component for increasingly severe noise conditions (p_x increasing). Thus, the ZNL estimators will not maintain constant weather/noise performance with rf bandwidths significantly less than 1 kHz. Rather they will tend towards the degradation in performance seen for an ideal, linear, time-invariant system. While our experimental investigations have not identified the rf bandwidth at which these effects become significant, our application results, based on the noise model, indicate the largest effective noise reduction one can obtain with

an optimal bandwidth selection, since, there are no significant changes in either model or application results for bandwidths larger than 1 kHz.

4.7.2.1 Linear Receivers

A general result from the analysis and tests of navigation PLL's in this chapter is that one should not employ a wide dynamic range, linear PLL, for signals corrupted by atmospheric noise. Where the other important aspects of a design problem (such as interference susceptibility^{47, 51}) dictate the use of a linear type system, some sort of clipper nonlinearity should also be employed. Our results show that this provides near optimum operation for most signal-to-noise ratios, signal models, and types of atmospheric noise. As we have noted, the implementation of the adaptive threshold clipper that we have used is quite easy, although any similar type of threshold setting procedure would probably perform nearly as well. The only other parameter required in such a system to achieve optimum performance for a given signal model (or alternatively, in a classical context as defined in section 4.2.3, to maintain a fixed loop bandwidth) is the effective noise power, which can be estimated from the variance of the ZNL output sequence. Thus an intuitive and reasonable modification to a basic linear PLL will provide near optimum performance for atmospheric noise.

4.7.2.2 Hard Limiting Receivers

The great attraction of a hard limiter ZNL, as we have employed it here, is that the PLL can be almost entirely realized with digital

circuits. A stable analog oscillator, low level preamplifier, and limiter circuits are the only analog elements required in the general case, although other variations such as analog feedback to a voltage-controlled oscillator can be employed. The hard limiting receiver provides near optimum performance in most cases, especially those with longer observation intervals which are the cases of greatest practical interest. Another advantage that is often associated with hard limiting PLL's is that they do not appear to require automatic gain control loops (AGC). However, this is not quite the case. The function of AGC in the linear receiver (with or without clipper) is to stabilize the effective loop error gain (\underline{K}) at a prescribed value which is optimum for a given signal model and noise power, or in the classical design sense, results in a prescribed loop bandwidth. The hard limit PLL requires exactly the same sort of information for exactly the same purpose, namely, the effective gain c of the limiter ZNL and the effective signal-to-noise ratio to specify the optimum loop gain, \underline{K}^* . We see from the expressions (4.29) and (4.30) defining these two parameters that they depend only upon the probability density of the loop error process, $z(k+1)$, evaluated at zero, $p_z(0)$. This can be estimated in a practical application by using a window discriminator with a small but finite width, centered at zero volts, and a counter. This would determine the average occupancy of this increment, by the input analog waveform, at the VCO zero crossing time (sample time).

* While hard limiters tend to be self-adaptive over a limited range^{45, 48} this variation does not result in optimal compensation nor does it consider the additional problem of adaptation to the changing character of atmospheric noise.

Thus, a hard limiting system can be designed to provide near optimum performance for most atmospheric noise and SNR conditions without sacrificing realization simplicity. A "choice" between a hard limit or linear-with-clipping type PLL for the navigation application would seem, then, to depend upon factors other than the atmospheric noise performance that we have investigated.

4.7.2.3 Optimum Time-Varying Receiver

The optimum time-varying PLL that we have considered in this work is definitely more complex than either of the two ZNL types, requiring both the co-channel envelope information and small digital computer to compute the covariance propagation and resulting time-varying gain, $K(k+1)$. The latter capability is often found in modern receiver systems, especially integrated navigation systems that combine inertial platforms or Doppler radar systems with radio aids. The co-channel information can be provided by a relatively unsophisticated algorithm to determine the two points on the $\sigma_y|v_0$ curve that were used to establish $E(k+1) \rightarrow R(k+1)$ mapping. Such an optimum system should provide excellent adaptability to any type of atmospheric noise condition found throughout the world. However, there is very little performance advantage in the system for estimator time constants greater than several seconds, and these are the ranges of greatest practical interest. We conclude, therefore, that the principal use of the optimum structure based on the joint channel noise model has been to demonstrate the degree of optimality of other, more practical systems, over the range of signal and noise conditions that we have investigated.

Chapter 5

SUMMARY AND SUGGESTIONS FOR FURTHER WORK

5.1 Summary

The work reported here has involved three distinct phases; experimental observations, mathematical modeling, and use of the model in a practical design problem. As we have stressed at several points, the end use of the model is an engineering tool, and this has provided motivation and guidance as to approximations and characteristics that were more, or less, important in the previous efforts. Three significant results of the experimental and modeling efforts can be summarized as follows

- 1) The model provides a first order probability density for a band-limited atmospheric noise waveform or noise envelope, and a first order joint probability density for similar waveforms observed in disjoint frequency channels.
- 2) The time structure of the noise model approximates at least one important aspect of the long time statistical dependence of atmospheric noise waveforms (beyond the correlation time of the bandlimiting filter).
- 3) Comparison of the noise model with extensive measurements of bandlimited atmospheric noise shows that the model matches important noise characteristics over a broad range of noise conditions. This comparison provides a table of model parameters describing this range of noise behavior.

The use of the atmospheric noise model in this work was restricted to a specific problem and considered only certain sub-specifics within that problem, such as the type of zero memory non-linearity to use in a filter. A discussion of these details is given in Chapter 4. On a broader level we believe there are two significant results from this application of the noise model:

- 1) A useful approximation for atmospheric noise is to consider samples spaced beyond the bandlimiting filter correlation time to be statistically independent. Under this assumption the first order probability density, for all types of noise conditions, provides the information necessary to determine the performance of various types of receiver structures. This independence assumption and use of the first order model yielded the ZNL filter analysis of Chapter 4.
- 2) The joint channel noise model and the concept of modeling the noise as a time-varying Gaussian process allows one to determine the near optimum performance of a receiver operating in all types of atmospheric noise. Even if such a design would not be considered practical for implementation, it provides a fundamental limit for comparison with other simplified designs.

5.2 Suggestions for Additional Work

5.2.1 Noise Model

As noted at the end of Chapter 3 the most significant questions for further experimental research on this type of noise model involve frequency dependent effects. The most important would be a determination

of the effect of rf bandwidth on the model parameters. While our results are for relatively broad bandwidths that allow one to determine the maximum performance improvement possible with atmospheric noise, a designer must know at what point bandwidth reduction begins to penalize these improvements. Other significant questions might be listed as follows:

- 1) Explore the joint channel model in more detail at VLF where the impulsive return stroke is more important than the leader noise burst.
- 2) Determine the effectiveness of the noise model at frequencies above LF. Since the noise at these frequencies is increasingly dominated by the noise burst properties of the discharge, we would expect that the model would be increasingly effective.
- 3) Determine the effect on the joint channel model of separation between channels at VLF, LF, and above.

The measurement suggested here could probably be most conveniently made by an instrumentation system using frequency shifting techniques to standardize filter shapes at the intermediate frequency. We avoided this approach in our work because of the difficulty in realizing extremely wide dynamic range multipliers to accomplish the shifting operation. Our results show that the application of the noise model is not critically sensitive to the large noise amplitudes and hence a system of reduced dynamic range that introduced a zero memory distortion (no memory over the sampling interval) at these amplitudes would not seriously compromise the resulting data analysis and modeling.

5.2.2 Application to Communication Receivers

The low frequency electromagnetic spectrum accommodates a greater number of digital communication systems than radio navigation systems. Most of these digital signalling schemes employ bit lengths of the order of 20-50 msec. This time period, the length of the observation interval in which the receiver must decide which of m signals was sent, is in the range where we found that the optimum waveform estimation receiver offered the greatest improvement over simple non-linear processing techniques. We suspect that similar and perhaps more dramatic improvements are possible in the digital receiver detection problem.

Just as in the estimation application, the model of the noise process as a time-varying Gaussian process provides immediate application of the general results of detection theory that include time-varying Gaussian power levels. In the simplest form of detection problem, deciding whether a known signal is present or not, we can draw the form of the optimum detection receiver directly from the insight provided by the joint channel noise model. In Figure 5-1 we see in the upper portion a basic correlation receiver for this problem. The received waveform, $r(t)$, is correlated against a replica of the transmitted signal and the result integrated over the observation interval to form the test statistic. The block labeled $f(z)$ is a linear transfer function in the linear form of the receiver, which implicitly assumes

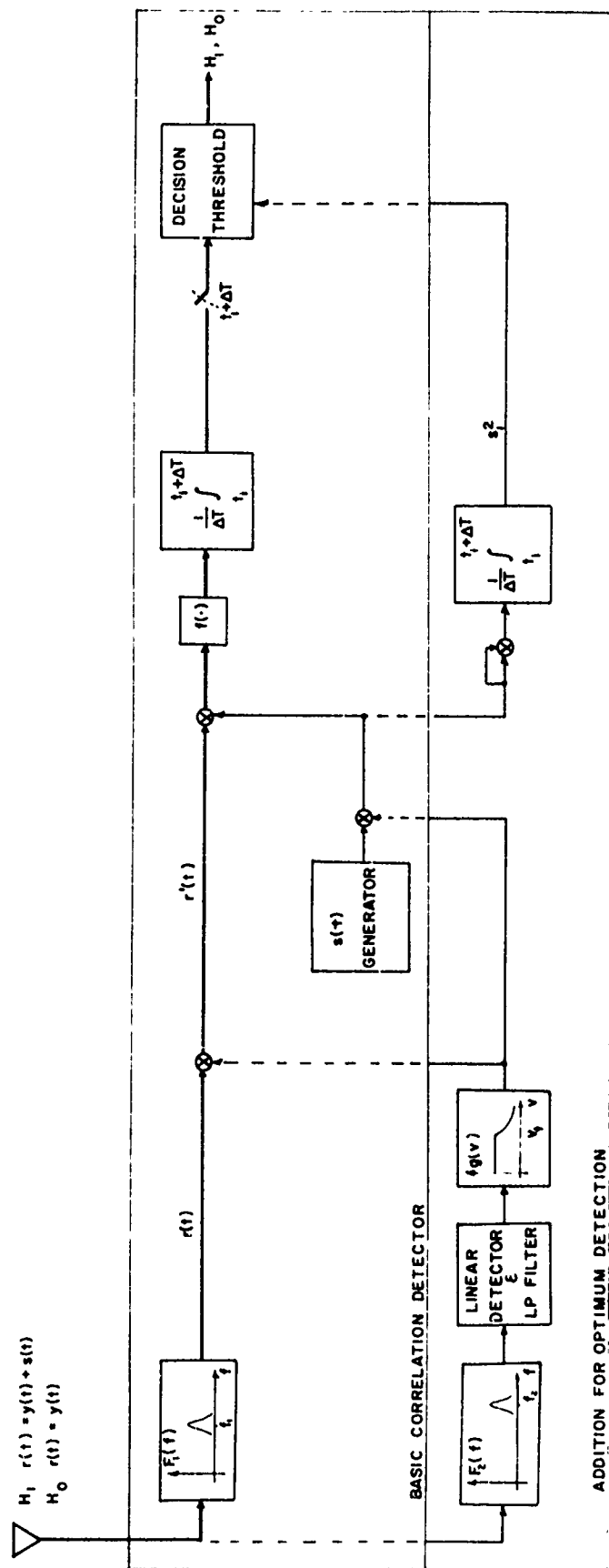


Figure 5-1. Optimum Digital Receiver for Atmospheric Noise

the atmospheric noise is white and Gaussian.* In typical atmospheric noise applications this function is a clipper or hole puncher or, it can be specified in a more optimal manner using the results of various studies^{43, 44, 50} concerned with the optimal non-linearity for statistically independent samples of non-Gaussian noise. The decision threshold is then determined from the criterion to be used³⁷ (Bayes, Neyman-Pearson, Min-Max etc) and the effective noise and signal power. These latter parameters must be calculated in a manner similar to the analysis used in Chapter 4 for the ZNL estimator. One would use the first order pdf of the noise (thus using an ensemble average of noise waveforms for that noise/weather condition) and compute the signal suppression and the effective noise power at the output of $f(z)$.

The lower portion shows the nearly optimal use of the pilot channel noise information. The pilot channel filter, $F_2(f)$, is specified to have exactly the same lowpass envelope response as the signal channel filter $F_1(f)$. This eliminates the problem of time offset found in our "worst-case" noise observation of Chapters 2 and 3 and should provide better correlation between waveforms than our experimental

*We note that the atmospheric noise component, $y(t)$, has a correlation function determined by the bandlimiting filter, $F_1(f)$. However, this filter is used to remove adjacent channel interference and hence $r(t)$ cannot be "whitened," the $y(t)$ component must be treated as white noise by the receiver.

results. The non-linearity, $g(v)$, realizes the inverse of the $E(k+1) \rightarrow [R(k+1)]^{1/2}$ mapping of Chapter 4 so that the output can be directly applied to the indicated multipliers. This results in an effective received signal, $r'(t)$, that has a nearly constant power level and a nearly Gaussian noise distribution (see section 3.4). This waveform is then correlated against a new $s(t)$, $s'(t)$, which reflects the effect of the scaling waveform derived from the pilot channel. The result may then be clipped by a fixed threshold $f(z)$ to include the fact that the joint channel noise model is an approximation and the effective noise power component of $r'(t)$ is not exactly Gaussian (this parallels the time-varying clipper of Chapter 4). After integration across the observation interval to form the test statistic, the decision is made using the effective signal power, s_1^2 , received during that interval and the nearly constant noise power of $r'(t)$.

The duality of the estimation problem of Chapter 4 and the detection scheme proposed here is evident. The time-invariant ZNL design and analysis uses the same assumptions and type of first order pdf analysis. The optimal time-varying detection receiver parallels the time-varying estimation receiver in the following ways; the inverse scaling operation attenuates noise excursions in the same way as the estimator's use of $R^{-1}(k+1)$ information (section 4.4.2) and the computation of effective signal power for each observation interval optimizes the decision threshold for that interval just as the time-varying estimator optimally weighted each sample via the $\Sigma(k+1|k+1)$ term of the gain matrix $\underline{K}(k+1)$.

We suspect that the optimum detection receiver will provide greater improvements than the optimum estimator tests indicated because of the short observations intervals, between which the atmospheric noise waveform is very non-stationary, and the fact that the estimator test records were based on samples spaced 1 msec apart, whereas the detection receiver can make effective use of much higher information rates. We also note that the optimum detection receiver employs principally analog multipliers which can be easily realized to operate at these VLF and LF frequencies. Extension of the suggested detector to actual FSK signalling schemes should be straightforward. We can also envision further uses of the joint channel information, for example, to "flag" bit decisions which have a high probability of error based on the actual signal-to-noise ratio for that observation interval. These flags could be employed in following decoders for error correction or retransmission requests.

BIBLIOGRAPHY

1. Pierce, E. T., "Atmospherics -- Their Characteristics at the Source and Propagation," Radio Noise of Terrestrial Origins, Part IV, URSI Record Elsevier Publishing Co., Amsterdam.
2. Beach, C. D. and D. C. George, "Error Performance of VLF and LF Receiving Systems with Nonlinear Atmospheric Noise Reduction," Westinghouse Electric Corp. Report RADC-TR-70-190, AD-875-991, September 1970.
3. Maxwell, E. L. and A. D. Watt, "Characteristics of Atmospheric Radio Noise from 1 kHz to 700 kHz," Proceedings of the IRE, 45, June 1957, 787-794.
4. Gupta, S. N., "Short Term Time Characteristics of Atmospheric Radio Noise Above Different Thresholds," IEEE Transactions EMC 13, Nr 4, November 1971.
5. George, T. S., "Investigation of Atmospheric Radio Noise," Engineering and Industrial Experiment Station, University of Florida, AD-133-763, November 1957.
6. Oh, L. L., "Measured and Calculated Spectral Amplitude Distribution of Lightning Spherics," IEEE Transactions EMC 11, Nr 4, November 1969.
7. Watt, A. D. and E. L. Maxwell, "Measured Statistical Characteristics of VLF Atmospheric Radio Noise," Proceedings of the IRE 45, pp. 55-67, January 1957.
8. Evans, J. E., "Preliminary Analysis of ELF Noise," Lincoln Laboratory Report ESD-TR-69-67, 1969.
9. Coon, R. M., et al., "A Simulator for HF Atmospheric Radio Noise," ESSA Technical Report ERL-128-ITS-90, July 1969.
10. Furutsu, K., and T. Ishida, "On the Theory of the Amplitude Distribution of Impulsive Random Noise," Journal of Applied Physics 32, Nr 7, July 1961.

11. Beckman, Peter, "Amplitude-Probability Distribution of Atmospheric Noise," Radio Science Journal of Research, NBS(USNC-URSI 68D, Nr 6, June 1964, 723-736.
12. Ibukum, Olu, "Structural Aspects of Atmospheric Radio Noise in the Tropics," Proceedings of the IEEE 54, Nr 3, March 1966.
13. Galejis, J., "Amplitude Distribution of Radio Noise at FLF and ULF," Journal of Geophysical Research 71, Nr 1, January 1966.
14. Modestino, J. W., "A Model for ELF Noise," Lincoln Laboratory Report ESD-TR-71-322, December 1971.
15. Eckberg, A., "Optimal Estimation of VLF Noise," S. M. Thesis, Massachusetts Institute of Technology (unpublished), June 1970.
16. Snyder, D., "Optimum Binary Detection of Known Signals in a Non-Gaussian Noise Resembling VLF Atmospheric Noise," Wescon Convention Record, Session 6, 1968.
17. Shaft, P. D., and J. O'Hara, "Modern Performance in VLF Atmospheric Noise," IEEE Transactions CT, October 1971.
18. Hall, H. M., "A New Model for "Impulsive" Phenomena: Application to Atmospheric-Noise Communication Channels," Stanford Electronics Laboratory Report SEL-66-052, AD-648-650, August 1966.
19. Kapp, J., and L. Kurz, "Performance of Two Suboptimum Detectors and Signal Selection in Gaussian and Impulsive Noise," Proceedings of the Seventh Allerton Conference on Circuits and System Theory, 459-465, IEEE, New York, 1969.
20. Klose, A., and L. Kurz, "A New Representation and Detection Theory for a Class of Non-Gaussian Channels," IEEE Transactions Communication Technology 1, Nr 2, April 1969.
21. Goldberg, A., "Survey of Impulse Noise Circuits Investigations," Telecommunication and Radio Engineering 2, 1966.

22. Hartley, H. , "Wideband Technique for Improving FSK Reception in Atmospheric Noise," DECO Communications Report 58 CP562-COM Westinghouse Electric Corporation, Leesburg, Virginia.
23. Maisel, L. , "Noise Cancellation Using Ratio Detection," IEEE Transactions on Information Theory 14, Nr 4, 1968.
24. Lee, W. H. , "A Digital System for Large Scale Loran-C Band Sampling," S.B. Thesis, Massachusetts Institute of Technology, 1972 (unpublished).
25. Gupta, S. , "Correlation Between Atmospheric Radio Noise Burst Amplitudes with Different Bandwidths," IEEE Transactions on Electromagnetic Compatibility 13, Nr 1, February 1971.
26. Privis, Y. S. , "Filtering Theory for Multiplicative Noise," Telecommunications and Radio Engineering 24, Nr 10, October 1969.
27. Papoulis, A. , Probability, Random Variables and Stochastic Processes, McGraw-Hill Book Co. , New York, 1965.
28. Dickinson, W. , "Engineering Evaluation of the Loran-C Navigation System," Final Report to U.S. Coast Guard, Contract Tcg-40547, September 1959 (unclassified).
29. Davenport, W. , and W. Root, Random Signals and Noise, McGraw-Hill Book Co. , New York, 1958.
30. Crichlow, W. Q. , et al. , "Amplitude Probability Distributions for Atmospheric Radio Noise," NBS, Boulder Colorado, NBS Mono. 23, 1960.
31. Baghdady, E. J. , (Editor), Lectures on Communication Theory, McGraw-Hill Book Co. , New York, 1961.
32. Rappaport, S. S. , and L. Kurz, "An Optimal Nonlinear Detection for Digital Data Transmission Through Non-Gaussian Channels," IEEE Transactions on Communication Technology 14, Nr 3, June 1966.

33. Richter, R., and L. Smits, "Signal Design and Error Rate of an Impulse Noise Channel," *IEEE Transactions on Communication Technology* 19, Nr 4, August 1971.
34. Deutsch, R., Nonlinear Transformations of Random Processes, Prentice Hall, Englewood Cliffs, N. J., 1962.
35. Cannahan, B., H. Luther, and J. Wilkes, Applied Numerical Methods, J. Wiley and Sons, New York, 1969.
36. Schweppe, F. C., Uncertain Dynamic Systems, unpublished course notes for 6.606, Massachusetts Institute of Technology, 1971.
37. Van Trees, H. L., Detection, Estimation and Modulation Theory, Part I, J. Wiley and Sons, New York, 1968.
38. Van Trees, H. L., Detection, Estimation and Modulation Theory, Part II, J. Wiley and Sons, New York, 1971.
39. Reilly, R. A., "Microminiature Loran-C Receiver/Indicator," *IEEE Trans. Aerospace Electronic Systems* 2, Nr 1, January 1966.
40. Hause, A. D., "Nonlinear Least Squares Filtering and Frequency Modulation," Massachusetts Institute of Technology, Research Laboratory of Electronics Technical Report 371, August 1960.
41. Smith, H. W., Approximate Analysis of Randomly Excited Non-linear Controls, M.I.T. Press, Cambridge, Mass., 1966.
42. Feldman, D. A., "Final Report, Project W-439," U.S. Coast Guard Electronics Engineering Center (unpublished) Wildwood, N. J., 1970.
43. Miller, J. H., J. B. Thomas, "Detectors for Discrete-Time Signals in Non-Gaussian Noise," *IEEE Transactions Information Theory* 18, Nr 2, March 1972.
44. Antonov, O. Ye., "Optimum Detection of Signals in Non-Gaussian Noise," *Radio Engineering and Electron Physics* 12, 541-548, 1967.

45. Lindgren, A. G., et al., "Noise Dynamics of the Phase-Locked Loop with Signal Clipping," IEEE Trans. Aerospace and Electronic Systems 5, Nr 1, January 1969.
46. Develet, J. A., "A Threshold Criterion for Phase-Lock Demodulation," Proc. IEEE 51, February 1963.
47. Frank, R. L., R. W. Nick, "Interference Vulnerability of Phase-Lock Loops with Amplitude Limiting and Sampling," IEEE, AES Convention 1969 Record, Washington, D. C., October 1969, pp. 62-74.
48. Jaffe, R., and E. Rechtin, "Design and Performance of Phase-Lock Circuits Capable of Near Optimum Performance over a Wide Range Input Signal and Noise Levels," IRE Trans. Information Theory 1, March 1955.
49. Evans, J. E., "Probability Density Function Estimation (with Applications to Receiver Design for Reception in Non-Gaussian Noise)" Lincoln Laboratory, Massachusetts Institute of Technology, Technical Note 1969- 47, ESD-TR-69-243.
50. Levin, B. R., and A. Kushnir, "Asymptotically Optimal Algorithms of Detection and Extraction of Signals from Noise," Radio Engineering and Electronic Physics 14, Nr 2, 1969.
51. Griffiths, A. S., "ELF Noise Processing," Lincoln Laboratory, Massachusetts Institute of Technology, Technical Report 490, ESD-TR-72-22, January 1972.
52. Haddad, A., and J. Thomas, "On Minimum Mean Square Error Non-Linear Filtering," TR Nr 16, Inf Sciences and System Laboratory, Princeton University, 1966.
53. Devlet, J. A., "A Threshold Criterion for Phase-Lock Demodulation," Proc. IEEE 51, February 1963.
54. Pervozanskii, A., Random Processes in Non-Linear Control Systems, Academic Press, 1965.
55. Capon, J., "On the Asymptotic Efficiency of Locally Optimum Detectors," IRE Trans. Information Theory 7, April 1961.

Appendix A

INSTRUMENTATION SYSTEM

A.1 Introduction

This appendix provides a general functional description of the instrumentation system used to collect information on atmospheric noise for this research. Detailed circuit schematics of the equipment are not provided, although measured performance characteristics of certain critical circuits are given.

The general functions of the system can be categorized as follows:

- i) Receive and process low-frequency atmospheric noise waveforms in the frequency region 14 kHz to 100 kHz.
- ii) Sample and digitize the processed waveforms according to a prescribed timing sequence.
- iii) Record the resulting digital data in a manner consistent with computer input facilities available.

In meeting the above functional requirements, several performance categories were important. The first of these was to provide a dynamic range in the analog circuits consistent with that of the anticipated atmospheric noise waveforms. This range has often been observed in excess of 100 dB; however, this equipment, due to restrictions in the practically achievable dynamic range of high speed analog-to-digital converters (A/D) is designed for 80 dB in nonlinear processing circuits and 100 dB in preceding linear circuits. A second major consideration in the analog circuits was to insure that the atmospheric noise-waveforms were not obscured by man-made interference, either communication signals transmitted throughout the frequency region of interest or noise generated

within the equipment. The latter may be either random noise in the low-level analog circuits or digital switching noise generated in the timing circuits, and hence synchronous with the sampling patterns.

Within the digital portions of the equipment the principal performance requirement was the generation of a wide variety of sampling/data handling patterns, varying from a maximum rate of 100 kHz to a minimum rate of 0.1 Hz. A second major requirement was the capability to interface this wide variation in data acquisition rate with the data recording device.

A final major performance specification was the inclusion of an operator interface system that provided rapid and flexible adjustment of system parameters and the accurate monitoring and display of various signal levels so that the available system capabilities could be individually optimized for each data sequence. This overall performance is especially important when we recognize that the atmospheric noise is stationary over a period often measured in hours and that a wide variety of sample records had to be collected within that time frame to characterize the noise under those particular conditions.

An overall functional diagram of the equipment is shown in Figure A-1. A sub-functional description with associated performance measurements is given in sections A.2 and A.3 for the analog and digital portions, respectively.

A.2 Analog Signal Processing

Low-frequency atmospheric noise fields were received on a one-meter loop antenna manufactured by Aerospace Research Inc. A single-

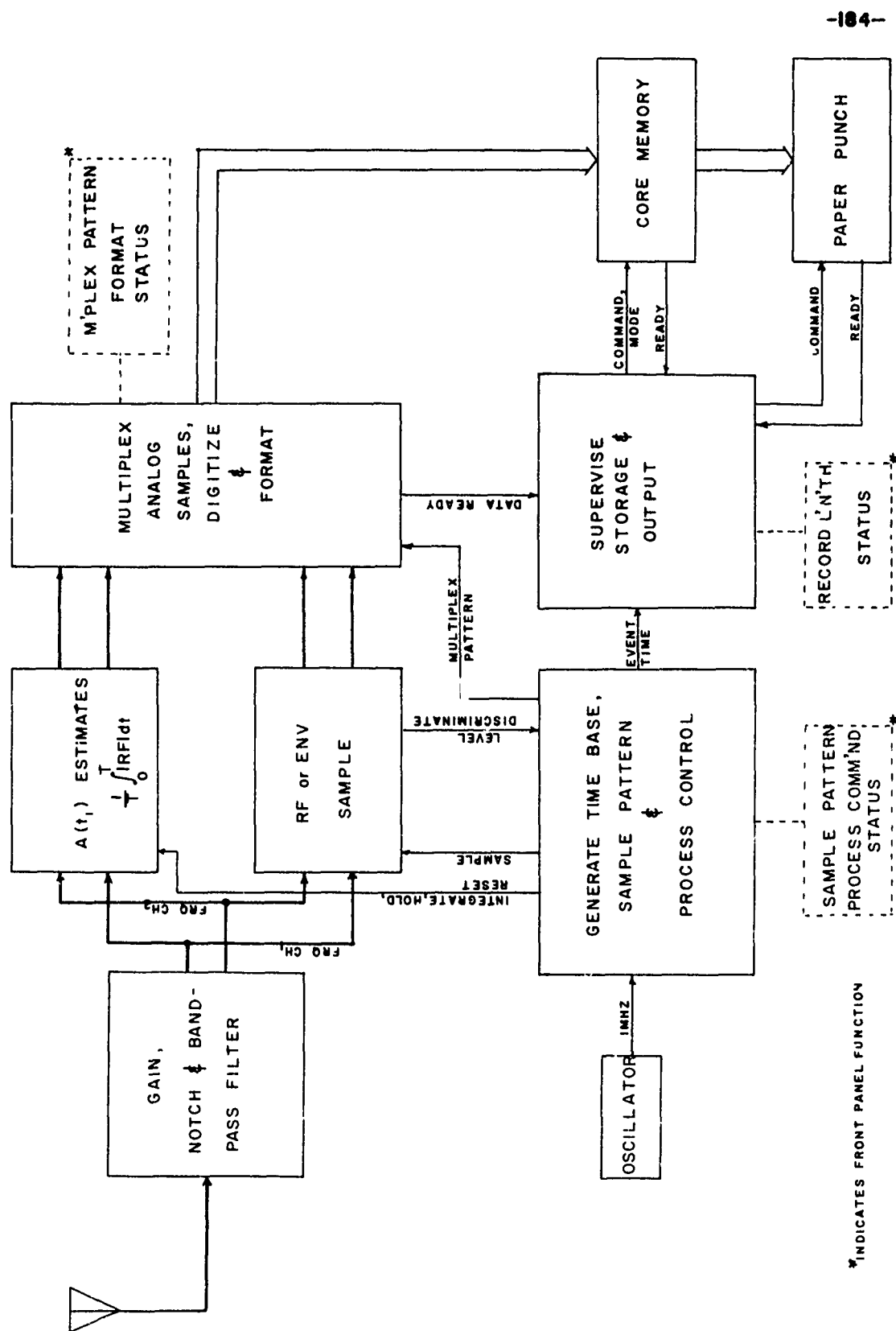


Figure A-1. Block Diagram of Instrumentation System

turn primary, coupled to a seven-turn, secondary transformer, drove a low-input impedance preamplifier via a series resonating capacitor. This circuit provided a single pole response of approximately 60 kHz bandwidth that was tuned to either 100 kHz or 36 kHz. The antenna preamplifier had an equivalent noise voltage, referred to the input, of $8.5 \text{ nV}/\sqrt{\text{Hz}}$. This level was approximately 6-10 dB below the background atmospheric noise component, at 100 kHz, as determined by visual observation of the respective waveforms on an oscilloscope. The preamplifier output was matched to a 100-ohm, balanced, transmission line which also supplied amplifier power.

The signal was then coupled to an array of L-C notch filters to remove large amplitude communication signals present throughout the low-frequency bands. These filters were provided by the U.S. Coast Guard Electronics Engineering Center, Wildwood, N.J., and exhibited maximum notch depths of 60 dB with notch widths at the -3 dB points of 2 kHz. The notch filter output was coupled, via a balanced line, to a differential input FET amplifier followed by a broadband operational amplifier and bootstrapped twin-tee notch filter to remove a strong interfering signal at 18 kHz, which was outside the tuning range of the L-C notch filters. The composite performance of the analog system to this point is shown in Figure A-2.

The received noise signal, with man-made interference reduced to manageable levels, was then coupled to several types of bandpass filters to establish the various noise frequency channels of interest. At the outset of the research, two single-stage bandpass filters of a balanced Butterworth type were used for this function. The center frequency and

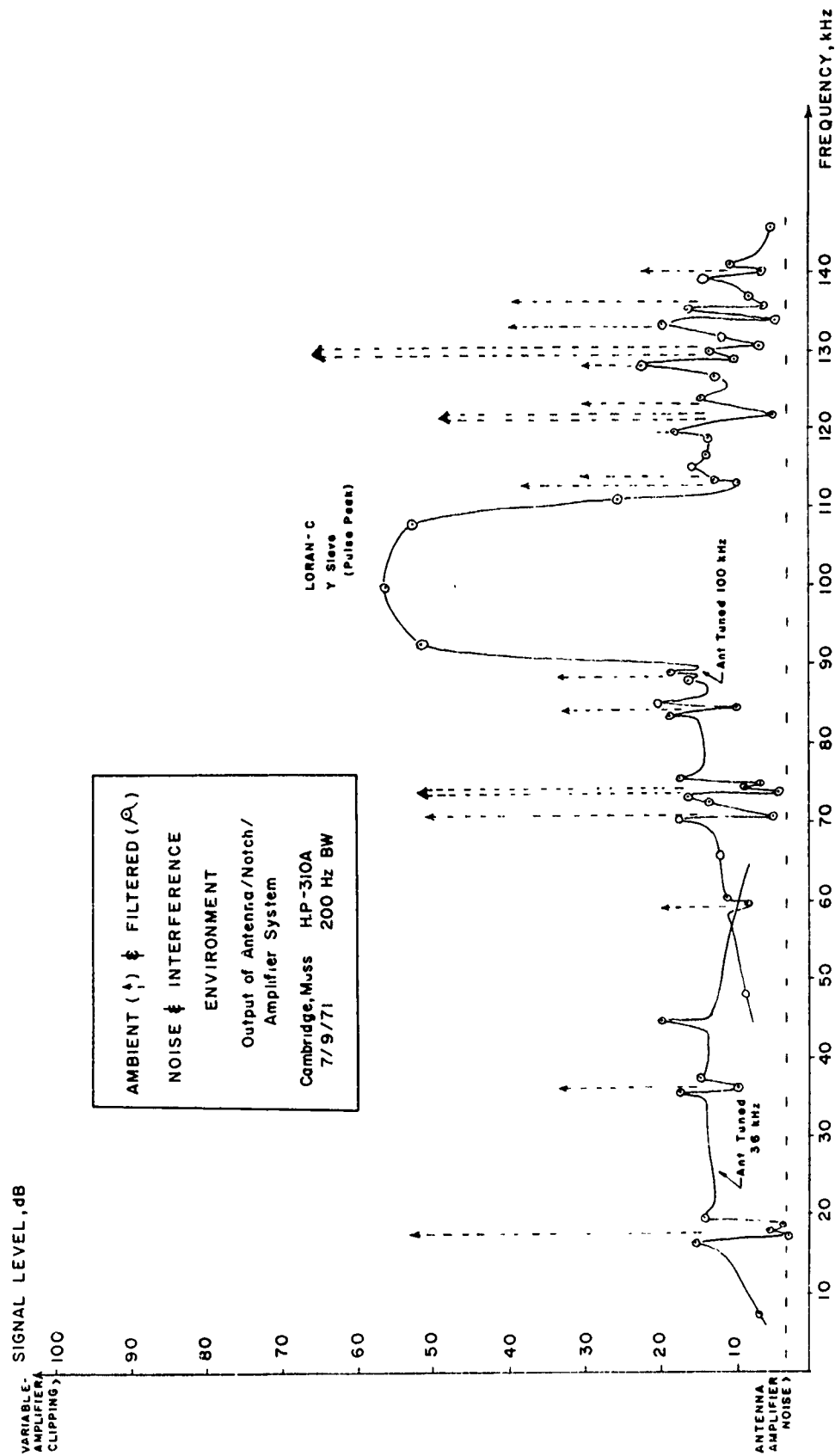


Figure A-2. Received Noise and Interference Spectrum

bandwidth of these filters could be conveniently changed with a plug-in resistor-capacitor network. The inductors used were the same high-Q pot core types used in the notch filters, and they permitted a maximum filter Q of approximately 500. As the research progressed and certain frequency channels were selected as providing representative data, these filters were specialized to fix-tuned, multi-stage types of the Tchebycheff or Lerner characteristic. Figure A-3 shows the frequency response of the various filters.

The bandlimited noise waveforms could be connected to any combination of four processing channels; two wideband amplifier/samplers, or two linear rectifiers followed by lowpass filters or integrate/hold/clear circuits. The latter provided wideband noise envelopes or the $A(t_i)$ sample series discussed in Chapter 2. The wideband samplers were conventional diode ring bridges constructed from matched quads of Schottky barrier diodes. The ring was driven by two dc coupled, pulsed current sources of 600nsec nominal width, included a current balance adjustment and a variable delay adjustment. The sampling gate analog input was driven by a low-impedance, wideband, operational amplifier and had a net slew rate at the holding capacitor of 24 volts/ μ sec. This rate, coupled with the fact that the samples were taken every 10 μ sec and the noise waveform was correlated over at least 50 μ sec, guaranteed tracking of the samples over the full ± 10 volt dynamic range of the analog system. The two diode bridge current adjustments allowed independent balancing of the "on" currents and the turn-off transient caused by both sources not turning off at exactly the same time. This balancing reduced absolute offset errors in the resulting sample to 1 mV.

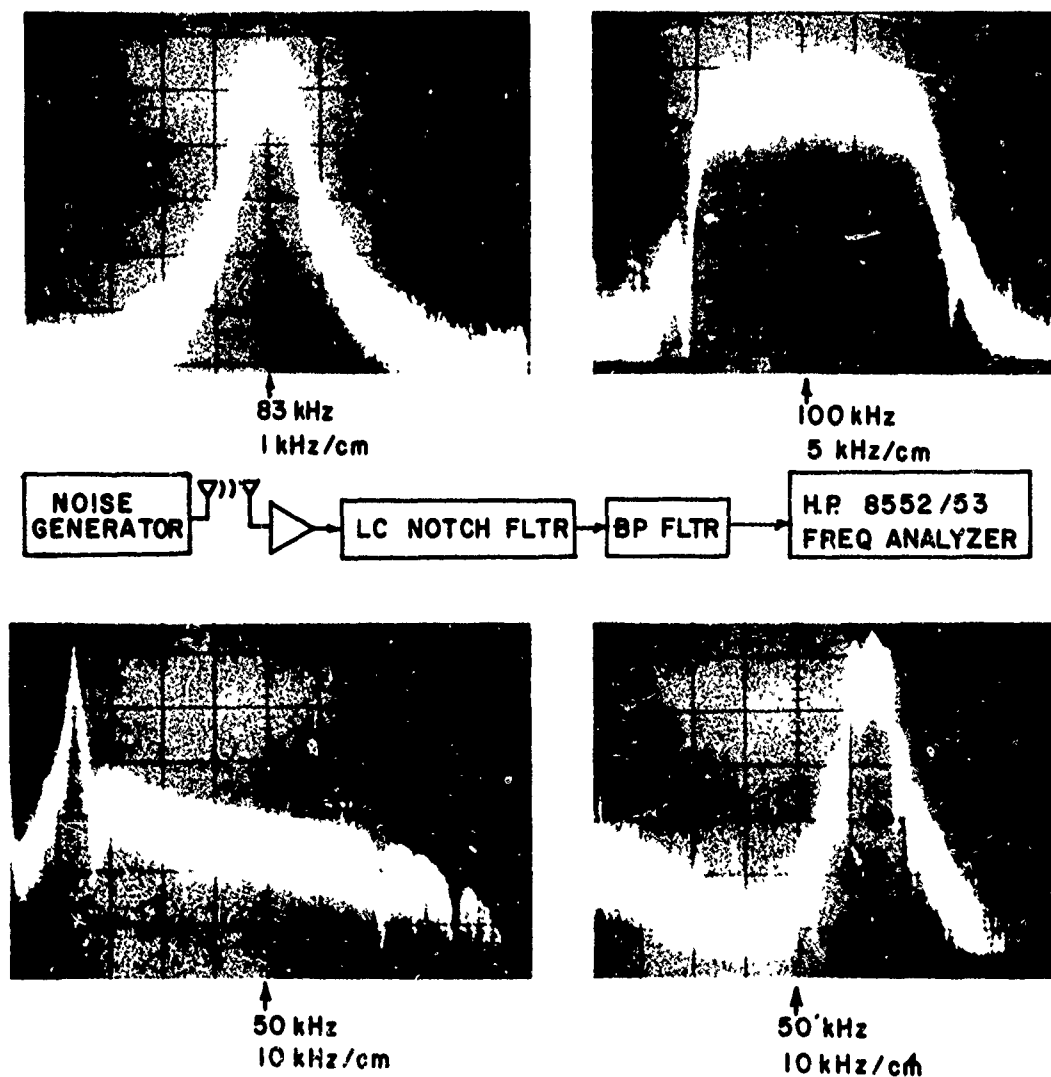


Figure A-3. Frequency Response of Observation Filters

The linear rectifiers utilized germanium diodes in the feedback loop of an operational amplifier to provide a linear range of 76 dB when properly trimmed. The rectifier output was connected to a two-stage, 3 dB ripple, Tchebycheff lowpass filter with 20 kHz corner frequency to recover the envelope from the rf noise waveform. This was fed to the wideband sampler when envelope sample records were required. The rectifier output was also connected to a gated integrator to generate the $A(t_i)$ sample. The input to the integrator was disconnected by an FET switch at the end of the integration period and the output held for 25 μ sec for A/D conversion, followed by a 75- μ sec clear period when the feedback capacitor was discharged by a second FET switch. This "service period" was a fixed 100 μ sec for any specified integration period.

The four possible sampled signal sources could then be connected to the A/D converter via four FET switches and a wideband buffer amplifier with 300-nsec settle time. These switches could be programmed to scan the signal sources in any periodic set of 1, 2, or 4 sources. The switch states were decoded from digital control sequences and the switches were activated at the beginning of a 10- μ sec sample/digitize/store time block so that transients had decayed prior to initiation of A/D conversion. The A/D converter was an Analogic AN-2715M, 15-bit, successive approximation type with total conversion time of 8.5 μ sec in our application. The digital output was in parallel 1's complement and was converted to sign and magnitude prior to storage.

The entire analog system was connected via an FET signal multiplex array to a monitor system. Any signal point (e.g., sampler input, sampler output, rectifier output, etc.) could be selected for monitoring,

resulting in signal availability at a front panel jack for oscilloscope display and processing by a metering circuit for average value of the signal magnitude and peak signal value. These parameters were displayed via a front panel digital voltmeter. The peak value circuit used an FET input threshold detector that provided acquisition of a 10- μ sec, 12-volt pulse to 5% accuracy, with a hold time-constant of 10 minutes. The combination of the average and peak value circuit allowed the operator to monitor these two parameters of the wide dynamic range atmospheric noise waveforms to optimize the use of the A/D converter dynamic range. The meter system was also used for calibration of dc offsets throughout the analog processing system. In addition to this analog monitoring, front panel lights displayed a 2-second pulse whenever any of the analog circuits following the L-C notch filters overloaded. Finally, the A/D digital output was displayed in sign and magnitude format for real time feedback to the operator of the effective signal range and for use in calibration of converter offset and gain.

Figure A-1 shows the various timing signals provided the analog system from the digital system and also an analog-digital path labeled "level discriminate." This was used for conditional sampling patterns as described in Chapter 2 and consisted of two discriminators. The first was a threshold detector connected to the integrator output. This supplied a state change whenever the integrator output exceeded a programmable analog threshold. The second line provided a digital output from a window discriminator which changed state only when the sampled value from one of the wideband samplers fell within a programmable analog voltage window. This latter circuit had a minimum window

resolution of 10 mV.

The analog signal processing system utilized state-of-the-art devices in conventional circuitry that was carefully optimized to provide the required dynamic range, operator feedback and flexibility to conduct an evolving experimental program in which goals and techniques were expected to change as information and insight developed.

A.3 Digital Timing and Control

The digital timing and control system was organized as a synchronous machine on a basic period of 10 μ sec, counted down from the 1-MHz crystal oscillator. The first 3 μ sec of this period were devoted to sampling, signal multiplexing and the start of A/D conversion. The 4-5 μ sec time period was reserved for reading data, stored in core, for output to the paper tape punch. The last 2 μ sec were reserved for formatting data from the converter, temporary storage and writing into core memory. Sampling patterns were generated as multiples of this 10- μ sec period. Sampling could be specified as continuous with spacing, T_s , of 10, 20, 50, 100, 200 μ sec, etc., to 10 seconds, or, in groups of size 2^n . Group spacing was independently specified, as was interior sample spacing. The total sample record could be specified as $256 \cdot 2^n$, $0 \leq n \leq 9$, or indefinite. All timing functions could be linearly scaled by a factor $0.1 \leq a \leq 1$ for synchronous operation at other band center frequencies. This was accomplished by varying the input oscillator frequency from 1 MHz to 100 kHz.

The digital process control was a dc coupled, finite state, machine which could be placed in various test/calibrate modes or initialize/run

mode. In the latter all counters and check circuits were cleared and armed by front panel control and a data run begun by pressing the "GO" button. During the data run, the state of various digital functions was monitored and sampling inhibited in the event of the machine trying to enter a disallowed state such as writing new data over data that had not been read out from memory, or exceeding the programmed number of total samples. The state of the process control was displayed via front panel lights, as was core storage remaining. Synchronous interrupt circuits were also provided to allow the operator to stop sampling or data outputting, during the run, without requiring re-initialization.

A.4 Data Handling

The A/D digital output, in 1's complement, was converted to sign and magnitude and stored in core memory in one of three forms. The first was a direct transfer of the entire 15-bit word into one 16-bit core memory word. This mode generally provided greater sample resolution than necessary, at the expense of data throughput to the recorder, and was only used for applications where such resolution or the sample sign was required, such as measuring the autocorrelation of the bandlimited rf noise waveform. The second mode retained only the most significant 8 bits of the sample magnitude, packed two samples per core word, and was used principally for the $A(t_i)$ sample record which was unipolar and of reduced dynamic range. The third and most often used mode was termed "compressed" and retained either the most significant 7 bits of the sample magnitude or bits 6 through 12 if bits 1 through 5 were all zero (where bit 1, $B_1 \triangleq$ MSB). Bit₈ of the stored

sample indicated whether B_1-B_7 or B_6-B_{12} was present. This mode of operation provided varying resolution but increased dynamic range for maximum data throughput and, as will be seen in Appendix B, was compatible with the probability density estimation algorithm that was used. We emphasize that while the second two modes of operation sacrificed digital resolution in storing and transmitting the sample, the converter always operated at 15 bit resolution. and hence the precision of each 7 or 8 bit sample was that of the original 15 bit conversion. Thus, for example, the resolution of mode two was a relative 2^{-8} but this bit was set to a one or zero with a precision of 2^{-14} in the conversion process.

An automatic data handling test system was built in and exercised prior to each major data recording effort. This system sent a staircase waveform, of 4 steps, to the A/D converter, with binary weighting between steps. This was converted, stored and outputted to the punch in all data handling modes and provided easily verifiable bit patterns on the paper tape. Since the waveform was derived from the precision reference source of the A/D converter, it tested relative converter performance and the entire data format and processing operation through to the punch.

A.5 Data Storage and Output

The core memory, used as a buffer between the variable sampling rates and paper punch, was a commercial grade, 1.5- μ sec access time, memory manufactured by Cambridge Memories. The punch was a Tally Corporation Model P-120 with 120, 8 bit, character/second capacity. The punch was operated on a "handshake" basis with the digital process

control. Punch line power was supplied via an isolation transformer and the data and logic control signals were transferred via an optical isolator. Thus, there was no common ground or conducting connection between the analog-digital instrumentation system and punch, preventing ground loop conduction of the large current transients generated by the punch solenoid drivers.

A detailed description of the digital system is given by Lee.²⁴ As we noted before the entire instrumentation system was characterized by conservative design and adaptability, both features required for study of noise waveforms whose characteristics were not known in advance. Each subsystem was tested during assembly, as were the analysis programs given in Appendix B. Finally, a one-month period was devoted to testing the entire hardware/software system as outlined in Appendix C.

Appendix B

DATA ANALYSIS ALGORITHMS

Appendix A described three modes in which the binary word, representing the data sample, were recorded on paper tape. This tape record was read into the PDP-1X computer and stored on magnetic tape for all further analysis and use. The tape reading subroutine unpacked the 16 bit word and rescaled the "compressed" format sample so that the analysis programs treated each sample as a 14 bit integer plus sign, with only the value of the least significant bit, entered at the time of analysis, indicating the actual format used in recording.

B-1 Probability Density Analysis

The basic frequency-of-occurrence analysis one can perform on a 14 bit integer sample record (neglecting sign) is to count the number of occurrences of each discrete value, or which there are $2^{14}-1$ possible values. In terms of the continuous probability density of the noise waveform, this can be thought of as sorting all samples into "bins" of normalized width 2^{-14} . The probability density estimate based on each bin population is then

$$pd(x_i) = \frac{\text{Number of Samples in Bin } x_i}{(\text{Total Samples}) \cdot (\text{LSB Value})}$$

For our purposes in analyzing atmospheric noise sample records, which have a large dynamic range and low probability of occurrence in the large amplitude region, such a technique leads to a large

variance in the individual bin estimates and is prohibitive in terms of memory requirements for a 14 bit maximum word length. An alternate technique that smooths the probability density estimate and results in a small memory requirement is to represent each sample word as a binary floating point number, $N = a \cdot 2^b$, where "a" is a 4 bit number and $0 \leq b \leq 10$. The occurrence of each sample value will be represented by a point in an 8×12 matrix where the first index specifies the 8 possible values of "a" (there are not 16, except at $b = 0$, since a given value of b specifies that $B_{11-b} = a_1 \equiv 1$) and the second, the value of b . Sorting samples in this manner can be easily programmed with a rotate instruction to find the leading 1 bit (the b index) and then strobing out the next three bits for the a index.

The principal advantage of this floating point analysis algorithm is that it provides a bin width which expands exponentially, in discrete steps, for increasing signal amplitude. Viewed another way, we can say that it provides a non-stationary smoothing function for the probability estimate since it averages across a larger number of the basic bins for increasing signal amplitude. The probability density estimate for this procedure is given by

$$pd(x_i)/\text{volt} = \frac{\text{Nr Samples in Bin } x_i}{(\text{Total Samples}) \cdot (\text{LSB Value}) \cdot (2^b)}$$

where LSB value is the value, in volts, of the least significant bit of the data format used on the record being analyzed. For use in calculating sample moments the signal value at bin center is used (the

average value for sign and magnitude representation)

$$x_i = (a+1/2) \cdot \text{LSB Value} \cdot 2^b.$$

B-2 Probability Density Estimation Error

It is well known⁴⁹ that the probability of a sample occurring in a given "bin" is a binomial trial with probability of occurrence

$$p = \int_{x_0}^{x_0+B_w} p_x(\eta) d\eta, \quad B_w = \text{Bin Width},$$

where $p_x(\cdot)$ is the true, continuous probability density of x . With the estimate of p given by (Number in bin)/(Total Samples = N) the variance of the estimate is (assuming independent samples)

$$\sigma_{\hat{p}}^2 = \frac{pq}{N} \approx \frac{p}{N}, \quad \sigma_{\text{norm}}^2 = \frac{\sigma_{\hat{p}}^2}{p^2} = \frac{1}{pN}.$$

If we describe $p_x(\cdot)$ as

$$p_x(x) = \begin{cases} p_x(0) & , \quad 0 \leq x \leq x_0 \\ \frac{p_x(0)}{x^{m+1}} & , \quad x_0 < x, \end{cases}$$

and consider the two cases of constant bin width and the exponentially increasing bin width (where we approximate the discrete increases as a continuous relation)

$$B_w = B_{w0}, \quad B_w = 2^{\log_2 x} = x$$

the normalized estimate variance is

Constant	Exponential
$\sigma_{\text{norm}}^2 \propto \begin{cases} 1/p_x(0) F_{w_0} N, & x < x_0 \\ x^{m+1}/p_x(0) B_{w_0} N, & x > x_0 \end{cases}$	$\sigma_{\text{norm}}^2 \propto \begin{cases} 1/p_x(0) x N, & x < x_0 \\ x^m/p_x(0) N, & x > x_0 \end{cases}$

This qualitative behavior is summarized in Figure B-1 where we see that the exponential bin width associated with the floating point number representation provides a minimum estimation error in the most critical region of the probability density. Greatest weight was given to fitting the model to the estimated density in this region (Chapter 3).

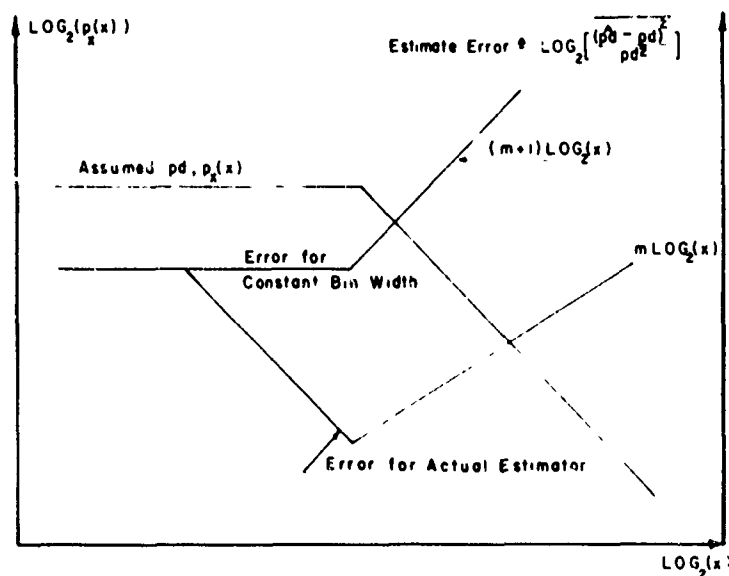


Figure B-1. Probability Density Estimate Error.

B-3 Probability Density Surface Analysis

The probability density surface analysis, used for the joint channel data records, employed a floating point representation for the envelope channel sample with $a = 1$ and for the rf channel sample with $a = 3$. This resulted in a $4 \times 13 \times 13$ matrix to represent all possible occurrences. Density estimation and moments were computed as in B-1 above.

B-4 Correlation Analysis

All sample records that were intended for correlation analysis were taken in continuous bursts where the burst length was much longer than the correlation interval of interest. The basic correlation technique was then to use a conventional lagged products algorithm on each burst and then average each correlation point across all bursts. Samples from different signal sources were interleaved on the record without synchronization codes, a check of correct data transfer was provided by total sample count which was accurately controlled in the instrumentation system.

If we define the following quantities;

$A(i), B(i)$ - Sample Records,

n - correlation point of $\rho_{AB}(n)$, N - Burst Record Length,

K - maximum value of n , M - number of bursts,

then the correlation coefficient was estimated as

$$\rho_{AB}^{(n)} = \frac{\overline{A(i) B(i+n)}}{\sqrt{\overline{A^2(i)} \cdot \overline{B^2(i)}}} = \frac{\frac{1}{M} \sum_{l=j}^M \frac{1}{N-K} \sum_{l=i}^{N-K} A(jN+i) B(jN+i+n)}{\left[\frac{1}{N^2 M^2} \sum_{l=i}^{NM} A^2(i) \sum_{l=i}^{NM} B^2(i) \right]^{1/2}}$$

This provides an unbiased estimate of $\rho_{AB}^{(n)}$, however, little can be said about estimate variance since the statistics are all non-Gaussian. In practice the entire 80000 point sample record was used to obtain the best stability possible.

Appendix C

INSTRUMENTATION TESTS

C-1 Probability Density Tests

The first test that was conducted of the instrumentation hardware and analysis software was a uniform distribution test. An asynchronous square wave was integrated to form a triangular wave, which when sampled, gave rise to a uniform probability distribution. The principal application of this was to calibrate slight inequalities in the widths of the A/D converter quantization. These were apparent at the low amplitude estimates of the probability density and appeared as a noise of much greater variance than predicted with a binomial assumption (see Appendix B). A corrective scale factor that reduced the uniform probability density estimate to the correct value was then inserted in the analysis program and applied to all data analysis.

The second test involved use of a General Radio Random Noise Generator whose output, with flat power spectral density across the 20 kHz to 500 kHz band, was applied to the instrumentation system by transformer coupling to the loop antenna. The resulting bandlimited noise waveform was sampled at 10 times the filter correlation time and the resulting probability density analysis converted to a cumulative distribution. This is shown below, plotted on Gaussian probability paper where a Gaussian cumulative distribution plots as a straight line.

The last probability density test to be applied consisted of an asynchronous sine wave which was modulated between two levels of

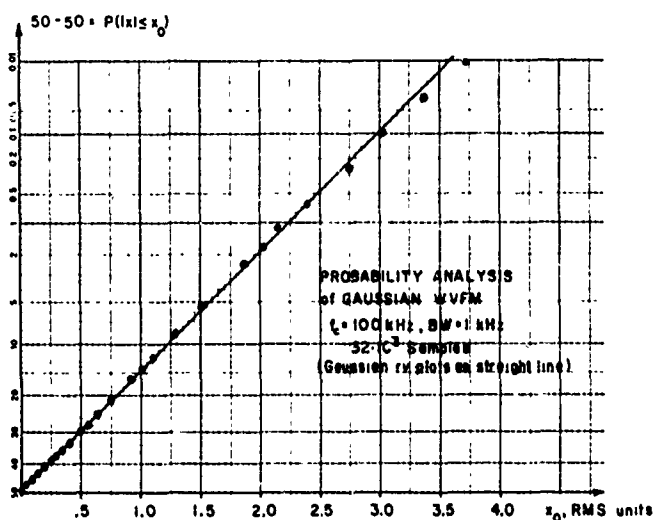


Figure C-1. Estimate of Gaussian Cumulative Distribution

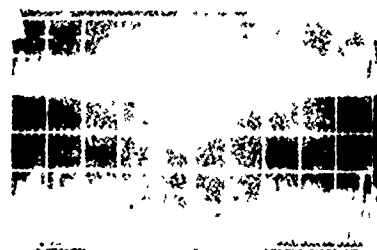
16 V Peak-Peak and 200 mV Peak-Peak. This modulation was at a 100 Hz rate which was asynchronous with both the rf sine wave and the sampling time-base. This type of waveform approximated, in dynamic range, the type of behavior anticipated in atmospheric

noise waveforms. The modulated sine wave was sampled using the "compressed" data mode and the resulting probability density estimate matched quite well the sum of two $1/\sqrt{1 - x^2/x_p^2}$ functions which describe such a switched, randomly sampled, sine wave.

C-2 Correlation Tests

A single effective test of the $A(t_i)$ estimate generators and correlation software was made by using a switched attenuator, as described above, to modulate the power level of a white Gaussian noise process. The white noise was then bandlimited at two different center frequencies and the $A(t_i)$ estimates of the short-time power level were formed using 1 msec integration times. The two resulting integrator waveforms are

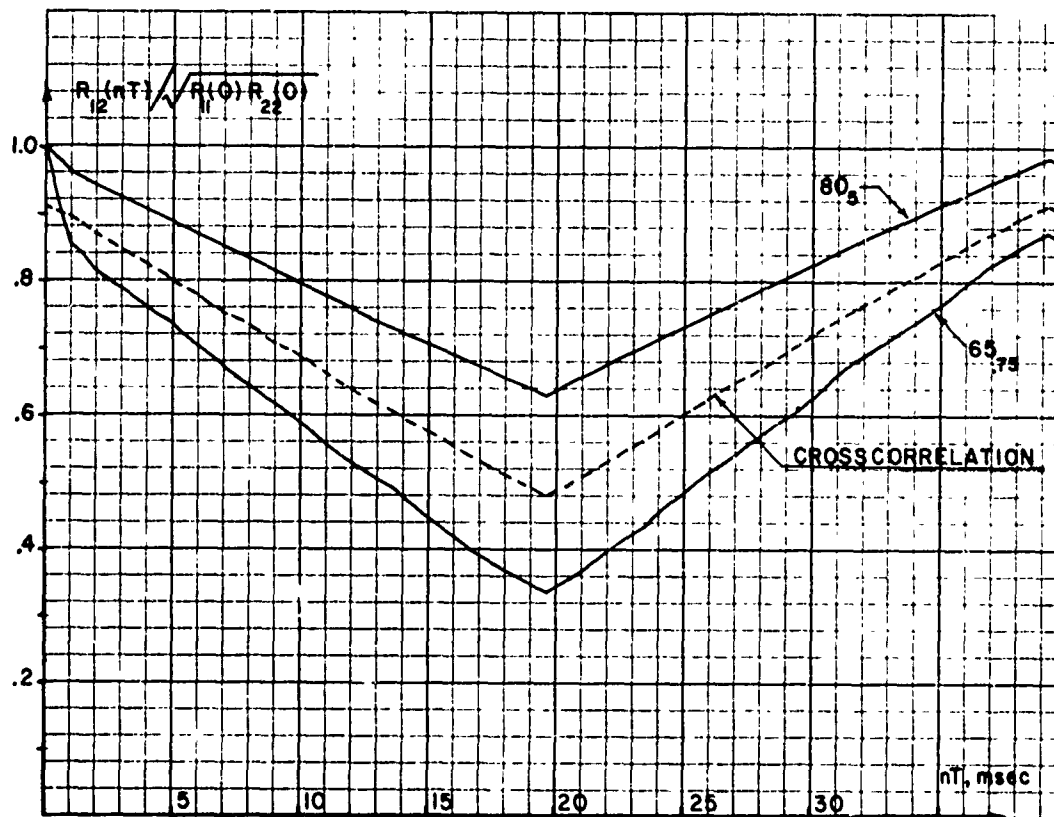
shown in Figure C-2. We note the obviously greater variation in the estimates, represented by the peak of the ramp, in the narrowband waveform compared to the broader bandwidth. The auto and cross-correlation analysis for a 10,000 point sample record is shown in the same figure. The waveform variance is indicated by the shaded areas at the origin, where we see that the .75 kHz bandwidth, slightly less than used in the final data recordings, yields a normalized variance of the power level estimate of 0.1. In comparison, the analysis of the 1 msec integration time data indicated variances of 0.7-0.85 and we would conclude that this is a reasonably accurate measure of atmospheric noise characteristics rather than an effect caused by the background Gaussian noise. Other tests verified the correlation software for bipolar data and the various data recording modes.



65 kHz, 0.75 kHz BW

80 kHz, 5 kHz BW

1 msec INTEGRATOR WAVEFORMS with
WHITE NOISE EXCITATION of TWO CHANNELS
5 v/cm, 5 msec/cm
(A(t_i) Samples taken at peak)



CORRELATION ANALYSIS, 10 GROUPS of 512 POINTS per GROUP

Figure C-2. Correlation Test Result

Reproduced from
best available copy.

Biography of Donald A. Feldman

Donald Feldman was born 19 October 1939 at Seattle, Washington. He graduated from the United States Coast Guard Academy in 1961, receiving the B. S. degree and a commission as Ensign in the Coast Guard. He served aboard ship for three years, entering the M. I. T. graduate school in 1964. He received the S. M. and Engineer degrees in 1966 and served the next four years at the U. S. Coast Guard Electronics Engineering Center, Wildwood, N. J. He received the Coast Guard Commendation Medal for engineering work performed at the Center. He returned to M. I. T. in 1970 to complete the doctoral program and the research reported here. He was reassigned to the Electronics Center as Chief of the Engineering Division in 1972.